Summer 7-17-2014

Mechanical Failure of Chorioamnion and Cervical Tissue: Contributions to Preterm and Term Birth

Brandi Nicole Briggs
University of Colorado Boulder, brandi.nicole.briggs@gmail.com

Recommended Citation

Briggs, Brandi Nicole, "Mechanical Failure of Chorioamnion and Cervical Tissue: Contributions to Preterm and Term Birth" (2014). *Mechanical Engineering Graduate Theses & Dissertations*. 5.
https://scholar.colorado.edu/mcen_gradetds/5

MECHANICAL FAILURE OF CHORIOAMNION AND CERVICAL TISSUE: CONTRIBUTIONS TO PRETERM AND TERM BIRTH

by

BRANDI NICOLE BRIGGS

B.S., University of Maryland Baltimore County, 2008

M.S., University of Colorado Boulder, 2011

A thesis submitted to the
Faculty of the Graduate School of the
University of Colorado in partial fulfillment
of the requirement for the degree of
Doctor of Philosophy
Department of Mechanical Engineering
2014

This thesis entitled:
Mechanical Failure of Chorioamnion and Cervical Tissue: Contributions to Preterm and Term Birth
written by Brandi Nicole Briggs
has been approved for the Department of Mechanical Engineering

____
Virginia L. Ferguson

____
Mark E. Rentschler

Date_______________

The final copy of this thesis has been examined by the signatories, and we find that both the content and the form meet acceptable presentation standards of scholarly work in the above mentioned discipline.

IRB protocol # COMIRB 11-0570, COMIRB 06-1159, CU Boulder IRB1007.16

Briggs, Brandi Nicole (Ph.D., Mechanical Engineering)

Mechanical Failure of Chorioamnion and Cervical Tissue: Contributions to Preterm and Term Birth

Thesis directed by Virginia L. Ferguson, Ph.D.

Despite significant advances in medical research, spontaneous preterm birth (SPTB) rates have not changed appreciably in over 100 years. SPTB is a global problem affecting 13 million babies annually and continues to be the leading cause of death among infants. During pregnancy, the cervix and chorioamnion (CA), the sac that surrounds the fetus during pregnancy, provide critical structural support for the growing fetus that requires optimum maintenance of tissue properties for sustaining pregnancy. This dissertation aims to elucidate the events leading to tissue failure in pregnancy by evaluating detrimental alterations in the extracellular matrix (ECM) chemistry and organization and tissue material properties that result in gross structural or functional tissue changes. To study tissue material property losses in the cervix, a novel technique was developed using ultrasound elastography (UE) by coupling ultrasound with a strain dimension to measure applied *in vivo* strains. A standardized method for UE image collection, using reference standards, image analysis, and an analytical solution that incorporated Hertzian contact mechanics, was developed and validated on tissue phantoms to measure *in vivo* tissue stiffness. With further validation on the human cervix and other heterogeneous materials, this technique shows promise for monitoring cervical stiffness *in vivo* to detect premature softening. To elucidate mechanisms that cause preterm rupture of CA, this dissertation characterized material properties and ECM composition and organization of both the amnion and chorion in term membranes with different modes of rupture. Clinically strong membranes (*i.e.* artificially ruptured CA) demonstrated an increased modulus in the rupture region of chorion and intact CA, but not in the stiff amnion. These results suggest that failure of the chorion to support and integrate with the amnion may play a large role in causing preterm rupture. Overall, the studies included in this dissertation provide novel approaches to measuring material properties and detecting ECM alterations in tissues that are critical for providing structural support during gestation. Thus, the work described in this thesis motivates future studies that could evaluate how the collective influences of cervical and CA gross structure and function link with ECM biochemistry, structure, and organization to ultimately lead to SPTB.

DEDICATION

For my husband, Kenny, my son, Luke, and my parents, who have provided continued support throughout the years.

ACKNOWLEDGEMENTS

First I would like to thank my research advisor, Ginger Ferguson, for the endless advice and support over the past six years. Thank you for the countless hours you have spent meeting with me, responding to e-mails, editing documents, and writing grants. You have shown me that unexpected results are exciting results and helped me to become the research scientist that I am today. I would also like to thank my committee members Dr. Karen Jonscher, Dr. Mark Rentschler, Dr. Wei Tan, and Dr. Virginia Winn for the many hours you spent reviewing my work and providing invaluable feedback. Additionally, I am immensely grateful for the many funding sources that made this dissertation and my time at the University of Colorado possible – the Butcher Foundation at the University of Colorado Boulder, the CU Boulder Innovative Grant Program, the Colorado Clinical and Translational Sciences Institute, the Dean's Graduate Student Research Grant, the Achievement Rewards for College Scientists Foundation, and the Department of Mechanical Engineering Summer Fellowship.

I have had the privilege of working with so many wonderful scientists who helped me to complete the work in this dissertation through their assistance in the lab or by engaging in many hours of conversation to understand my data. In particular I would like to acknowledge the past and present members of the Ferguson lab. Thank you for all the great feedback you all have provided during our many conversations in group meetings and in the office. Thank you to the many undergraduate students that I have had the pleasure of mentoring and who have contributed to this dissertation – Kristopher

Schneider, Veronica Hogg-Cornejo, Carly Barnard, Luke Ladtkow, and Patrick Muljadi. I am immensely grateful for Dr. Virginia Winn and her lab, Anita Kramer, Dr. Meghan Donnelly, and Dr. Michael Plotnick, who spent many hours collecting placental membrane samples for me. A special thank you to GE Healthcare for the use of a Voluson E8 ultrasound system and to Barbara Kari for going above and beyond to help us succeed with this project. Additionally, I wish to thank Christian Perrey at GE Healthcare for taking the time to answer our ultrasound elastography questions. I would like to recognize the University of Colorado Hospital for allowing us to use their facilities to store the ultrasound system and to spend many hours using their rooms while collecting ultrasound images. Thank you to Dr. Meghan Donnelly who spent countless hours brainstorming with us, trying all of the crazy ideas we thought of, and collecting ultrasound elastography images for this dissertation. I also want to recognize the Anseth lab for the great histological training and consultation, and for the use of their histology equipment.

Lastly, I want to thank my amazing family and friends who have always been there supporting me and providing encouraging words. You all have helped me to push through the hard times and to celebrate the good times. Without you I would not be the person I am today. Finally, I wish to thank my wonderful husband who stuck through it all with me. Thank you for all the nights you cooked dinner while I studied and then made a pot of coffee on your way to bed, for the countless late nights you came to help me clean up in the lab, for always being there to listen, and most importantly for your continued support, encouragement, patience, and love you have always shown me. I would not have been able to do it without you.

CONTENTS

CHAPTER

TABLES

Table

FIGURES

Figure

CHAPTER 1

MOTIVATION AND SPECIFIC AIMS

Despite significant advances in medical research, spontaneous preterm birth (SPTB) rates have not changed appreciably in more than 100 years. SPTB is a global problem affecting 13 million babies annually and remains to be the leading cause of death among infants[53]. Babies born preterm are at increased risk for a plethora of conditions affecting their quality of life including respiratory problems, vision problems, hearing impairment, feeding and digestive problems, cerebral palsy, and developmental delay[2]. One emerging theory as to why the preterm birth rates continue to be unacceptably high is due to the focused approach the research community has taken to characterize the pathways that lead to SPTB; when in reality, it is an immensely complex problem. Therefore, there exists a need for a holistic research approach for studying SPTB that recognizes nano-scale molecular parameters and micrometer length scale contributors to macro tissue function across the integrated system of tissues critical for sustaining pregnancy.

During pregnancy, the cervix provides a foundation and mechanical support for the overlaying chorioamnion (CA) (Figure 1.1). When the internal *os* of the cervix softens and begins to funnel, the foundation for the CA diminishes, changing the loading conditions on the CA, and causing further distension of the membrane (Figure 1.2). This increase in distension can ultimately lead to CA tissue failure. **Therefore, we hypothesize that the cervix, the CA, and their substructures form a hierarchical and integrated load bearing system that undergoes mechanical failure to initiate birth. In particular, we hypothesize that alteration of ECM constituents, structure, and organization influences tissue material property losses, which in turn enables gross structural and functional tissue changes and, ultimately, tissue failure** (Figure 1.3). The timing of this cascade is imperative to the outcome of the pregnancy, whether tissue failure leads to preterm (< 37 weeks gestation) or term birth.

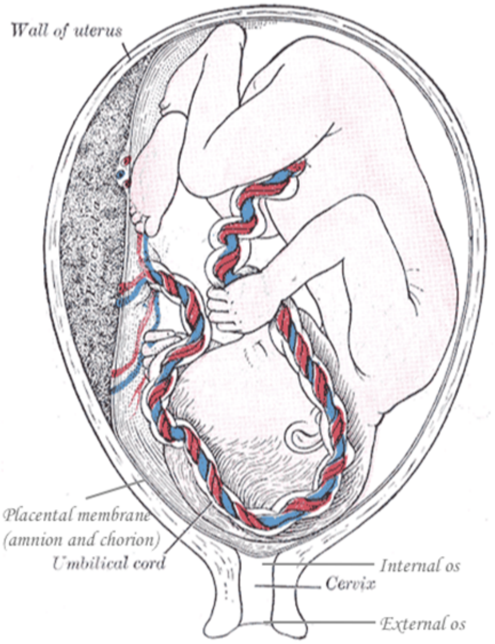

Figure 1.1. The cervix is located at the lower uterine pole with the internal *os* closest to the uterus. The placental membrane, chorioamnion, is the sac the surrounds the fetus *in utero*. It extends from the placenta and contains the amnion (innermost layer) and the chorion (outer layer). [63]

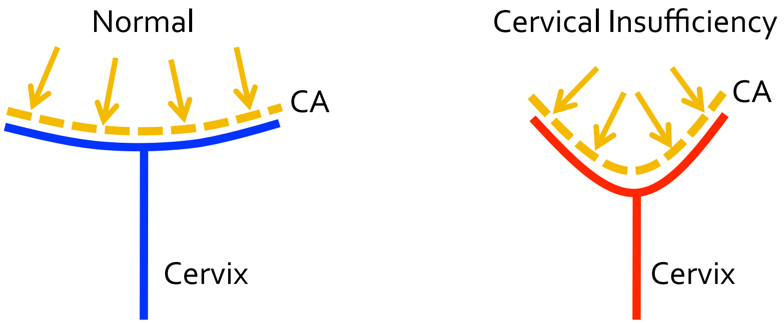

Figure 1.2. The cervix provides a foundation and mechanical support for the overlaying CA. When the internal *os* of the cervix softens and begins to funnel, either due to cervical insufficiency or ripening at term, the foundation for the CA diminishes, changing the loading conditions on the CA, and causing further distension of the membrane.

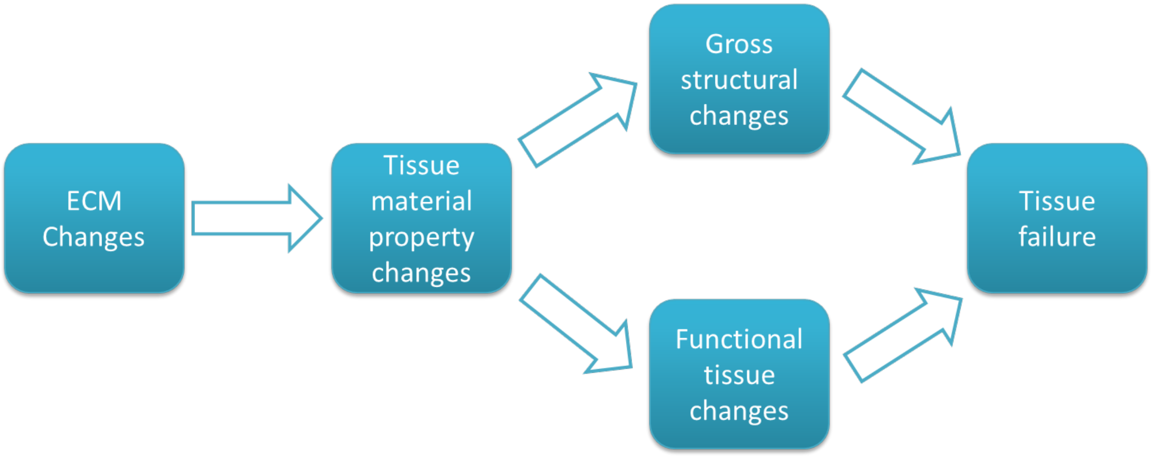

Figure 1.3. Alteration of ECM constituents, structure, and organization influences tissue material property losses, which in turn enables gross structural and functional tissue changes that causes tissue failure (*i.e.* preterm or term birth).

Premature softening and dilation of the cervix is diagnosed as cervical insufficiency. This event is sometimes suspected mid-pregnancy when funneling at the internal *os* (Figure 1.2) or shortening of the cervix is observed during a routine ultrasound examination. However, cervical ripening is asymptomatic and so it is often missed until after a patient experiences preterm labor or a second or third trimester miscarriage. The ability to diagnose cervical softening earlier in pregnancy, prior to the resulting gross structural changes (*i.e.,* cervical funneling), could improve upon the clinical detection of cervical insufficiency and indicate the need for hydroxyprogesterone caproate injections (the synthetic version of progesterone that has been shown to prolong pregnancy) or potentially increase the success rate of a cervical cerclage (the placement of a suture into and around the cervix to prevent further dilation).

Ultrasound elastography (UE), where traditional B-mode ultrasound is coupled with a tissue strain dimension to measure strains resulting from an applied cyclic load[128], provides potential for a non-invasive method to easily and safely monitor cervical softening throughout gestation. However, UE provides only a qualitative measure of relative strain displacement within the field of view. To calculate a modulus from the strain measurement, the stress in the tissue must be ascertained by use of a force transducer[77] or reference standard[38,64,176]. Additionally, the transvaginal transducer probe tip geometry is spherical, causing strain dissipation within the imaged tissue during compression[64,66,115,127]. Therefore, to obtain a semi-quantitative measure of cervical stiffness throughout gestation, a standardized method of image acquisition, stress measurement, and strain dissipation correction must be established.

The second component to the integrated cervix-CA system studied in this dissertation is the CA. The CA is the sac that surrounds the fetus *in utero* and is designed to mechanically rupture at term to allow delivery of the fetus. Preterm premature rupture of the membrane (PPROM), rupture prior to 37 weeks gestation, increases the risk of infant morbidity and mortality. The necessary biochemical and mechanical changes that occur to weaken the membrane and prepare it for rupture either at term or preterm are not thoroughly understood.

Past studies have focused on characterizing possible individual contributors to membrane rupture such as material properties, structure, and protein expression of the individual CA layers. These studies have shown that the amnion is physically stronger and stiffer than the chorion and concluded that the amnion is the primary structural determinant for the CA membrane[134,135].

These results have driven us and others to primarily consider the amnion properties during gestation [29,131,136]. When studying membrane properties adjacent to the site of rupture as compared to near the placenta, differences were observed in material properties and protein expression suggesting an altered ECM near the site of rupture[48,49]. To gain a holistic understanding of the events contributing to the timing of membrane rupture *in vivo* the combination of these factors on term membranes with differing modes of rupture requires deeper study. Additionally, few studies have considered the CA membrane as a composite system that includes the combination of the amnion, chorion, and their interface to understand the interplay of each layer in the timing of membrane rupture. A complete study that investigates multiple contributors to functional tissue changes in both the chorion and amnion may elucidate possible mechanisms leading to PPROM.

As a whole, this dissertation aims to elucidate the events leading up to tissue failure in pregnancy by evaluating ECM and tissue material property changes that cause gross structural or functional tissue changes. Thus, the specific aims for this study are:

1.1 SPECIFIC AIMS

(1) Aim 1: To establish materials and methods that enable quantitative evaluation of cervical stiffness, or modulus, using UE.

Hypothesis: Tissue phantom stiffness can be quantified using UE when incorporating a reference standard of known stiffness into the image.

Approach: Characterize reference standards using mechanical testing and validate their use with UE by imaging gelatin tissue phantoms of known stiffness.

(2) Aim 2: To develop an analytical solution that corrects UE data for strain dissipations within the imaged tissue caused by compression of a spherical tip (*e.g.* transvaginal transducer probe) into the tissue.

Hypothesis: Calculated UE moduli error due to strain dissipation caused from compressing tissue with a spherical tip (*e.g.* transvaginal transducer probe) can be reduced by assuming a Hertzian contact analysis.

Approach: Develop an analytical solution to characterize the strain dissipation observed when imaging tissue phantoms with a transvaginal transducer probe using Hertzian contact mechanics formulations and three-dimensional Hooke's law equations.

(3) Aim 3: To elucidate the role of microscopic length scale contributors to macro tissue function in CA membrane failure.

Hypothesis: The ECM composition, structure, and organization dictates tissue material properties of the amnion and chorion. Furthermore, the interaction of the amnion, chorion, and the strength of the interface between these two layers influences the timing of CA membrane rupture.

Approach: Use mechanical testing to compare tissue properties adjacent to the site of rupture and near the placenta for membranes that ruptured spontaneously versus artificially at term. Three perspectives will be considered: (1) amnion only, (2) CA composite, and (3) the interface between the amnion and chorion. Measure ECM composition and visualize structural organization in the amnion and chorion to elucidate causes for observed clinical differences between membrane modes of rupture.

CHAPTER 2

INTRODUCTION

2.1 ANATOMY OF THE HUMAN CERVIX

The human cervix is located distal to the uterus (Figure 2.1). The external orifice opens to the vaginal canal and the internal orifice connects to the uterine wall. It can be approximated as a cylindrical structure with the cervical canal at the center (Figure 2.2). This dynamic tissue changes dimensions and geometry throughout pregnancy with thinning of the cervical stroma and opening of the cervical canal at term to allow for delivery of the fetus.

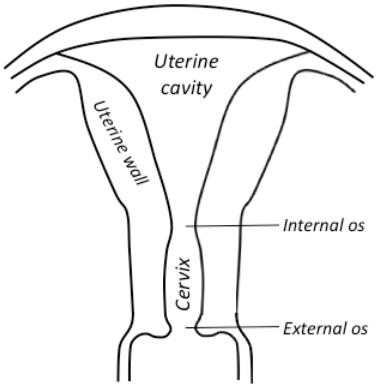

Figure 2.1. The cervix is located distal to the uterus with the external orifice opening to the vaginal canal. (Frontal view of female anatomy)

The cervix can be divided into two layers of tissue, the cervical mucosa and stroma. The mucosa lines the stroma and is exposed to the cervical canal (Figure 2.2). It consists of a single layer of columnar epithelium. Extending from the mucosa layer are numerous cervical glands that cause thick secretions from the cervical canal. The stroma constitutes the bulk of the cervix. It is composed primarily of collagen, proteoglycans, and glycosaminoglycans; however, small quantities of elastin and smooth muscle have also been identified in this region of the cervix. It is the organization and composition of the stromal extracellular matrix (ECM) that dictates the mechanical properties of the bulk cervical tissue. [146,163]

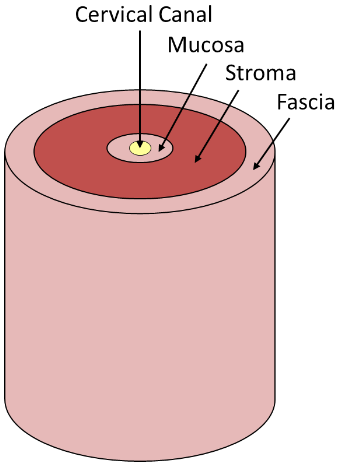

Figure 2.2. Simplified schematic showing the mucosa, stroma, and fascia layers of the cervix surrounding the cervical canal.

Collagen content is typically associated with soft tissue strength in tension; however, the organization and orientation of the collagen fibers can significantly alter the mechanics of the tissue as well. The cervical stroma has been studied using MRI and X-ray to quantify the orientation of the collagen fibers.[13,168] Three zones of collagen fibers were identified. The innermost and outermost rings of the stroma contain collagen fibers that are preferentially aligned in the longitudinal direction, whereas the middle layer consists of collagen fibers preferentially aligned in the circumferential direction (Figure 2.3). The preferential orientation of collagen alignment in the cervix likely indicates increased strength in these

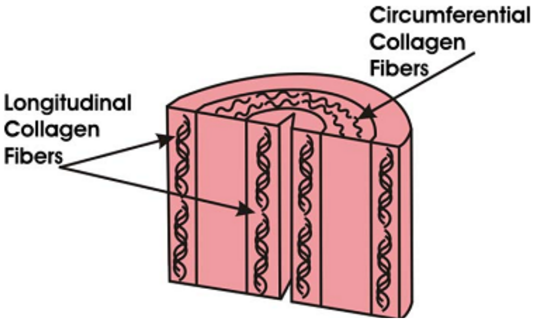

Figure 2.3. Schematic indicating the preferential orientation of collagen fibers in the cervical stroma.[13]

directions.

Not only does the organization of collagen contribute to soft tissue mechanical properties but the type, concentration, and degree of cross-linking also plays a large role in tissue strength. Cervical stroma consists of primarily collagen types I and III.[82]In the non-pregnant cervix 54-77% of cervical dry weight is attributed to collagen.[69] The degree of collagen cross-linking can be measured by quantifying the solubility of the collagen fibers. Increased solubility is associated with newly synthesized collagen and fewer cross-links. Decreased solubility indicates mature collagen and increased cross-links. In the non-pregnant cervix, 18-67% of the total collagen content is soluble. [62,73,118,121,122,141,146,163,169] This large range indicates the widespread variability often seen in human subjects.

Proteoglycans (PGs) are composed of negatively charged glycosaminoglycans (GAGs) and a protein core that consequently attracts water, resulting in tissue swelling and a water content of 75-80% in the non-pregnant cervix.[118,146,163] Hydrated tissues exhibit distinct viscoelastic and poroelastic physical properties when water can move through the tissue. In tension, hydrated tissues can exhibit a loss in energy upon loading (hysteresis) and a curvilinear loading curve such that the modulus of the material increases with increasing strain as water content is lost in the tissue. The high water content in the cervix combined with a well-organized collagen matrix results in limited water movement through the cervix and the ability to sustain high levels of compressive loading during gestation. [119] A secondary function of PGs in the cervix is to regulate collagen fibril formation and organization, which has also been discussed to alter tissue mechanical properties. The primary PG in the cervix is decorin[164], which constitutes 90% of the cervical PG content. Decorin has been shown to be associated with increased collagen organization and cross-linking in soft tissues. There are three types of sulfated GAGs in the cervix: chondroitin and/or dermatin sulfate, heparin and heparin sulfate, and keratin sulfate. Also present in the cervix is hyaluronan, a free GAG chain that is not attached to a PG protein core.[69]

Small quantities of elastin and smooth muscle have also been identified in the cervix. Elastin accounts for the elastic behavior of the cervix, which is hypothesized to allow the cervix to return to its original shape following distension. In non-pregnant tissue, elastin makes up 0.9-2.9% of the cervical dry weight.[90] Smooth muscle accounts for less than 10% of the cervix[42] and does not appear to contribute to the overall strength of the tissue.[140]

2.2 MECHANICAL PROPERTIES OF THE CERVIX

Tissue mechanical properties are highly dependent upon the organization and composition of the ECM, thus the mechanical response of the cervix agrees well with known properties of a collagen matrix combined with a generous concentration of PGs and GAGs. Both collagen and PGs/GAGs are known to cause a nonlinear, time-dependent stress response, so it's not surprising that the cervix also exhibits a non-linear, time-dependent response in both tension and compression.[47,119,140] Collagen fibrils are also known to have differing properties in tension compared to compression. In tension, a collagen fibril is remarkably stiff; however, in compression the same fibril will buckle under a small load. The cervix is known to have collagen fibrils with a preferential orientation along the longitudinal axis.[13] Therefore, these preferentially aligned collagen fibrils are likely responsible for the increased stiffness in tension compared to compression along the longitudinal axis. In compression, the organization of the collagen matrix in combination with the PGs and GAGs are known to drive the mechanical response through hydraulic permeability.[120] Non-pregnant tissue has a well-organized collagen matrix that limits water movement through the tissue, thus decreasing hydraulic permeability and increasing the strength of the tissue in compression.[119] Therefore, it can be deduced that the bulk mechanical response of the cervix is a complex interplay between the tensile properties of the collagen network and the compressive response of the hydrated GAGs.[120]

The mechanical response of the cervix also depends upon the direction of loading (anisotropic) and location on the cervix (heterogeneous).[120] Consistent with any soft tissue that contains collagen with a preferential orientation, the cervix has been shown to be anisotropic. As expected, in tension the cervix is more compliant when the collagen fibers are aligned orthogonal to the applied force. On the other hand, in compression the cervical tissue demonstrates a stiffer axial stress response when the collagen fibers are aligned orthogonal to the applied force. This indicates the effectiveness of the collagen fibers to constrain lateral stretches in compression. Given these results, the stress response of the cervix is dependent upon the distance from the cervical canal since the collagen fiber orientation changes with distance from the cervical canal (Figure 2.3). Additionally, the material properties of the cervix also vary with location along the longitudinal axis, with the external *os* being the stiffest and the internal *os* being the most compliant.[40,119,120]

It should be noted that most mechanical testing on the human cervix has been performed *ex vivo*, impairing the ability to simulate realistic boundary conditions and loading profiles. Human samples are typically obtained through hysterectomy, including caesarean hysterectomy at the end of pregnancy. Normalcy of the tissues obtained with this method is questionable since the reason for a hysterectomy is usually related to a specific pathology that may have an unknown effect on the cervix. To allow for a more controlled investigation, several studies also tested the constituents and mechanics of mouse cervix. These studies are limited by the difference in anatomy and thus loading conditions on the mouse cervix compared to the human cervix.

2.3 CERVICAL RIPENING

The human cervix serves a dual structural function throughout pregnancy. Prior to term, the main purpose of the cervix is to support the weight of the fetus during development. The cervix fulfills this function by staying closed and firm. At term, it must soften and dilate to allow delivery of the fetus (i.e. cervical ripening). Several factors contribute to this ripening process and thus dictate the integrity of the cervix at different time points during gestation. The studies discussed in this work will focus on three factors that can indicate the status of cervical function during pregnancy: cervical geometry, ECM constituents, and material (tissue) properties.

Gross structural changes during cervical ripening

The shape of the cervix can reflect the presence of remodeling within the tissue. If no softening or remodeling has occurred the cervical shape should be similar to that of the non-pregnant cervix, long and closed. Since the internal *os* is typically the most compliant area of the cervix, this is also the area that tends to experience thinning of the cervical stroma (effacement) and thus opening of the cervical canal (dilation) first. The opening of the internal *os* is termed funneling and results in a cervical canal that has the shape of a Y.[70] The length of the cervix is defined as the region of the cervical canal that has remained closed. Therefore, funneling of the internal *os* also results in decreased cervical length. With progressive cervical remodeling and softening, increased thinning of the stroma, opening of the canal, and decreased cervical length are observed. This progression results in the canal having the shape of a V and then a U. [70] Therefore, the geometry, in particular the cervical length, can be used to assess the degree of cervical remodeling that has occurred and the resulting risk of delivery.

Biochemical contributors to cervical ripening

Complex biochemical processes resulting in changes of the ECM content and organization are thought to play a large role in the drastic mechanical property changes necessary for cervical ripening (Table 2.1). [58,69,89,171] Of particular interest during pregnancy are the changes in collagen content, organization, and solubility as well as PG and GAG content. It has been thought that the expression of matrix metalloproteinases (MMPs) are largely responsible for these changes in the ECM. In particular, MMP-1, MMP-2, and MMP-9 have been shown to increase during pregnancy both before and during labor. MMP-1, in particular, breaks down collagen types I and III, both of which are known to be the primary collagens in the cervical stroma.

Collagen content, organization, and cross-linking is known to directly correlate to soft tissue strength *in vivo*. In the cervix, the total collagen content has been shown to decrease towards the end of gestation in preparation for dilation. 54-77% of the non-pregnant cervical dry weight consists of collagen while only 23-36% of the cervical dry weight is collagen in the third trimester. [62,73,163,169] Collagen content further decreases during labor[163], when the cervix is required to reach maximum dilation and effacement. In addition to collagen content, the organization and cross-linking of collagen can alter the mechanical properties of the tissue. Collagen organization and cross-linking in the cervix has been measured by quantifying collagen solubility. Collagen solubility begins to increase in the cervix as early as 10 weeks gestation[163] and by the third trimester 80-90% of the collagen in the cervix is soluble. [62,73,82,119,121,122,141,163,167,169] This increase in collagen solubility has been correlated to cervical softening and shorter labor times. Additionally, morphologic studies have observed a decrease in collagen anisotropy further supporting the decrease in collagen organization observation with increased gestation.[118,120]

PGs and GAGs are essential to the functional structure of the cervix by regulating ECM assembly and attracting water into the tissue, which limits tissue volume changes in compression. Decorin, the primary PG in the cervix, binds to collagen and regulates fibril formation. [151] The amount of decorin in the cervix decreases by 40-50% at the end of gestation[69,122], leading to disorganization of the collagen network within the ECM. Although PG content decreases at the end of pregnancy, the concentrations of sulfated GAGs and hyaluronan (HA), a free GAG in the ECM, increase. [119,123,132,153,162,166] As expected from the increase in GAGs, the water content of the cervix also increases by approximately 5% in the third trimester[69,118], which is associated with a decrease in collagen organization[145] and more compliant tissue behavior.

Table 2.1. Changes in the ECM near term and the resulting effects on the cervix

ECM Constituent	Change during pregnancy	Resulting Effect
Total collagen content	↓	Decreased tissue strength
Collagen solubility	↑	Less organized collagen and decreased cross-linking
Decorin (primary PG)	↓	Disorganization of collagen
Sulfated GAGs and hyaluronan	↑	Increased tissue hydration and decreased collagen organization

Stiffness changes of the cervix during pregnancy

Several studies have shown quantitatively that cervical softening occurs gradually throughout pregnancy[16,31] with at least an order of magnitude decrease in confined compressive strength between a ripened, term cervix (E = 1.6 kPa)[119] and a non-pregnant cervix (E = 122 kPa). [45,81,119,120,146] This trend is consistent with observations reported by physicians using digital palpation. Among all gestations tested, pregnant tissue was significantly more deformable than non-pregnant tissue and did not exhibit a nonlinear stiffening response with increasing strain that is typical of biological tissue. [40] Instead, pregnant tissue continued to elongate under constant load, suggesting an increase in hydraulic permeability.[119] Decreases in strength of the non-pregnant cervix were also observed with previous vaginal deliveries, agreeing with clinical observations of decreased labor times with increased number of vaginal deliveries.[119]

Cervical insufficiency

Cervical ripening is a necessary process to allow for successful vaginal delivery of the fetus; however, the timing of this ripening process is critical for the outcome of the pregnancy. Cervical insufficiency, or premature cervical ripening, is diagnosed if a cervix is not stiff enough to support the pregnancy to term. It is sometimes suspected mid-pregnancy (20 weeks gestation) when funneling or shortening of the cervix is observed during a routine ultrasound. However, cervical insufficiency is asymptomatic resulting in non-painful cervical dilation and thus often goes undetected until after a patient experiences preterm labor or a second or third trimester miscarriage. In an effort to understand what causes cervical insufficiency, various studies have quantified the ECM constituents and mechanical properties of the insufficient cervix and compared them to the normal cervix. These studies have found decreased collagen content[141,146,163], increased collagen solubility[141], decreased elastin content[90,91,148], increased smooth muscle content, and decreased cervical resistance. [180] The combination of these results indicates that the insufficient cervix is more compliant than the normal cervix. Thus, a need arises in the obstetrics community for a non-invasive device that will safely and easily monitor cervical stiffness throughout gestation for the early detection of cervical ripening.

2.4 CURRENT CLINICAL ASSESSMENT OF THE CERVIX

Towards the end of the last trimester of pregnancy, a patient will undergo cervical exams by physical digital palpation at each prenatal visit and after labor has initiated. The purpose of these exams is to identify the biomechanical status of the tissue to determine probability of delivery. A qualitative analysis of the cervical dilation, effacement, station, consistency, and position are noted and compiled to determine a Bishop score.[20] The larger the Bishop score, the closer the cervix is to being fully ripe. This subjective analysis is not consistent among physicians and only considers the external *os* of the cervix. Despite these flaws, the Bishop score is the current standard in obstetrics for assessing cervical ripening.

To better understand the condition of the cervix, physicians can couple the Bishop score assessment of the external *os* with a transvaginal ultrasound (TVUS). During a TVUS, the technician assesses the length of the cervix as well as any funneling that may occur at the internal *os*. Women with a shorter cervix are at a higher risk for spontaneous preterm delivery.[71,125] Yet length of the cervix is not a definitive predictor of preterm delivery. The shape of the cervix as visualized with a TVUS can indicate the presence of remodeling within the tissue. Figure 2.4 shows the closed state of the cervix (T) as well as the progression of geometric changes that occur with cervical thinning and dilation prior to delivery (Y, V, U).[70] Prior to term the cervix should have a T configuration. If the Y, V, or U configurations are observed then cervical softening and remodeling has begun. Although TVUS provides a better quantitative assessment compared to the Bishop score, it is limited by not being able to measure the material properties of the tissue. Before geometric changes occur in the cervix, the stiffness of the tissue must decrease. The ability to monitor cervical stiffness throughout pregnancy could improve cervical consistency assessment during gestation, which could provide insight into the timing of delivery, predict the success of induced labor[15], and suggest the presence of cervical insufficiency prior to shortening and funneling of the cervix.

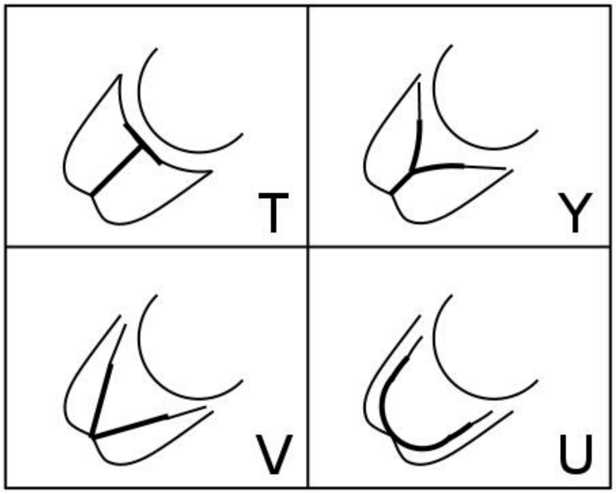

Figure 2.4. Cervical morphology during pregnancy and in preparation for delivery. T is the normal state of the cervix prior to ripening; Y, V, and U illustrate the progression of changes that occur with cervical thinning and dilation prior to delivery. This process is known as funneling of the cervix. [70]

2.5 IN VIVO MEASUREMENT OF CERVICAL STIFFNESS

Few studies have successfully quantified the stiffness of the cervix *in vivo*. Assessing cervical stiffness, especially during pregnancy, is difficult since the test must not compromise the mechanical integrity of the tissue. Two instruments have been developed and clinically tested to quantify cervical mechanical properties *in vivo*: the cervicotonometer[32] and an aspiration device. [106]

The cervicotonometer, developed by Cabrol et al. [32], records the force required to open the cervix and the resulting distance traveled during this process. These two parameters were used to calculate a “cervical distensibility index” (CDI), where an increase in CDI indicated cervical softening. They observed that the CDI was 5.9 times greater at term compared to the non-pregnant cervix and that CDI increased gradually as gestational age increased. Although this device provided a quantitative measure of cervical stiffness, it cannot be safely used during late gestation since it could induce labor. Additionally, the device must be very stable to give reproducible results and induces a radial force instead of compressive, which may not be physiologically relevant.

The second device, developed by Mazza et al[106], applies a negative pressure to the external *os* of the cervix and shows the displacement profile of the tissue into the device. By recording the magnitude of pressure and displacement profile of the tissue, a stiffness parameter was defined. When tested on cervical tissue *in vivo* and *in vitro* the device produced similar results proving its reproducibility. It was also shown that the pregnant cervix is more compliant than the non-pregnant cervix with a gradual decrease in stiffness throughout gestation. This device holds greater clinical relevance than the cervicotonometer because it applies a force along the same axis as the *in vivo* loading of the fetus on the cervix. However, it has a limited displacement range (1-3 mm) so it only measures surface tissue at the external *os*. It cannot provide quantitative information on changing properties deep within the cervical tissue.

2.6 ULTRASOUND ELASTOGRAPHY

In recent years, ultrasound elastography (UE) has emerged as a unique, non-invasive method for estimating tissue stiffness *in vivo*. UE couples traditional ultrasound with a strain dimension to measure applied *in vivo* tissue strains.[128] During imaging, the technician applies a cyclic load to the tissue with the transducer probe. In real-time, a color map is displayed over the B-mode ultrasound image depicting the strains measured within the field of view. The color scale is generated based on the maximum (red) and minimum (blue) strains measured. From these strain values, differences in tissue stiffness can be inferred by assuming that under the same load a soft tissue will strain more than a stiff tissue.[128] This concept can be modeled with springs in series (Figure 2.5). Therefore, current elastography images only suggest relative differences in moduli within the image, where the blue areas of the image represent "stiffer" tissue and the red areas represent "softer" tissue. This analysis of elastograms has successfully been used to diagnose tumors in breast tissue[5,74,160] and prostate tissue[114], as well as to diagnose liver diseases.[59]

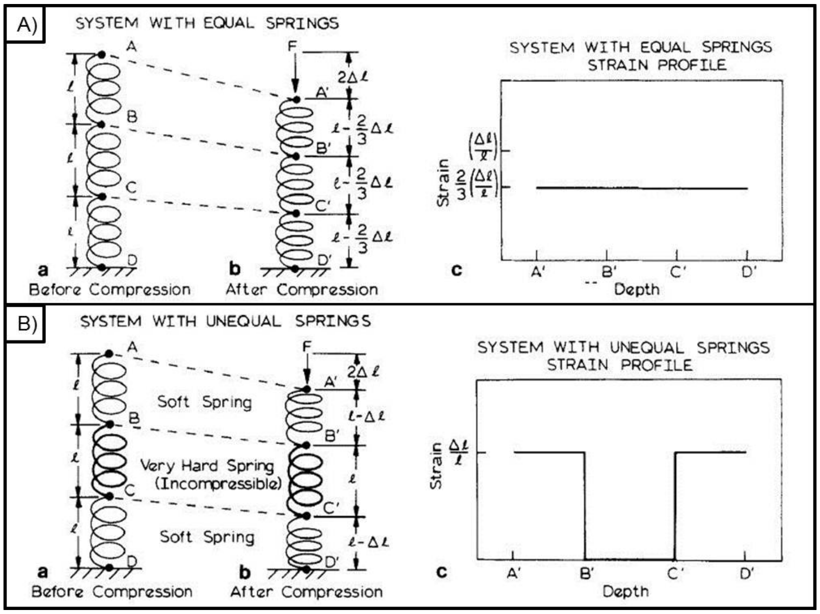

Figure 2.5. Ultrasound elastography tissue strain dimension is modeled with springs in series. When the springs in series have equal spring constants (stiffness) the strain is constant in each spring (A). Springs that have unequal spring constants (stiffness) respond with differing strains, which are expressed in the elastography images (B). [128]

As more is understood about ultrasound elastography and its capabilities, new applications for this technology continue to emerge, including monitoring the stiffness of the cervix through pregnancy. Several groups have conducted proof of concept studies to investigate whether UE is a valid method for assessing cervical stiffness. Differing strains were observed with location on the cervix and when comparing normal to abnormal cervixes (Figure 2.6). [66,115,159,161,175] Additional studies used UE to assess the ability to predict successful induction of labor. [158] They assigned a numeric scale, termed the elastography index (EI), to the colored strain map (purple = 0, blue = 1, green = 2, yellow = 3, red = 4) so that larger EI values indicated larger strains. Correlations were discovered between successful induction and larger EI values at the internal *os*, while failed inductions correlated with lower EI values at the internal *os.* Although these combined studies indicated that UE could be used in the future to assess cervical stiffness, they consistently concluded that it only provides a qualitative analysis of the cervix and more work is needed to standardize image collection and analysis to estimate cervical modulus. Additionally, several reports observed that the measured strain was dependent upon the distance from the probe rather than material property differences. [64,66,115] Further work needs to be conducted to characterize and correct for the strain dissipation caused by the compression of a small, spherical probe (*e.g.* transvaginal transducer probe) into the tissue.

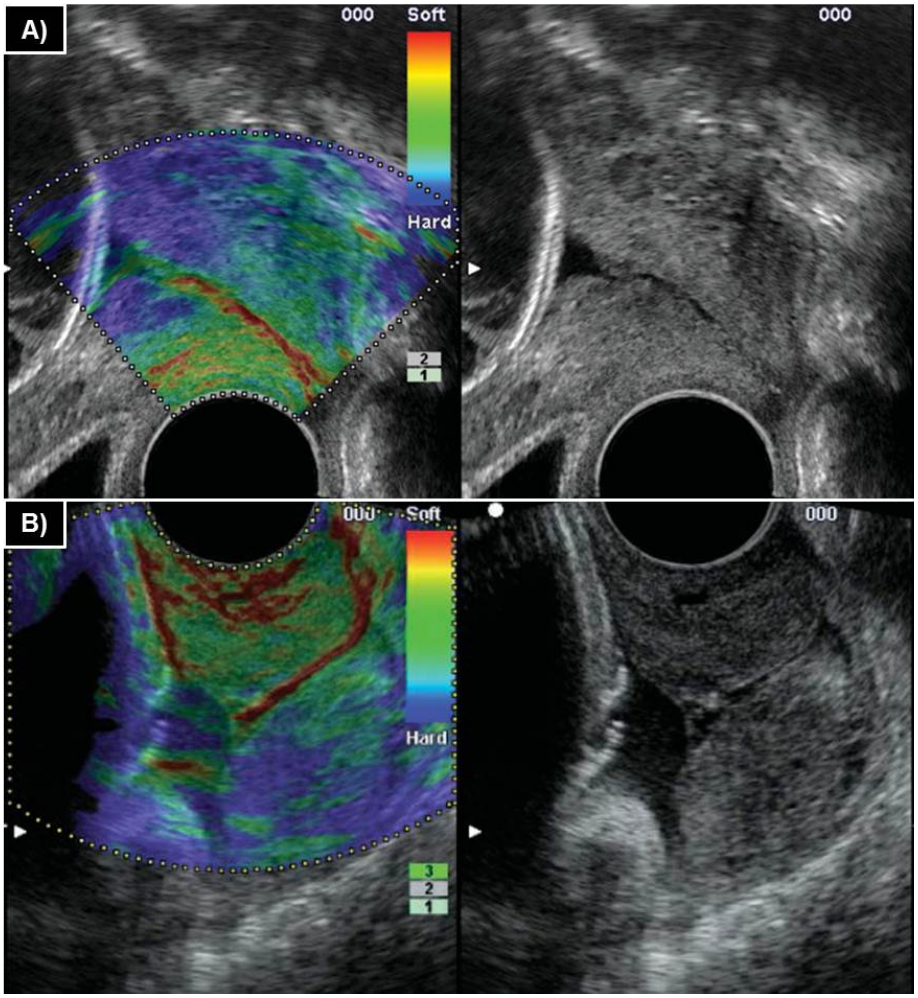

Figure 2.6. Ultrasound elastography images of a cervix at (A) 28 weeks gestation[159] and (B) 24 weeks gestation. [175] Cervical canal is identified at the red line. The corresponding standard B-mode, grey-scale ultrasound images are located to the right.

To standardize UE image analysis and determine cervical modulus, the stress in the tissue must be ascertained. This can be achieved by either using a force transducer[77] to measure the force applied to the tissues or by incorporating reference materials of known stiffness into the images.[38,64,176] The use of a force transducer may seem desirable because of the directly quantifiable measure it can produce; however, it is not trivial to accurately measure the low magnitude loads that cause the small strains necessary for UE. Furthermore, integrating a force transducer device onto a transvaginal transducer probe would likely be painful or intimidating to the patient. Incorporating a reference material that conforms to the ultrasound transducer probe, particularly when using a transvaginal transducer probe, is less likely to cause discomfort or anxiety in the patient. The use of a reference material involves a one-dimensional, linear Hooke's law expression (Equation 2.1) to calculate the modulus (a measure of stiffness) of the tissue. It is assumed that the stress, σ, in the reference material is equal to the stress in the tissue. Therefore, the modulus of the tissue (E_T) is calculated using the known modulus of the reference material (E_S) and the strain ratio between the reference material and the tissue ($\varepsilon_S/\varepsilon_T$) that is measured with UE (Equation 2.2).

$$\sigma = E\varepsilon \tag{2.1}$$

$$E_T = E_S \frac{\varepsilon_S}{\varepsilon_T} \tag{2.2}$$

Specialized UE software has been developed and implemented on select systems to allow the user to select regions of interest (ROI) to display the mean strain value and calculate the strain ratio between two regions of interest that is necessary for the use of equation 2.2. Chino *et al.*[38] and Yanagisawa *et al.*[176] demonstrated the reliability and validity of this technique for measuring the Young's modulus of muscular tissue using a linear transducer probe. However, demonstrating this technique on the cervix using a transvaginal transducer probe is underexplored in the literature.[64]

Cervical elastography images are biased by a strain dissipation that results from indenting a half space (tissue) with a spherical indenter tip (transvaginal transducer probe). This phenomenon has been reported in several studies that observed an increased strain directly under the transducer probe, which decreased with distance from the probe[64,66,115], but no study has implemented a Hertzian contact mechanics formulation to correct the strain data in the cervix.

Hertzian contact mechanics states that when indenting a half space (assumed to be the imaged tissue) with a spherical probe (transvaginal transducer probe) the generated stress field within the half space dissipates non-linearly as a function of distance into the half space.[75] The classic approach for determining the stresses and strains within the half space was derived by using the theory of potential.[25,35] Assuming a purely normal pressure, *p(ξ,η)*, two potential functions (ψ and ψ_1) can be defined within the loaded area *S*:

$$\psi_1 = \int_S \int p(\xi,\eta) \ln(\rho + z)\, d\xi d\eta \tag{2.3a}$$

$$\psi = \frac{\delta\psi_1}{\delta z} = \int_S \int p(\xi,\eta) \frac{1}{\rho} d\xi d\eta \tag{2.3b}$$

where ρ is the distance between a general point *C(ξ,η)* that lies on the surface of the half space within the loaded area *S* and a general point *A(x,y,z)* that lies within the body of the half space. The components of elastic displacement (u) at any point *A(x,y,z)* within the solid can then be expressed in terms of the defined potential functions:

$$u_x = -\frac{1}{4\pi G}\left\{(1-2v)\frac{\delta\psi_1}{\delta x} + z\frac{\delta\psi}{\delta x}\right\} \tag{2.4a}$$

$$u_y = -\frac{1}{4\pi G}\left\{(1-2v)\frac{\delta\psi_1}{\delta y} + z\frac{\delta\psi}{\delta y}\right\} \tag{2.4b}$$

$$u_z = \frac{1}{4\pi G}\left\{2(1-v)\psi - z\frac{\delta\psi}{\delta z}\right\} \tag{2.4c}$$

where G and v are the shear modulus and Poisson's ratio material properties of the half space, respectively. Substituting equations 2.3 and 2.4 into the three-dimensional Hooke's law formulations, the equations for stress (σ) at any point in the half space can be defined as:

$$\sigma_x = \frac{1}{2\pi}\left\{2v\frac{\delta\psi}{\delta z} - z\frac{\delta^2\psi}{\delta x^2} - (1-2v)\frac{\delta^2\psi_1}{\delta x^2}\right\} \tag{2.5a}$$

$$\sigma_y = \frac{1}{2\pi}\left\{2\nu\frac{\delta\psi}{\delta z} - z\frac{\delta^2\psi}{\delta y^2} - (1-2\nu)\frac{\delta^2\psi_1}{\delta y^2}\right\} \tag{2.5b}$$

$$\sigma_z = \frac{1}{2\pi}\left\{\frac{\delta\psi}{\delta z} - z\frac{\delta^2\psi}{\delta z^2}\right\} \tag{2.5c}$$

Hertz theory[67] defines the pressure distribution within the half space necessary to solve for the potential functions in equation 2.3. To solve for the pressure distribution, several assumptions must be made about the dimensions of the half space and the contact. Defining the contact area of the indenter tip into the half space as *a*, the radius of the indenter tip as *R*, and the significant dimensions of the half space as *l*, the assumptions in the Hertz theory are described as follows:[75]

(i) The surfaces are continuous and non-conforming: $a<<R$;

(ii) The strains are small: $a<<R$;

(iii) The material being indented is an elastic half space: $a<<R$, $a<<l$;

(iv) The surfaces are frictionless.

The pressure distribution within the half space can then be defined as:

$$p = p_o\{1-(r/a)^2\}^{1/2} \tag{2.6}$$

where p_o is defined as the maximum pressure within the half-space and *r* is defined as the distance from the z-axis to the point of interest.

In the case of cervical elastography, the most accurate measure of strain is located directly under the apex of the transducer probe[64]; therefore, the stresses and strains of interest are located along the z-axis. Using equations 2.3, 2.5, and 2.6, the stresses along the z-axis ($r = 0$) can be expressed as:

$$\sigma_z = -p_o\left(1+\frac{z^2}{a^2}\right)^{-1} \tag{2.7a}$$

$$\sigma_x = \sigma_y = -p_o\left[(1+\upsilon)\left(1-\frac{z}{a}arctan\frac{a}{z}\right) - \frac{1}{2}\left(1+\frac{z^2}{a^2}\right)^{-1}\right] \tag{2.7b}$$

The strains that are measured during UE can be set equal to the strain in the z-direction. Assuming that the strains in the x and y directions are equal (due to geometric symmetry) and substituting equation 2.7 into the three-dimensional Hooke's law formulations, the strain within the half space along the z-axis and in the z-direction can be solved as:

$$\varepsilon_z = \frac{p_o}{E}(1+\upsilon)\left[2\upsilon\left(1-\frac{z}{a}arctan\frac{a}{z}\right)-\left(1+\frac{z^2}{a^2}\right)^{-1}\right] \tag{2.8}$$

where E is the Young's modulus of the half space. The maximum pressure, p_o, due to a Hertzian pressure distribution is expressed as:

$$p_o = \frac{2}{\pi}\frac{E^*a}{R} \tag{2.9}$$

where E^* is defined as:

$$E^* = \frac{E}{1-\upsilon^2} \tag{2.10}$$

Substituting equations 2.9 and 2.10 into equation 2.8, the ultrasound elastography strain profile along the z-axis can be expressed as:

$$\varepsilon_z = \frac{2}{\pi}\frac{(1+\upsilon)}{(1-\upsilon^2)}\frac{a}{R}\left[2\upsilon\left(1-\frac{z}{a}arctan\frac{a}{z}\right)-\left(1+\frac{z^2}{a^2}\right)^{-1}\right] \tag{2.11}$$

The observed strain dissipation within a tissue that is imaged with a transvaginal transducer probe can be characterized using equation 2.11.

2.7 ANATOMY OF THE PLACENTAL MEMBRANES

The placental membrane, the sac that surrounds the fetus *in utero*, consists of three macroscopic layers: the amnion, the chorion, and the decidua (Figures 2.7 and 2.8). The amnion is the innermost layer (closest to the fetus). It is thin (~50 μm[3,133]), avascular, and composed of epithelial cells and connective tissue. It obtains its supply of nutrients and oxygen from the surrounding chorionic fluid, amniotic fluid, and fetal surface vessels. The amnionic epithelium rests on a basal lamina that is mainly composed of collagen IV fibrils[177], laminin[8], and heparan sulfate proteoglycans. [54] Laminin and collagen type IV perform a significant strengthening function in the amnion. [27] Attached to the basal lamina is the compact stromal layer. It contains collagen types I and III[95] and fibronectins[92] that are largely secreted by the amniotic epithelial cells. [8] This dense collagen layer contributes largely to the amnion tensile strength. [27] Additionally, the fibronectin in this layer is associated with collagen cross-links, which is critical for the mechanical properties of the membrane. The deeper portion of the amniotic mesenchyme, the fibroblast layer[23], contains a dense network of branched fibroblasts responsible for ECM and collagen synthesis.

The amnion is then loosely connected to the chorion at the spongy layer through bundles of collagen fibers (Figure 2.8), proteoglycans, and a few scattered fibroblasts. [23,52,110,142,149] The proteoglycans are composed of negatively charged GAGs and a protein core that consequently attracts water and results in tissue swelling. This unique property allows for the amnion to easily slide over the chorion at the spongy layer. [18,27]

The chorion is composed of connective tissue and embedded fetal blood vessels. The composition of the chorionic mesoderm is similar to that of the fibroblast layer of the amnion. The connective tissue is followed by a basal lamina, composed of laminin and collagen IV and shows accumulations of fibronectin and collagen III in its immediate surrounding. [8] Fibronectin is seen as the “glue” that holds cells together and is important in connecting the chorion to the maternal decidua. The trophoblast is separated from the chorionic mesoderm by this basal lamina. The trophoblast cells are connected by a system of partly dilated intercellular clefts. The clefts are filled with loosely arranged collagen fibers and bundles of a fine fibrillar material. [23]

The trophoblast then fuses with the decidua. The decidua, the only maternal component of the membranes, contains trophoblastic cells, maternal blood vessels, phagocytes, and other inflammatory cells.

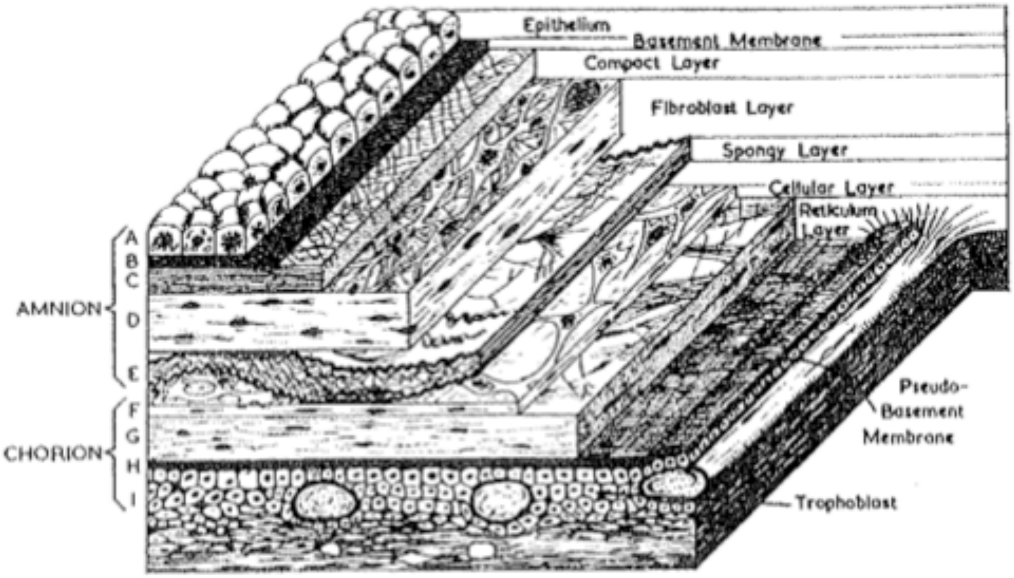

Figure 2.7. Structural organization of the chorioamnion showing the different layers that constitute the amnion and chorion. [24]

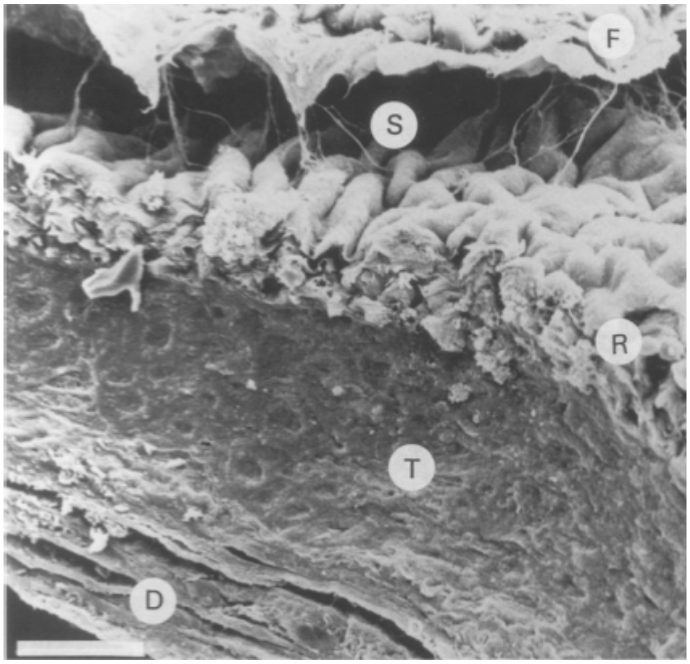

Figure 2.8. Scanning electron image of placental membranes showing the fibroblast layer (F), spongy layer (S), reticular layer (R), trophoblast layer (T), and the decidua (D). Fine fibers connect the amnion to the chorion at the spongy layer (x 1350). [52]

2.8 STRENGTH OF THE CHORIOAMNION

Three types of *ex vivo* testing apparatus have been used to characterize the mechanics of chorioamnion (CA): (1) uniaxial tensile testing[22,65,133,137], (2) biaxial inflation (burst) testing[6,86-88,94,139,143], and (3) biaxial puncture testing. [107,117,134,135,144,150] The tensile testing method involves placing the ends of a strip of CA membrane in vice grips and pulling the membrane in uniaxial tension. During the test, the force and displacement is recorded to calculate the mechanical properties of the tissue. Although this testing method is well understood, does not require large specimen dimensions, and is repeatable, the results can be seen as not physiologically relevant since the CA membranes *in vivo* are subjected to biaxial stretch forces. Burst testing most accurately replicates *in vivo* loading conditions with fluid pressure applied perpendicular to the plane of the membrane. However, it requires a large piece of membrane for each test and does not allow for multiple tests to be conducted with the same membrane to test for location variability. Additionally, the measured strength of samples tested via burst testing is in excellent agreement with values reported from uniaxial tensile testing[33], supporting our decision to use the well understood uniaxial tensile test in our studies. Puncture testing was developed to mimic the biaxial *in vivo* loading conditions of the membrane but requires smaller specimen dimensions than burst testing. Instead of applying fluid pressure to the membrane, a spherical metal probe is used to displace the central portion of the membrane perpendicular to the plane of its surface. Puncture testing has also been shown to validate uniaxial testing results[21], which further supports the use of the simplified uniaxial test method despite being criticized for not being physiologically relevant. When evaluating the results of each testing method only three findings are consistent in the existing literature: (1) the amnion is physically stronger and stiffer than the chorion; (2) the membranes demonstrate viscoelastic properties; and (3) the strength of an individual infant's membrane is not homogenous over its surface. [10,117]

Viscoelastic properties

The first to demonstrate the viscoelastic properties of chorioamnion were Lavery and Miller in the late 1970s. [87] They demonstrated that the CA membranes exhibited creep, stress relaxation, and non-recoverable deformation even at relatively minor intrauterine stretch forces. [86-88] Of increasing interest is the use of cyclic tests with increasing loading amplitude[88,117,136] given that the membranes are viscoelastic and subjected to cyclic loading during labor *in vivo*. Through these tests, the rupture strength and work to rupture were computed as a function of cycle number. [138] The amnion rupture strength was seen to increase with cycle number and the work to rupture decreased. However, after a large number of cycles the rupture strength eventually decreased. These patterns were not seen in the chorion. From these patterns, it was hypothesized that the collagen fibers in the chorion and amnion realign during initial stretch cycles and strain-harden the placental membranes.[117] Braxton-Hicks contractions may have the same strain hardening effect on the CA membrane *in vivo* thus making it brittle and easily ruptured.

2.9 CONTRIBUTORS TO MEMBRANE FUNCTION AND RUPTURE

The CA membrane serves a dual structural function throughout gestation. Prior to term it must remain intact to prevent leaking of amniotic fluid and to provide a physical barrier between the fetus and environmental conditions that may cause infection. At term the membrane is designed to rupture to allow the delivery of the fetus. The timing of rupture is critical to the outcome of the pregnancy. The studies discussed in this work will focus on three factors that could affect the timing of CA rupture during pregnancy: alteration of CA microstructure, biochemical/ECM changes, and material (tissue) property differences.

Structural changes to prepare for rupture

Previously, it was thought that the forces and stretching due to contractions during labor initiated the rupture process of the membrane. However, in approximately 10% of women membrane rupture preceded contractions.[117] The discovery of this trend caused a shift in placental membrane research. Researchers now propose that a remodeling process changes the primary collagen type(s) and alters ECM organization, which causes structural weakening and cellular apoptosis. There are several examples of this remodeling process documented in the literature. One study of term membranes that ruptured during labor showed a zone of extreme altered morphology characterized by swelling and disruption of the connective tissue as well as thinning of the trophoblast and decidual layers. [97] Another study verified these results by showing at the site of rupture a reduction of membrane thickness, dilation of intercellular canals, degenerative thinning of the trophoblast layer, and decreased numbers and disorganization of the collagen fibers in the fibroblast and spongy layers. [23] ECM remodeling was further confirmed through two histological findings of Caesarean section patients: the decidual layer was thinner and the FMMI (ratio of relatively acellular to cellular layers) was higher in the cervical zone. [109] Optiz and Bernoth[130] examined the membranes under polarized light and observed parallel "rupture lines" of collagen at the site of rupture indicating further reorganization in preparation for rupture.

Biochemical contributors to membrane rupture

In addition to the structural changes mentioned above, biochemical markers of both collagen remodeling and apoptosis have been studied. Moore et al. [85,116] treated membranes as well as isolated amnion with TNF and IL-1β *in vitro* in an effort to mimic the remodeling process that occurs *in utero*. The same biochemical markers of collagen remodeling and apoptosis were observed in the treated membranes that have been seen in the altered morphology zone of untreated membranes. [49] Other groups have shown that at term a decrease in fibronectin prepares the membrane for delivery. It has been shown that perturbations of the interaction between fibronectin and its integrin receptor may signal the cells to secrete destructive enzymes such as matrix metalloproteinases (MMPs). [27] Therefore, physicians have implemented the measurement of fibronectin to assess the risk of delivery, where a decrease in fibronectin indicates an increased risk of delivery.

Extracellular matrix degradation is controlled by MMPs, which are modulated by tissue inhibitors of MMPs (TIMPs). Specific types of MMPs attack specific collagen types, which further prepares the membrane for rupture. In the period directly before the onset of labor, MMP-1 dominates the concentration of active MMPs. MMP-1 breaks down collagen types I and III, the primary collagen types found in the amnion compact layer that provides strength to the membrane. This starts the weakening process in preparation for rupture. During the labor process, MMP-3 and MMP-9 increase in concentration. MMP-3 breaks down collagen types III and IV, proteoglycans, fibronectin, and laminin. Collagen type IV is found in the basement membrane along with proteoglycans and laminin. Fibronectin is in the compact layer and is a major contributor in connecting the chorion to the decidua. Therefore, MMP-3 further weakens the membrane by breaking down the basement membrane and removing the cross-links between collagen. By attacking fibronectin, MMP-3 also prepares the membrane to be delivered after the fetus. Proteoglycans are a major component at the interface between the amnion and chorion allowing them to easily slide over one another, so when this is removed it may allow the interface to delaminate easier. MMP-3 can also activate existing MMP-1 and MMP-9. MMP-9 degrades collagen types IV and V. Collagen type V is another contributor to amnion strength in the compact layer. Following delivery, MMP-1 and MMP-2 increase.[27] MMP-2 is another MMP that degrades collagen type IV.

Many factors have been studied that activate or alter the concentration of MMPs in the fetal membranes. One of these factors is apoptosis, programmed cell death. The same components that cause apoptosis, including stretch forces[50], also activate MMP-1, MMP-9[56,157], and MMP-2. [55] Therefore, it seems that the apoptotic process weakens the membranes by reducing the fibroblastic cell population that is responsible for producing new collagen while simultaneously activating MMPs that break down the surrounding extracellular matrix. [117] One of the MMPs, MMP-9 is also induced with prostaglandins (PGE2, PGF2α), interleukins (IL-1, IL-6, TNF-α), and reactive oxygen species. [9,30,108,165,178] Prostaglandins initiate and maintain uterine contractions. [156] The main source for prostaglandin E_2 (PGE_2) is the amniotic epithelium. [124] At the onset of labor, production of prostaglandins and interleukins increases which may explain why the concentration of MMP-9 increases with labor as well. [41,80,93,105,113,126,154] Amniotic fluid of pregnancies with preterm rupture of the membranes have increased expression of MMP-9[14,57,174] while TIMP-1, which inhibits MMP-9, is decreased. [57] Therefore, MMP-9 levels show promise for predicting membrane strength.[48,49,83]

Mechanical property differences near the site of rupture

As suggested by the observed zone of altered morphology discussed above, the strength of the membrane is not homogenous over its surface near term. These differences in mechanical properties have been observed in several studies that sampled specimens in various locations over the membrane. Generally, samples taken along the membrane tear line were weaker than those taken adjacent to the placenta. [11,12] Membranes taken from non-labored Caesarean sections also exhibit this weak zone over the cervix, characterized by decreased strength, work to rupture, stiffness, and ductility (displacement at rupture), suggesting that this process is largely biochemically regulated instead of solely by structural reorganization during labor. [49,116]

Changes in mechanical properties with gestational age

To further study the changes that occur in the CA in preparation for rupture, some studies have looked at membranes of differing gestational age. Several studies have shown that membranes prior to term have substantially greater mechanical integrity and the weak zone is small or absent compared to term membranes. [117,134,135,144] It has been hypothesized that this change in mechanical integrity is due to a change in collagen content, but there are conflicting reports as to whether the collagen content of the amnion decreases with gestational age. [99,155] Although the mechanism for weakening is not fully understood it is clear that there is a decrease in CA strength associated with increasing gestational age.

2.10 SEQUENCE OF MEMBRANE RUPTURE AND THE ROLE OF THE CHORIOAMNION INTERFACE

There have been conflicting reports regarding whether the chorion or amnion ruptures first. However, it seems that the majority of studies have shown that the chorion is the first to rupture. [12,86,117,135] The rupture sequence was described in great detail by Moore et al. [117] who reported intact membrane distention, separation of the amnion and choriodecidua, rupture of the choriodecidua, non-elastic further distention of the amnion, and ultimately amnion rupture. This rupture sequence suggests that the separation of the amnion and chorion plays an important role in membrane failure. [10]

The importance of the chorioamnion interface for intact CA membrane function and rupture has been identified but has been underexplored in the literature. Moore et al. [117] stopped puncture tests after only one layer had ruptured and discovered that the entire sample had delaminated, not just the portion that was under the probe. They also observed that the amnion and chorion were frequently separated following spontaneous rupture of the membrane and prior to delivery. This lead to the comparison of mechanical properties of intact chorioamnion to separated amnion and chorion. The strength of the intact chorioamnion was approximately equal to the sum of the separated amnion and chorion. However, the sum of the work to rupture of the individual amnion and chorion was only 54% of the work to rupture the intact chorioamnion. This difference in work to rupture is hypothesized to be, at least in part, due to the work required to separate the amnion from the chorion. Another study quantified the adhesive force of the interface using T-peel tests.[84] It was shown that the adhesive force decreased as the distance from the placental disc increased. This study was a preliminary quantification of the interface mechanical properties. However, the testing method did not provide any stiffening of the amnion or chorion to isolate the response to the interface nor did it provide physiologically relevant loading conditions to the interface. The chorioamnion undoubtedly experiences tremendous shear with fetal movements and uterine contractions, but the shear strength of the interface has not been investigated.

2.11 TIMING OF CHORIOAMNION RUPTURE

CA rupture can be described through six different categories depending on the timing of rupture. The first category is the natural, spontaneous rupture of the membrane (SROM). This is the most common form of rupture and occurs at term during labor. In some cases, a physician artificially ruptures the membranes (AROM) after labor onset. If the membrane ruptures at term but prior to the onset of labor, then it is considered premature rupture of the membrane (PROM). These first three categories are considered to be healthy membrane rupture. The fourth category is iatrogenic membrane rupture, occurring after/during medical interventions either for diagnostic or therapeutic purposes, and the fifth category is intrauterine rupture of the amnion portion of the CA membrane during fetal development in the first three months of pregnancy. The final category of rupture is preterm premature rupture of the membrane (PPROM), categorized as spontaneous rupture occurring prior to term (< 37 weeks gestation). This category is the most significant of the abnormal membrane rupture mechanisms due to the poor understanding what causes PPROM and the increased risk of infant morbidity and mortality that results from PPROM.

Differences in healthy membranes

To begin to understand what dictates the timing of membrane rupture, the mechanics, ECM constituents, and structural differences between these categories of rupture must be thoroughly studied. Little has been published about the differences between the three types of membrane rupture that occur at term. One study compared SROM and PROM membranes but found no differences in tensile rupture properties. However, there was thinning of the membrane near the site of rupture in PROM membranes. [12] Another study compared "clinically weak" (spontaneously ruptured prior to 3 cm dilation) membranes to "clinically strong" (artificially ruptured or ruptured post 8 cm dilation) membranes and found no difference in bursting tension. [43] Although these studies did not find any differences in failure strength there may be some other mechanism responsible for differences in membrane behavior *in vivo* that warrants further investigation. If the differences of healthy membrane behavior are understood, then the mechanisms that lead to unexpected rupture, especially of PPROM, may start to be elucidated.

Preterm premature rupture of the membranes

One unfortunate result of preterm rupture and thus the risk of preterm birth is infant mortality. In 2006, the percentage of infant deaths that were preterm-related was 36.1%.[104] The reason why some membranes fail preterm and some do not is poorly understood. Surprisingly, amnion from PPROM membranes has higher tensile strength than term membranes. [87] Therefore, it seems that tensile strength of the amnion does not fully indicate the behavior of the chorioamnion *in vivo*. Other reports have shown a local reduction of trophoblast cells, absence of decidua, edematous swelling of connective tissue, a dissolution of collagen fibers, and local activation of a variety of proteinases in the area of PPROM membranes overlying the cervix. [6,51,96,97] The overall content of collagen did not seem to differ so it seems that the distribution of isoforms, their cross-linking density, and the availability and activity of the respective cleaving enzymes may be of more importance. [27,78,98] Further studies are needed to determine the exact mechanisms responsible for differing responses of the membranes *in vivo* and why some membranes rupture preterm while others do not.

2.12 STUDIES IN THIS THESIS

The proposed work in this dissertation aims to detect tissue property changes that can result in preterm birth. During pregnancy, the cervix provides a foundation for the overlaying CA. When the internal os of the cervix softens and begins to funnel, the foundation for the CA diminishes, changing the loading conditions on the CA, and causing further distension of the membrane that can ultimately lead to CA rupture. **Therefore, we hypothesize that the cervix, the CA, and their substructures form a hierarchical and integrated load bearing system**

that undergoes mechanical failure to initiate birth. In particular, we hypothesize that alteration of ECM constituents, structure, and organization influences tissue material property losses, which in turn enables gross structural and functional tissue changes and, ultimately, tissue failure. The timing of this cascade is imperative to the outcome of the pregnancy, whether tissue failure leads to birth preterm (< 37 weeks gestation) or at term.

Specifically, we aim to enable quantitative evaluation of stiffness, or modulus, with UE by incorporating a reference standard of known stiffness into the image (Chapter 3). An analytical solution will be developed to correct for strain dissipation within the tissue during image collection by implementing a Hertzian contact mechanics solution (Chapter 4). We hypothesize that these novel methods for image collection and analysis will allow for direct comparison of images between patients and longitudinally throughout gestation, which could enable the estimation of the biomechanical state of the cervix and early detection of cervical insufficiency. This dissertation further aims to elucidate the role of microscopic length scale contributors to macro tissue function in CA membrane failure by studying the mechanical properties, ECM constituents and structural organization of CA membranes that ruptured spontaneously versus artificially at term (Chapter 5). We hypothesize that the ECM and tissue property changes in normal, term membranes that have differing modes of rupture can elucidate the mechanisms responsible for preterm premature rupture of CA membranes.

CHAPTER 3

DEVELOPMENT AND VALIDATION OF ULTRASOUND ELASTOGRAPHY REFERENCE MATERIALS FOR SEMI-QUANTITATIVE MEASUREMENT OF CERVICAL TISSUE STIFFNESS *IN VIVO*

3.1 ABSTRACT

Ultrasound elastography (UE) provides a non-invasive, facile method to safely assess tissue properties *in vivo*. For UE of the cervix, a transvaginal probe compresses the cervical tissue in an oscillating fashion where pre- and post-compression A-line pairs are cross-correlated to produce a strain profile within the displaced tissue. However UE requires standardization to convert the strain measurements to a modulus that evaluates tissue stiffness. We aim to improve UE and, ultimately, current clinical practice for non-invasive *in vivo* tissue stiffness assessment through the use of calibrated reference standards. Nine polydimethylsiloxane (PDMS) materials were fabricated with a compressive modulus range of 8.9 ± 1.3 kPa to 1310 ± 26 kPa by varying the elastomer base to cross-linker ratio from 60:1 to 10:1. Three tissue phantoms of varying compressive modulus (Stiff: 55.95 ± 5.49 kPa, Mid-range: 19.39 ± 4.46 kPa, and Compliant: 7.28 ± 2.02 kPa) were evaluated using UE while overlaying the PDMS reference standards on

the transvaginal probe. The UE strain ratio, between each standard and phantom, was used to predict the tissue phantom stiffness using a one-dimensional Hooke's Law constitutive equation that linearly relates stress to strain through a proportionality constant characteristic of the strained material, termed modulus. At depths 12.5 mm into the phantoms, the 50:1 PDMS (41.4 kPa) standard estimated the compliant phantom modulus within 12% error while the 40:1 PDMS (93 kPa) standard estimated the mid-range and stiff phantom moduli within 16% and 36% error, respectively. The estimates of modulus at depths greater than 12.5 mm into each phantom were inaccurate, thus necessitating further work to determine how to apply this method to tissues at greater distances from the probe. This study presents the potential for UE to measure a semi-quantitative value for *in vivo* tissue stiffness, which could enable direct comparison of images from multiple UE operators as well as data collected longitudinally from a single patient or across multiple patients, which may provide insight into cervical changes related to cervical insufficiency and preterm labor.

3.2 INTRODUCTION

Cervical insufficiency (CI) is diagnosed as premature softening of the cervix that can result in preterm labor or early termination of the pregnancy. This condition is asymptomatic and thus often missed until after a pregnancy loss. The difficulty in diagnosing CI is largely due to the inability to assess cervical stiffness at the internal *os* where softening is likely to begin. Ultrasound elastography (UE) holds promise for non-invasively measuring *in vivo* tissue stiffness; however, current techniques only reveal a qualitative analysis of measured displacements (*i.e.* strain), which cannot be compared between users, longitudinally in a single patient or across multiple patients. UE couples traditional B-mode imaging with a strain dimension to measure tissue displacements by compressing the transducer probe into the tissue in an oscillating fashion and cross-correlating pre- and post-compression A-line pairs to produce a strain profile within the displaced tissue. [129] The measured strains are displayed in a color strain map overlying the B-mode image, with red corresponding to the largest strain measured and blue corresponding to the smallest strain measured. However, the measured strain varies with both the magnitude of applied load and tissue stiffness heterogeneity. [128] Thus, the displayed strain map of the tissue only suggests relative differences in moduli (a measure of stiffness) within the image and not absolute measures of moduli. Only by standardizing the UE measurements of strain displacement can this technique be used to quantitatively evaluate tissue properties such as stiffness or modulus.

UE has been successfully used to detect stiff masses within soft tissue, such as breast and prostate tumors[4,36,60,74,76], through a qualitative comparison of measured strains in the tumor compared to surrounding fatty tissues; however, the cervix lacks a tissue in close proximity that can be used as a standard comparison. In an effort to quantitatively evaluate UE images of the cervix, Swiatkowska-Freund and Preis[158] established an elastography index that assigned a score to five different colors displayed on the resulting strain map (purple = 0, blue = 1, green = 2, yellow = 3, red = 4). The calculated elastography index, a measure of strain displacement at specific locations within each UE image, was used to numerically compare anatomical regions of interest between images. More recent developments in UE systems allow the user to display a numeric value representing the mean measured strain within a selected region of interest (ROI) within the image. With this information, users can calculate the strain ratio between two ROIs. [5,72,160] While both of the aforementioned methods have advanced UE towards an objective analysis, they are limited by quantifying measures of strain in the tissue that is displaced under the ultrasound transducer probe, which can change with the magnitude of applied force, geometry of the tissue, and surrounding tissue heterogeneity. Without simultaneous determination of the applied stresses (a measure of force or pressure) and of the resulting stress field underneath the transducer (distribution of force in the tissue), quantification of intrinsic tissue properties, such as modulus, cannot be determined through simple measures of strain.

To overcome these limitations, we propose the development of a technique in which a material property describing the stiffness of a material, such as modulus, is calculated from these images and used as a means of comparison. The modulus is determined through a linear relationship between the strain within a material and the applied stress. Here, strain displacement is quantified throughout the imaged region using UE. However, quantifying the stress applied by the probe to the underlying soft tissue is not trivial. This can be achieved by either using a force transducer[77] to measure the force applied to the tissues or by incorporating reference materials of known stiffness into the images. [38,64,176] The use of a force transducer may seem desirable because of the directly quantifiable measure it can produce; however, it is not trivial to accurately measure the low magnitude loads that cause the small strains necessary for UE. Furthermore, integrating a force transducer device onto a transvaginal transducer probe would likely be painful or intimidating to the patient. Incorporating a reference material that conforms to the transvaginal ultrasound transducer probe is less likely to cause discomfort or anxiety in the patient. It is assumed that the stress in the reference standard is equal to the stress applied to the tissue. Therefore, the stress can be calculated by multiplying the measured strain in the reference material by the known reference material modulus. [128] Chino *et al.* [38] and Yanagisawa *et al.* [176] demonstrated the reliability and validity of this technique for measuring the

Young's modulus of muscular tissue using a linear transducer probe. However, demonstrating this technique with a transvaginal transducer probe, where the geometry of this type of probe is much more complex, to measure cervical stiffness is underexplored in the literature.[64]

We aim to improve UE and, ultimately, clinical methods for non-invasive *in vivo* cervical tissue stiffness assessment. We hypothesize that incorporating calibrated reference standard materials that overlay a transvaginal ultrasound transducer probe will enable standardization of UE measurements. Such reference standards for UE need to possess a tunable modulus ranging over several orders of magnitude to accommodate different types of soft tissues, remain stable over several months and with repeated use, maintain properties despite being sterilized between patients, and exhibit elastic properties such as a constant modulus with cyclic loading and with varying loading frequency. Aside from the specified mechanical properties, the reference material cannot distort or shadow the ultrasound image and must produce sufficient backscatter for accurate strain measurements within the standard.

By including a reference material of known properties within every UE image, the resulting strain displacement throughout the tissue can be measured and subsequently normalized to the reference modulus, thus enabling determination of the moduli within the tissue directly underneath the transducer probe. Consequently, this proposed technique could allow for direct comparison of UE information between users, longitudinally in a single patient or across multiple patients. Achieving quantitative measures of *in vivo* tissue stiffness, or modulus, could improve diagnostic procedures that are reliant on detecting tissue stiffness changes. Additionally, the ability to compare images longitudinally in a single patient would enable physicians to monitor the progression of pathological tissue changes, such as cervical ripening prior to full term in pregnancy, and therefore improve timing of diagnosis and treatment.

In this study, we fabricated custom UE reference standards to satisfy the above requirements, characterized the compressive modulus of these materials, and validated their use with elastography. The reference standards were imaged for accuracy of estimating tissue phantom moduli and recommendations for measuring tissue stiffness with UE coupled with reference standards are suggested.

3.3 MATERIALS AND METHODS

Reference Materials Fabrication

Polydimethylsiloxane (PDMS) standards were prepared with a Sylgard 184 kit (Dow Corning, Midland, MI) and the elastomer base to cross-linker ratio was varied to produce standards of varying elasticity. Nine ratios of elastomer base to cross-linker (10:1, 20:1, 30:1, 35:1, 40:1, 45:1, 50:1, 55:1, and 60:1) were mechanically mixed for 10 minutes, degassed under vacuum for 30 minutes, and then cured at 130°C for 2 hours. Samples for mechanical characterization were cured in a glass petri dish and 8 mm diameter cylinders were cut from the bulk material for unconfined compression. Samples for UE were cured in custom aluminum molds following the above procedure to fit over a transvaginal ultrasound transducer probe.

Tissue Phantom Fabrication

Three tissue phantoms were prepared (compliant, mid-range, and stiff) by mixing 900 mL of boiling water with 36 g, 72 g, or 144 g of unflavored gelatin (Knox brand gelatin) and 18 g of sugar-free psyllium hydrophilic mucilloid fiber (brand name: sugar-free Metamucil).[28] A portion of the mixture was poured into a petri dish for mechanical characterization and the remaining mixture was poured into a plastic container (16 cm x 10.5 cm x 5.5 cm) for UE imaging; both mixtures were cooled until firm. 8 mm diameter cylinders were cut using a biopsy punch from the petri dish sample for mechanical characterization.

Quasistatic Mechanical Testing

Mechanical testing was performed using conventional materials testing methods to quantify the compressive moduli, a measure of stiffness, of both the PDMS standard and the gelatin tissue phantom materials. An MTS Insight 2 (MTS Systems Corp, Eden Prairie, MN) with a 5 N load cell was used to perform unconfined compression testing between two smooth metal platens. All height to diameter ratios of PDMS and gelatin mechanical testing samples were less than 2, according to the ASM Handbook[1] specifications for unconfined compression. Quasistatic behavior was observed with cyclic loading (n = 2 samples/PDMS standard). Samples were pre-loaded to 0.01 N and then compressed to a maximum of 10% strain at a rate of 0.25 mm/s for three cycles (this high strain rate minimizes the influences of material viscosity on the resulting material properties). The compressive modulus was defined as the slope of the final 20% of each stress-strain loading curve.

In initial UE image trials, the 50:1 PDMS standard experienced strains greater than 10% during imaging. Therefore, this standard was cyclically compressed to an initial strain of 10% for three cycles to match testing on the other PDMS materials. The strain was then increased in increments of 5% with three cycles per increment to a maximum strain of 25% to evaluate stress-strain relationships at greater strains.

To assess the validity of using PDMS as a UE reference standard, the compressive modulus was evaluated with aging, repeated use, and after sterilization. The compressive modulus of each PDMS standard (10:1, 20:1, 30:1, 35:1, 40:1, 45:1, 50:1, 55:1, and 60:1) was measured at one week, two weeks, 16 weeks and 26 weeks after fabrication (n = 2 samples/PDMS standard). New samples were cut for each time period from the same bulk material to characterize changes in modulus over time. To evaluate changes in modulus with repeated use, three samples were cut from the 20:1 and 50:1 PDMS standards and tested five times on the same day. Additionally, two samples of each PDMS concentration (10:1, 20:1, 30:1, 35:1, 40:1, 45:1, 50:1, 55:1, and 60:1) were cut to test for changes in modulus after sterilization. Compressive modulus was measured before sterilization, then PDMS standards were soaked in Cidex (Advanced Sterilization Products, Irvine, CA) for 12 minutes, wiped dry, (as is standard for sterilization of transvaginal ultrasound transducer probes in clinical practice) and mechanical properties were measured again. Sterilization was repeated for five cycles and the compressive modulus was measured after each cycle.

Dynamic Mechanical Testing

Dynamic mechanical analysis enables quantitative evaluation of properties, including measures of modulus, in viscoelastic materials that may vary as a function of the testing frequency (*i.e.,* strain rate). Here, one 5 mm diameter cylinder was cut from the 10:1, 20:1, 30:1, 40:1, 50:1 and 60:1 bulk PDMS standards for dynamic mechanical analysis (mean height: 2.28 ± 0.14 mm). Compressive frequency sweeps were performed using a TA Q800 (TA Instruments, New Castle, DE) with a preload of 0.01 N. The frequency was varied from 0.01 Hz to 10 Hz at 1% strain with 5 frequencies per decade. Storage and loss modulus were analyzed to assess changes in the elastic and viscous portions of the modulus as a function of loading frequency.

Effects of Silica on Mechanical Properties

To increase the number of boundaries in the PDMS standards that generate backscatter during ultrasound imaging, small particles of silica (Alfa Aesar, Ward Hill, MA), psyllium hydrophilic mucilloid fiber (brand name: sugar-free Metamucil), or air bubbles were added to the PDMS standards before samples were cured in the custom molds for UE imaging. PDMS standards with the added silica were the only material to repeatedly generate an easily attainable, homogenous elastography signal throughout the volume of the material. Therefore, all PDMS standards that were used for UE imaging contained a small concentration of silica (0.027 g of silica/g of PDMS).

To investigate the effects of added silica on the modulus of PDMS, samples of 20:1 and 50:1 elastomer base to cross-linker were prepared without silica, 0.0125 (g of silica)/(g of PDMS), 0.025 (g of silica)/(g of PDMS), and 0.0375 (g of silica)/(g of PDMS). Three 8 mm diameter cylinders were cut from each bulk material and quasistatic mechanical behavior was observed with incremental cyclic loading as previously described.

Quantification of Phantom Modulus using Ultrasound Elastography

PDMS standards (20:1, 30:1, 40:1, or 50:1 PDMS) were overlaid onto the transvaginal transducer probe (GE Model IC5-9-D, GE Healthcare, Austria) during imaging to include a material of known properties within the field of view for subsequent tissue modulus calculation. UE images of each tissue phantom were obtained with a GE Voluson E8 (GE Healthcare, Austria) and cini-loop video files were recorded for a minimum of 40 seconds per imaging session. A quality scale bar indicated if the tissue compression was in an acceptable range and if any unwanted lateral movements were detected by displaying green for good, yellow for fair, and red for unacceptable. Preliminary images indicated that the strain ratio between two consecutive sites within the standard and phantoms remained unchanged if this quality bar was in the yellow or green range. If the quality bar dropped to red the data from those frames were eliminated from the analysis. The 10:1 PDMS standard was excluded from image acquisition since its modulus is too large compared to the cervix (~2-57 kPa throughout gestation[119]). The force required to produce a measurable strain in the 10:1 PDMS standard would have caused large strains in the cervix and possible discomfort. Additionally, the 60:1 PDMS standard was too difficult to physically handle due to its compliance and so it was also excluded from UE image collection.

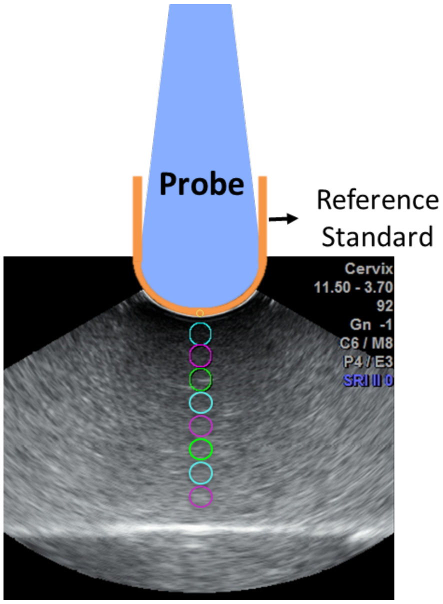

Figure 3.1. Gelatin phantoms were imaged with a transvaginal transducer probe and an attached PDMS reference standard. GE software was used to select circular regions of interest (ROI) on the ultrasound images to display the mean strain within each ROI. ROIs were placed in the standard and throughout the depth of the phantom.

GE software on the ultrasound system was used to select circular regions of interest (ROI) on the UE images. ROIs were identified in the standard and phantom located directly under the center of the probe. [64] Eight 5 mm diameter circles were lined up from top to bottom in the phantom to capture the strain profile through the depth of the phantom (Figure 3.1). The location of each circle was defined as the distance from the surface of the phantom to the center of the circle. The UE software displayed a graph of the mean measured strain over time for each selected circle. The strain data was extracted from these graphs using custom Matlab code (Matlab R2013b, The MathWorks Inc., Natick, MA). Strain ratios between the standard and ROIs in the phantom at each time point were calculated and analyzed using OriginPro (OriginLab, Northampton, MA). Hooke's law of elasticity, that relates the stress applied to an elastic material and the resulting strain through a proportionality constant termed modulus (E), was used to equate the calculated UE strain ratio to the ratio between UE phantom modulus (E_p) and PDMS standard compressive modulus (E_s) (Eq. 3.1),

$$^{\varepsilon_s}/_{\varepsilon_p} = {}^{E_p}/_{E_s} \tag{3.1}$$

where ε_s is the measured strain in the PDMS standard during UE imaging, ε_p is the measured strain in the phantom during UE imaging, and E_s is the compressive modulus of the PDMS standard measured with unconfined compression. The calculated UE phantom modulus (E_p) was then compared to the measured phantom compressive modulus from unconfined compression by calculating a percent error between the two measurements. This calculated percent error was used to evaluate the accuracy of using UE to calculate tissue modulus.

Viscoelastic materials can exhibit an increased modulus with increased strains. Therefore, it is important that the compressive modulus calculated with unconfined compression was determined at strains comparable to those experienced during image collection. To determine the strain experienced during image collection, representative DICOM images of the standard and phantom under compression during imaging and without any applied load were exported from each imaging session. ImageJ (US National Institutes of Health, Bethesda, MD) was used to measure the thickness of the PDMS standard and gelatin phantom to calculate the strain due to the application of force from the transducer probe during imaging. These values were compared to the unconfined compression testing protocol to ensure that the strain experienced during imaging matched the strain that the PDMS standards and gelatin phantom compressive moduli were measured at.

Statistical Analysis

Compressive moduli of the PDMS standards were examined for differences with aging, repeated use, sterilization, and addition of silica using Student's t-tests. Analyses were performed in R (R: A language and environment for statistical computing, Vienna, Austria). A value of $p < 0.05$ was considered to be significant.

3.4 RESULTS

Mechanical Characterization

The mechanical responses of PDMS standards under several conditions were characterized using unconfined compression to assess their ability to be used as a UE reference standard. The stress-strain response of PDMS at 10% strain displayed little to no variation in maximum force or modulus from cycle one to cycle three (Figure 3.2a). Results are thus reported as the mean compressive modulus of all three cycles. By evaluating the modulus as the tangent to the large strain, linear portion of each loading curve, the mean compressive moduli of the PDMS standards were determined as: 8.9 ± 1.3 kPa for the 60:1 PDMS standard, 18.2 ± 0.3 kPa for the 55:1 PDMS standard, 27.7 ± 2.3 kPa for the 50:1 PDMS standard, 50.4 ± 8.5 kPa for the 45:1 PDMS standard, 97.3 ± 2.8 kPa for the 40:1 PDMS standard, 170.9 ± 8.8 kPa for the 35:1 PDMS standard, 304.6 ± 15.6 kPa for the 30:1 PDMS standard, 701 ± 46.6 kPa for the 20:1 PDMS standard, and 1310 ± 26 kPa for the 10:1 PDMS standard (Figure 3.3). Table 3.1 summarizes the modulus changes observed in the PDMS standards with aging, repeated use, sterilization, frequency, and addition of silica. For all PDMS standards tested, the only change observed was during the dynamic mechanical analysis with an increase in storage and loss moduli with increased frequency.

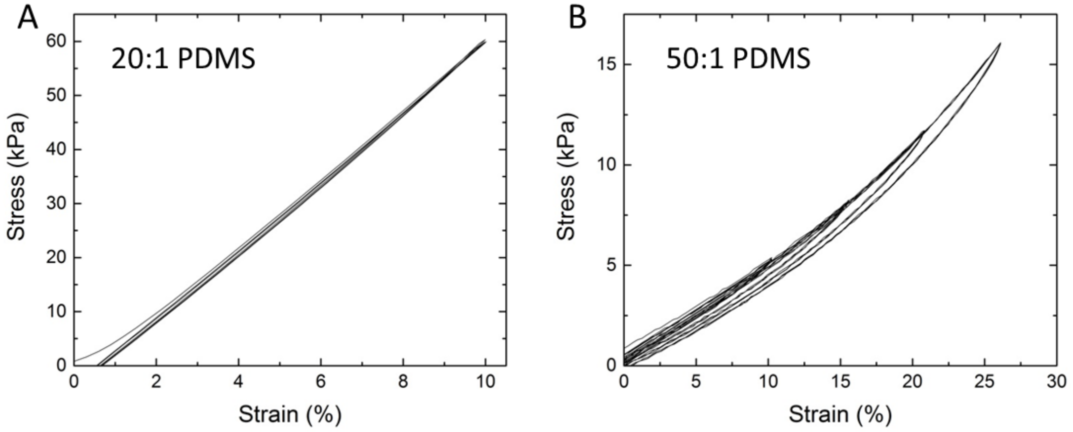

Figure 3.2. Representative stress-strain curves of PDMS standards tested in unconfined compression. All standards were cyclically loaded to 10% strain for 3 cycles (A) and the 50:1 was further incremented to a maximum strain of 25% (B) due to the large strains that the 50:1 standard experienced during imaging. Curves reveal little to no variation in hysteresis, maximum force, or modulus from the first to the third compression cycle at each strain increment thus indicating elastic-like behavior (*i.e.,* the properties of PDMS did not change with repetitive, cyclic loading).

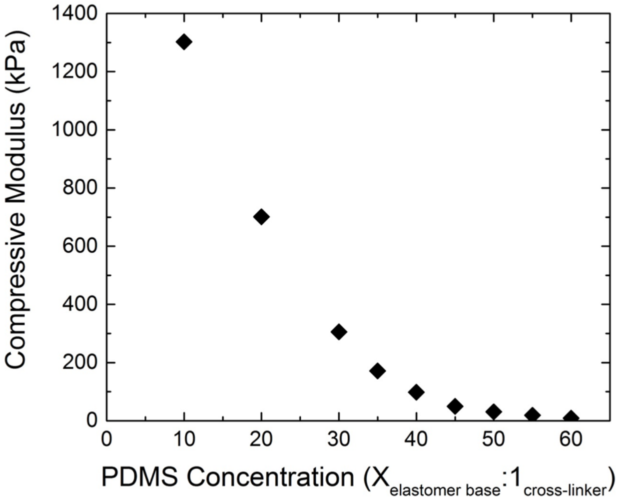

Figure 3.3. Mean compressive moduli from unconfined compression cyclic testing at 10% strain for all fabricated elastomer base to cross-linker ratios (10:1, 20:1, 30:1, 35:1, 40:1, 45:1, 50:1, 55:1, and 60:1) illustrate the versatility and tunablility of PDMS. The moduli achieved by varying the PDMS elastomer base to cross-linker ratios match those measured for soft tissues, including the cervix.[119]

Table 3.1. Summary of PDMS mechanical property changes observed with time, repeated use, sterilization, frequency, and small concentrations of added silica

Factors Tested	Outcome
Time	No significant change in compressive modulus from one week to 26 weeks after fabrication
Repeated use	No significant change in compressive modulus with five cycles of testing protocol
Sterilization	No significant change in compressive modulus after five sterilization cycles
Frequency	Storage and loss modulus increase from 0.01 Hz to 10 Hz
Addition of silica	No significant change in compressive modulus with the addition of up to 0.0375 grams of silica per gram of PDMS

Compressive moduli of the gelatin tissue phantoms were determined using the same protocol as the PDMS standards in unconfined compression. The stress-strain response of the gelatin tissue phantoms at 10% strain displayed a small decrease in maximum force and modulus from cycle one to cycle three, similar to biological tissue behavior (Figure 3.4a). This change in modulus with incremental loading cycles, however, was not significant. Thus, the compressive modulus was calculated as the mean modulus of all three cycles in the same manner as the PDMS standards: 7.28 ± 2.02 kPa for the compliant phantom, 19.38 ± 4.46 kPa for the mid-range phantom, and 55.95 ± 5.49 kPa for the stiff phantom (Figure 3.4b).

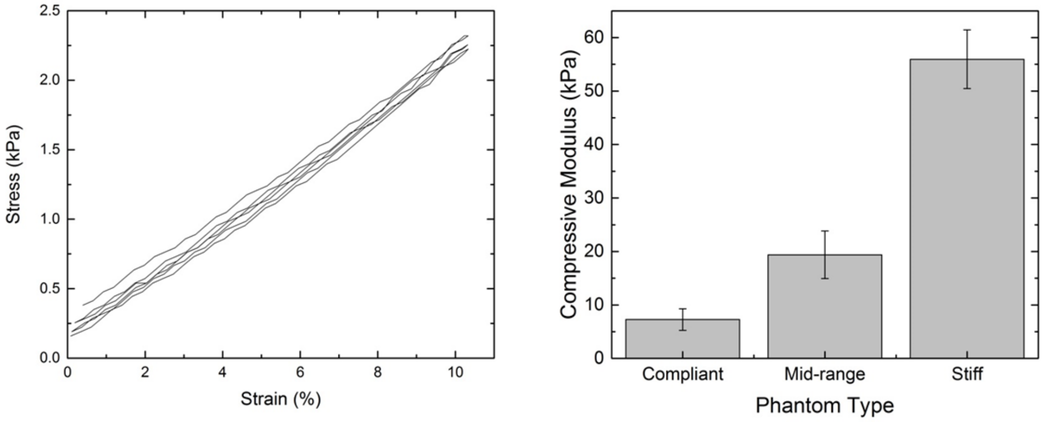

Figure 3.4. Representative stress-strain curve of phantoms in unconfined compression (left) and mean compressive modulus for each phantom (right).

DICOM images were collected before and during obtaining elastography images. From these images, the strain that the PDMS standards and phantoms experienced during UE imaging was calculated. This strain was then compared to the mechanical testing unconfined compression protocol to ensure that the strains were comparable. DICOM images of all three phantoms and all but the 50:1 PDMS standard underwent less than 10% strain during UE imaging; therefore, the compressive moduli of the three tissue phantoms and all but the 50:1 PDMS standard reported in figures 3.3 and 3.4b at 10% strain were used for tissue phantom modulus estimation (Eq. 3.1). The 50:1 PDMS standard experienced much larger strains, up to 25%. Therefore, the 50:1 PDMS standard was tested in unconfined compression to strains up to 25% and the compressive modulus at 25% strain (45.35 ± 4.0 kPa) was used for tissue phantom modulus estimation (Eq. 3.1). Even at these larger strains the 50:1 PDMS displayed little variation in maximum force and modulus from cycle one to cycle three within each strain increment (Figure 3.2b).

Quantification of Phantom Modulus using Ultrasound Elastography

UE images of each tissue phantom were obtained with a PDMS standard overlaying the transducer probe. Directly under the ultrasound probe, elastograms displayed a homogenous strain field through the PDMS standard and a decrease in strain with increasing distance into the phantom (Figure 3.5).

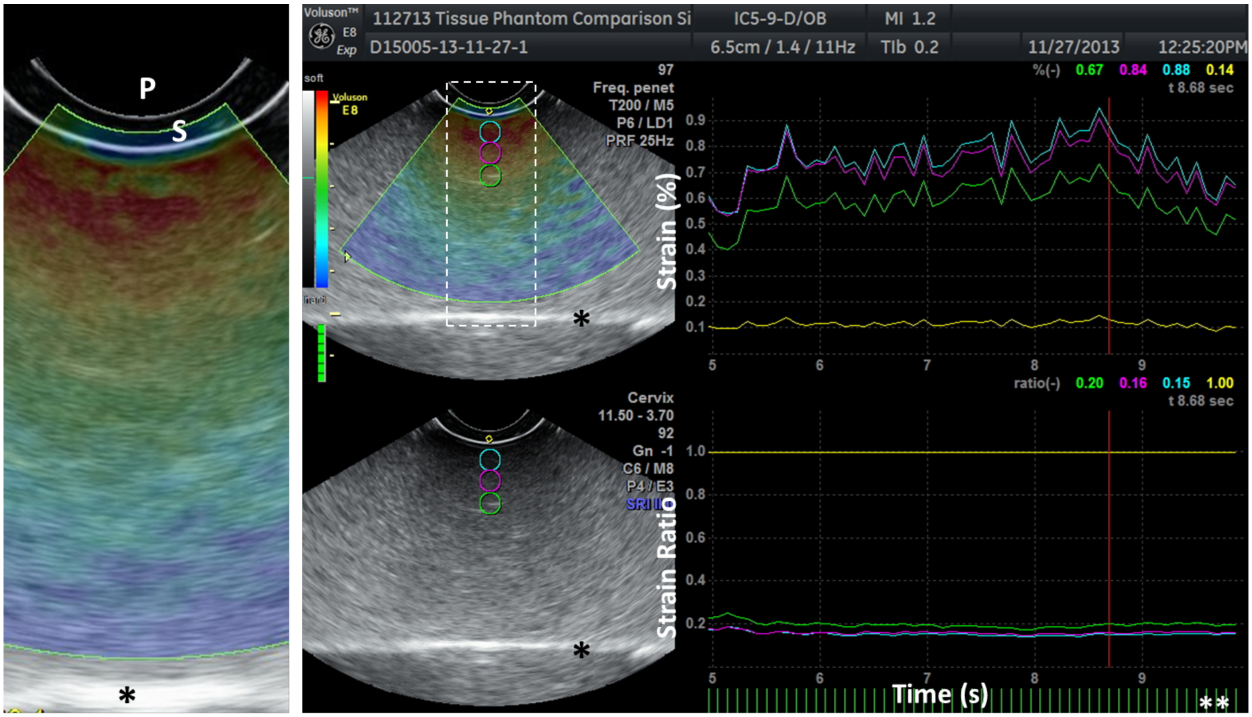

Figure 3.5. Representative ultrasound elastography image of the mid-range phantom as imaged with the 40:1 PDMS standard. The left inset shows the transducer probe (P) with the attached standard (S). Beneath the apex of the ultrasound probe, note the uniform strain pattern in the central region of the PDMS standard as well as a decrease in strain as a function of distance from the probe throughout the phantom as denoted by the color bar in the central panel (red = lowest strain displacement and blue = greatest strain displacement measured in the imaging session). The white line (denoted by *) represents the bottom edge of the phantom and was used to orient each measurement perpendicular to this surface. The mean strain within each selected ROI is plotted (top right) and the strain ratio between the standard and each circled ROI within the phantom is plotted (bottom right) as a function of time. The vertical green lines beneath these plots (**) indicate that the quality scale bar was within the green and yellow region during imaging.

Using linear Hooke's law to estimate the UE modulus of the phantom yielded results with a wide range of error that varied with two factors: 1) the modulus of the PDMS standard in combination with the modulus of the phantom being imaged and 2) the distance into the phantom at which the strain was measured (Figures 3.6 and 3.7). The compliant phantom modulus (7.28 kPa) was most accurately calculated when the 50:1 PDMS standard (45.35 kPa) was attached to the transducer probe. The mid-range (19.38 kPa) and stiff (55.95 kPa) phantom moduli were both calculated most accurately when the 40:1 PDMS standard (97.25 kPa) was attached to the transducer probe.

As the distance into each phantom was increased, the ability of Hooke's law to accurately predict the UE modulus of the phantom diminished. The compliant and mid-range phantom moduli were most accurately calculated at 7.5 mm from the top surface of the phantom, with errors of 13.6% and 9.5%, respectively, and the stiff phantom modulus was most accurately calculated at 2.5 mm from the surface of the phantom, with 42.9% error. For all PDMS standard/gelatin phantom combination, at depths greater than 12.5 mm into the phantom, Hooke's law predicted an increase in UE modulus diverging from known phantom compressive moduli values (Figure 3.6). The divergence in predicted UE phantom moduli, with increased depth into the phantom, was much greater for the stiff phantom compared to the compliant and mid-range phantoms (Figure 3.7).

The stiff phantom was more difficult to image due to the increase in force required to produce a measureable amount of strain through the depth of the phantom. This increase in force caused the 50:1 PDMS standard to experience large deformations that inhibited the ability to select an ROI located directly under the probe in the standard. Therefore, the 50:1 PDMS standard was excluded from the analysis of the stiff phantom.

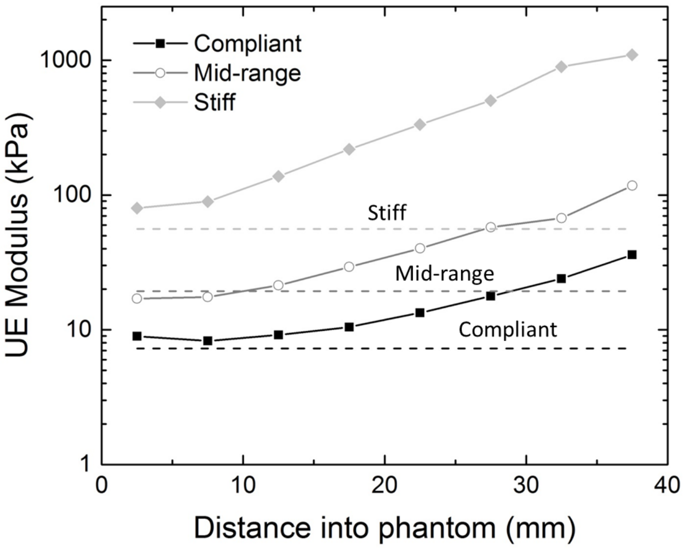

Figure 3.6. UE modulus of each phantom as a function of distance into the phantom. Dashed lines show the measured modulus of each phantom from unconfined compression mechanical testing data. The most accurate modulus calculations of each phantom are shown. This was obtained when the compliant phantom was imaged with the 50:1 PDMS standard and when the mid-range and stiff phantoms were imaged with the 40:1 PDMS standard.

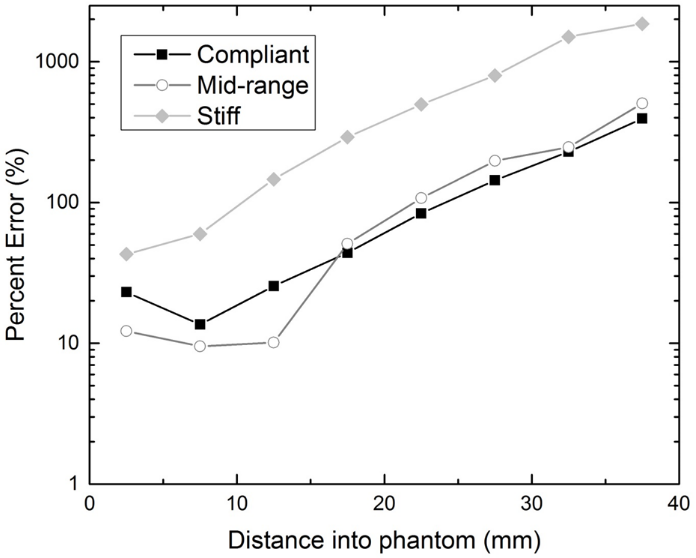

Figure 3.7: Percent difference between the phantom stiffness calculated using UE imaging and a linear Hooke's law approximation as compared to the measured phantom stiffness from unconfined compression testing. Data are plotted as a function of distance into each phantom.

3.5 Discussion

The aim of this study was to fabricate and validate standard reference materials that could be used to enable semi-quantitative assessment of tissue stiffness and thus to standardize ultrasound elastography (UE) imaging. UE reference standards were fabricated with a tunable modulus ranging over several orders of magnitude and so can be used with various different types of soft tissues. The reference standards fabricated in this study were shown to remain stable over several months, with repeated use, and after sterilization without altering material properties. During elastography imaging, the reference standards were cyclically loaded to large strains, up to 25%, without experiencing permanent damage and consequential property alterations. Furthermore, they returned to their original dimensions after unloading and did not vary in modulus while undergoing cyclic loading. In addition to the specified mechanical properties, the fabricated reference materials did not distort or significantly shadow the ultrasound image and produced sufficient backscatter for accurate strain measurements within the standard. Therefore, the reference materials fabricated in this study fulfill the requirements of a UE reference standard and hold promise for improving assessment of tissue properties and behavior during UE imaging.

To identify candidate materials that would enable standardization of strain displacement measurements in UE, several different materials were considered. While overlaying the probe with each candidate material, UE images were evaluated for spatial distortion, blurring and shadowing. Silicone and thermoplastic polymers produced shadowing that obscured anatomical features in the B-mode image. Thus, these materials did not meet the criteria for a UE reference standard. Additionally, polyethylene glycol dimethacrylate (PEGDM) and agarose hydrogels were too brittle to withstand the strains experienced during handling and imaging. PDMS was the only material tested to not cause image distortion or shadowing and to also not fracture during the imaging process and so was pursued as the most optimal candidate material.

The modulus of PDMS is tunable (*i.e.,* the modulus is easily controlled by affecting the elastomer base to cross-linker ratio), possesses near elastomeric properties, and is stable under varying conditions.[170] Here, a wide range of reference standard compressive moduli, 8.9 ± 1.3 kPa to 1310 ± 26 kPa, were obtained by varying the elastomer base to cross-linker ratio during preparation from 60:1 to 10:1, respectively. This range of moduli confirms the versatility and tunablility of PDMS, where modulus values compare well with experimentally determined *ex vivo* properties for human cervix.[119] The correct preparation of PDMS in our labs was verified by comparing with previously published values for 10:1 PDMS materials.[26,34,79,152,170] Moreover, we observed little variation of maximum force or modulus of PDMS with repetitive mechanical loading suggesting that PDMS can be considered an elastic material, thus enabling the use of linear Hooke's Law to determine stiffness of imaged phantom materials or tissues. PDMS is also a stable material that is unaffected by repeated use, aging, and sterilization with Cidex, the standard method for sterilizing medical devices between patients. While the compression modulus of PDMS varied as a function of the testing frequency in dynamic mechanical analysis, these parameters were stable at the relatively low frequencies (~2 to 4 Hz) that are applied during UE image collection and resulted in a modulus increase of less than 14% from 2 to 4 Hz. Overall, this work demonstrated that PDMS is a tunable and stable material that facilitates use in UE applications.

To increase the amount of backscatter, enhance UE image quality, and optimize accuracy of strain displacement measurements, the PDMS standards were fabricated with embedded silica particles. Although silica is a stiff particulate, the low mass fractions (< 3% by weight) added to the PDMS materials did not alter the compressive moduli of the standards.

When imaging tissue phantoms using UE, coupled with a standard reference material, the modulus of the selected reference material significantly influenced the accuracy of the calculated UE phantom modulus. Our results indicated a greater error between UE moduli and known compressive moduli of the phantoms when the PDMS reference standard modulus was considerably stiffer than the tissue phantom modulus. Additionally, if the PDMS standard was too compliant, compared to the tissue phantom, then the PDMS standard compressed too much for accurate strain measurements. This variance of calculated tissue phantom modulus with varying PDMS standard modulus was a large source of error that was not trivial to resolve. Thus, an objective method for PDMS standard selection that yields accurate tissue phantom modulus measurements will be the focus of future studies.

The heterogeneous strain distributions observed in the phantoms suggest that the distance at which the tissue stiffness is measured from the probe is also a variable that requires regulation. This is due to the fundamental relationships of Hertzian contact mechanics, which states that when indenting a half-space (i.e., a volume of material possessing a flat surface) with a spherical probe, the stress field that is generated within the half-space dissipates non-linearly with increased distance into the half-space. Furthermore, the rate of stress dissipation in the half-space is dependent on the contact depth (*i.e.,* the amount that the spherical probe is compressed into the half-space).[75] As the contact depth decreases, the rate of stress dissipation within the phantom increases,[75] causing stresses that are too small to produce accurately measured strains at the bottom of the tissue phantom. Our results indicated that a simple linear Hooke's law relationship could be used to calculate the tissue phantom modulus within 12.5 mm from the surface of the phantom if sufficient contact area was maintained. As the contact depth was decreased, as was the case for the stiff phantom, the distance into the phantom that linear Hooke's law accurately calculated the phantom modulus decreased. Additionally, while Hooke's law could be used to predict tissue phantom modulus, the accuracy of this approach decreased with increased distance into the phantom that the modulus was measured at. The effects of the spherical ultrasound transducer probe contacting the tissue phantom as described by Hertzian contact mechanics thus cannot be ignored, especially as the region of interest increases in distance from the probe. Therefore, a more complex Hertzian contact mechanics analysis is necessary to accurately estimate *in vivo* tissue stiffness and will be the focus of future studies.

The present study presents the potential to accurately and non-invasively measure *in vivo* tissue stiffness using UE. Current methods for determining *in vivo* tissue stiffness are generally invasive, posing the risk of infection, or lack an accurate quantitative measure of stiffness. Therefore, UE could be useful for a number of applications that require the detection of stiffness changes in soft tissues to assess the progression of normal changes in tissue stiffness (*e.g.,* cervical ripening in pregnancy), diagnose a pathological condition (*e.g.,* preterm cervical softening at the internal *os*), or determine the effectiveness of a therapy (*e.g.,* progesterone treatment for a short cervix in pregnancy. [147] Additionally, the use of standardized UE could enable differentiation of benign and malignant tumors in a variety of soft tissues to reduce the need for tissue biopsies[5,17,39,160], early diagnosis of conditions that present with an asymptomatic change in tissue stiffness such as cervical insufficiency[64,66], or the study of pathophysiology and biomechanics of conditions that alter the stiffness of soft tissues such as muscular dystrophies. [46] An imaging technique that can accurately and non-invasively detect changes in muscle stiffness would not only aid in the differential diagnosis of neuromuscular disorders but would also reveal important information about the progression of these disorders. In all of these examples, the need to accurately and non-invasively quantify *in vivo* tissue stiffness is evident.

In conclusion, PDMS was determined to be a suitable choice for use as a UE reference standard and produced accurate and repeatable measurements of tissue phantom stiffness at distances close to (< 12.5 mm) the point of contact between the transducer probe and the tissue phantom. Though promising, this method of measuring *in vivo* tissue stiffness has limitations that need to be addressed to enable reliable use of this technique in a clinical setting. To obtain the most reliable measure of tissue phantom modulus this study suggests: 1) imaging tissues at compression frequencies between 2 and 4 Hz, 2) selecting the modulus of the reference standard to minimize the differences between the reference standard modulus and the tissue modulus, 3) regulating contact depth to ensure sufficient contact between the standard and tissue, and 4) using linear Hooke's law to only estimate tissue stiffness within 12.5 mm from the surface of the tissue. Implementing these proposed strategies when performing UE may allow for a non-invasive, semi-quantitative measure of *in vivo* tissue stiffness in regions of tissue close to the ultrasound probe.

CHAPTER 4

IMPLEMENTATION OF A HERTZIAN CONTACT MECHANICS BASED FORMULATION FOR *IN VIVO* CERVICAL TISSUE STIFFNESS ASSESSMENT USING ULTRASOUND ELASTOGRAPHY

4.1 ABSTRACT

Cervical insufficiency, clinically diagnosed as premature cervical softening, is an asymptomatic condition that often goes undetected and may result in preterm labor or early termination of pregnancy. The current method for monitoring cervical consistency during pregnancy involves digital palpation to qualitatively assess the stiffness of the external *os*. However, cervical softening typically begins at the internal *os* – a region that is not easily accessible without substantial interventions. Ultrasound elastography holds promise for non-invasively monitoring cervical stiffness throughout pregnancy, but is also qualitative unless a force transducer or reference standard is used during image acquisition. Additionally, the transvaginal ultrasound transducer probe has a spherical tip that causes strain dissipation within the imaged tissue during compression. In this study, an analytical solution based on three-dimensional Hooke's Law relationships and Hertzian contact mechanics formulations is

developed and used to analyze UE images for semi-quantitative estimates of modulus obtained on tissue phantoms with an attached reference standard. The solution is validated using a finite element model and then applied to a non-pregnant cervix and two pregnant cervixes to demonstrate the feasibility of imaging human tissue *in vivo*. Using the analytical solution to calculate modulus of the tissue phantoms was significantly more accurate compared to the commonly used one-dimensional, linear Hooke's law approach and allowed for an objective and accurate method for reference standard selection. Additionally, cervical modulus values were obtained of the anterior lip that agreed well with previously published values. The results from this study indicate that ultrasound elastography with an attached reference standard holds promise for evaluating cervical stiffness throughout gestation and could improve early detection and diagnosis of cervical insufficiency.

4.2 INTRODUCTION

In 2011, 11.73% of all births in the United States were preterm (< 37 weeks completed gestation). [100] Babies born preterm are at risk for respiratory problems, vision problems, hearing impairment, feeding and digestive problems, cerebral palsy, and developmental delay. [2] Complications due to preterm birth are the leading cause of death among infants.[53] One known cause of preterm birth is premature cervical ripening (i.e., softening), diagnosed as cervical insufficiency.[47,53] Cervical insufficiency is asymptomatic and thus often goes undetected until after a patient experiences preterm labor or a second or third trimester miscarriage.

Cervical ripening typically starts at the internal *os* with remodeling that causes a decrease in stiffness, eventual funneling and decreased cervical length.[70] This softening process is necessary for uterine contractions to successfully dilate the cervix for delivery of the fetus.[53] However, the timing of cervical ripening is critical for the outcome of the pregnancy. Typically, cervical softening at the internal *os* goes undetected until the gross physical change in cervical shape can be detected with B-mode ultrasound imaging. Thus, when the cervix softens prematurely it often goes unnoticed increasing the risk for preterm delivery. The ability to measure cervical stiffness at the internal *os* could significantly improve early detection and diagnosis of cervical insufficiency.[53]

Current clinical practice for measuring cervical stiffness is performed near term (≥ 36 weeks gestation) via digital palpation of the external *os*.[20] Such observations are qualitative, do not reveal information about the internal *os*, and can vary widely between health care practitioners.[71] Additionally, these cervical checks are not typically performed earlier in pregnancy since they could unnecessarily introduce infection.

Alternative methods of quantifying cervical stiffness have been developed, yet a clear and precise method of noninvasively measuring cervical stiffness is still not available.[53] One device was developed that records the force to open the cervix to a specified diameter; however, this device cannot be used during late gestation since it could induce labor. [32] A second device was developed that applies a negative pressure within an aspiration tube and the displacement profile is analyzed to calculate cervical stiffness. [106] Although this aspiration device can be used without the risk of inducing labor, it only measures the stiffness of the external *os* and cannot provide quantitative information on changing properties deep within the cervical tissue. In recent years, ultrasound elastography (UE) has emerged as a unique method for measuring applied *in vivo* tissue strains (a normalized measure of displacement).[128] UE has thus been recognized as a powerful tool to qualitatively infer tissue stiffness (based on a simplistic one-dimensional, linear

Hooke's law relationship between strain and modulus); however, several researchers have incorrectly used UE to quantify tissue stiffness due to their lack of understanding of the fundamental mechanics that are involved. They have incorrectly used UE to compare images without knowledge of the force[5,72,160,161,175], without an applied compression[158], or without correcting for strain dissipation when using a transvaginal ultrasound transducer probe[64,66,115]. It is apparent that this technology provides potential for a non-invasive method to easily and safely monitor cervical stiffness throughout gestation; however, it is not as trivial as others have assumed. Thus, there exists a need to develop a standardized protocol for UE image collection and analysis.

To calculate a quantitative measure of tissue stiffness from the measured UE strains, the stress (a normalized measure of the applied force) in the imaged material must be ascertained. This can be achieved by either using a force transducer[77] to measure the force applied to the tissues or by incorporating reference materials of known stiffness into the images. [38,64,176] The use of a force transducer may seem desirable because of the directly quantifiable measure it can produce; however, it is not trivial to accurately measure the low magnitude loads that cause the small strains necessary for UE. Furthermore, integrating a force transducer device onto a transvaginal transducer probe would likely be painful or intimidating to the patient. Incorporating a reference material that conforms to the ultrasound transducer probe, particularly when using a transvaginal transducer probe, is less likely to cause discomfort or anxiety in the patient. For the incorporation of a reference material, the strain in the reference material is measured and displayed in the elastogram. The stress in the reference material, which is equivalent to the stress in the imaged tissue, can then be calculated by multiplying the strain in the reference material by the known reference material modulus. [128]

In our previous work, we have shown the successful use of reference materials coupled with UE to calculate tissue phantom stiffness using a one dimensional, linear Hooke's Law relationship (Chapter 3). The accuracy of this method to calculate stiffness diminished with increased distance into the phantom (> 12.5 mm), where the measurement is most needed in the cervix. The limited accuracy of the one dimensional Hooke's law method is due to the fundamental relationships of Hertzian contact mechanics, which states that when indenting a half-space with a spherical probe (e.g. a transvaginal ultrasound transducer probe) the generated stress field within the half space dissipates non-linearly as a function of distance into the half space.[75] Therefore, a Hertzian contact mechanics analysis is necessary to accurately measure *in vivo* tissue stiffness located at distances greater than 12.5 mm from the outer surface of the reference standard. An accurate measure of tissue stiffness would allow for direct comparison of UE information from multiple UE operators as well as data collected longitudinally in a single patient or across multiple patients at different distances within the tissue.

For this study, we aim to develop an analytical solution based on three-dimensional Hooke's Law relationships and Hertzian contact mechanics formulations to analyze UE images obtained on tissue phantoms with an attached reference standard. The solution is validated using a finite element model and then used to analyze images obtained on one non-pregnant cervix and two pregnant cervixes. Achieving a quantitative measure of *in vivo* cervical stiffness through gestation could improve early detection and diagnosis of cervical insufficiency.

4.3 MATERIALS AND METHODS

Reference Materials Fabrication

Polydimethylsiloxane (PDMS) standards were prepared with a Sylgard 184 kit (Dow Corning, Midland, MI) and the elastomer base to cross-linker ratio was varied to produce standards of varying elasticity. To increase backscatter in the standards during imaging, silica was added to each standard prior to curing (Chapter 3). Four ratios of elastomer base to cross-linker (20:1, 30:1, 40:1, and 50:1) were mechanically mixed for 10 minutes, 0.027 (g of silica)/(g of PDMS) was added and mechanically mixed for an additional 3 minutes, degassed under vacuum for 30 minutes, and then cured at 130°C for 2 hours in custom molds to fit over a transvaginal ultrasound transducer probe.

Tissue Phantom Fabrication

Three tissue phantoms were prepared (compliant, mid-range, and stiff) by mixing 900 mL of boiling water with 36 g, 72 g, or 144 g of unflavored gelatin (Knox brand gelatin) and 18 g of sugar-free psyllium hydrophilic mucilloid fiber (brand name: sugar-free Metamucil). [28] The mixture was poured into a plastic container (16 cm x 10.5 cm x 5.5 cm) and cooled until firm.

Mechanical Testing

An MTS Insight 2 (MTS Systems Corp, Eden Prairie, MN) with a 5 N load cell was used to perform cyclic unconfined compression tests of the PDMS standards and gelatin phantoms as previously described (Chapter 3). Compressive modulus was defined as the slope of the final 20% of each stress-strain loading curve.

Ultrasound Elastography Image Collection

UE images were obtained with a GE Voluson E8 (GE Healthcare, Austria) ultrasound system using a transvaginal ultrasound transducer probe (GE Model IC5-9-D, GE Healthcare, Austria) on each tissue phantom as well as three healthy women at the University of Colorado Hospital (COMIRB #11-0570). All participants were informed of the image collection protocol and risks associated with this study. Prior to image collection, each participant provided written informed consent. This portion of the current study was approved by the Colorado Multiple Institutional Review Board at the University of Colorado Hospital, Denver, CO.

Cervical elastograms were collected on a non-pregnant woman, an early gestation patient (7 weeks gestation), and a mid-gestation patient (26 weeks gestation). The participants had no preexisting serious health conditions and did not have any indications for preterm delivery (*e.g.* preeclampsia). Images were collected perpendicular to the cervical canal so that the orientation of the elastogram displayed the anterior lip of the cervix in contact with the PDMS standard and on top of the posterior lip of the cervix. A region of the cervix located approximately mid-way between the external and internal os was centered under the apex of the transducer probe. Cini-loop video files were collected for a minimum of 40 seconds per imaging session. A quality scale bar indicated if the tissue compression was in an acceptable range and if any unwanted lateral movements were detected by displaying green for good, yellow for fair, and red for unacceptable. Preliminary images indicated that the strain ratio between two consecutive sites within a standard and phantom remained unchanged if this quality bar was in the yellow or green range. If the quality bar dropped to red, the data from those frames were eliminated from the analysis.

GE software on the ultrasound system was used to select circular regions of interest (ROI) to analyze in the standard and phantom/tissue located directly under the apex of the probe. [64] The location of each circle was defined as the distance from the surface of the phantom/tissue to the center of the circle. The UE software displayed a graph of the mean measured strain for each selected circle as a function of time. The strain data was extracted from these graphs using custom Matlab code (Matlab R2013b, The MathWorks Inc., Natick, MA). Strain ratios at each time point were then calculated and analyzed using OriginPro (OriginLab, Northampton, MA).

Images of the three gelatin phantoms were collected with no standards and then one standard (20:1, 30:1, 40:1, or 50:1 PDMS) layered on top of the transducer probe. In the phantom, eight 5 mm diameter ROIs were sequentially analyzed from top to bottom using the ultrasound analysis software to capture the strain profile through the depth of the phantom (Figure 4.1). When the phantom was imaged without standards, the strain ratio was defined as the ratio between the strain in the first ROI and the strain in each respective ROI in the phantom. When the phantom was imaged with a standard attached to the transducer probe, the strain ratio was defined as the ratio between the strain in the PDMS standard and each ROI in the phantom.

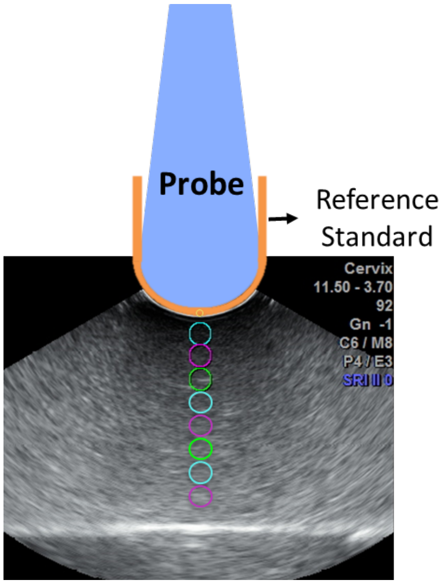

Figure 4.1. Gelatin phantoms were imaged with a transvaginal transducer probe and an attached PDMS reference standard. GE software was used to select circular regions of interest (ROI) on the ultrasound images to display the mean strain within each ROI. ROIs were placed in the standard and throughout the depth of the phantom.

The non-pregnant cervix was imaged with a 40:1 PDMS standard and then separately with a 50:1 PDMS standard attached to the transducer probe. The early gestation cervix was imaged with the 40:1

PDMS standard and the mid-gestation cervix was imaged with the 50:1 PDMS standard attached to the transducer probe. The strain ratio for all cervical elastograms was defined as the ratio of strain between the PDMS standard and each ROI placed throughout the thickness of the cervix located directly under the apex of the transducer probe.

Representative DICOM images of the phantoms and tissues under compression during imaging as well as without any applied load were exported from each imaging session. ImageJ (US National Institutes of Health, Bethesda, MD) was used to measure the thickness of the gelatin phantom or cervix in each image. The contact depth (distance that the indenter tip is compressed into the phantom) was determined as the difference between the unloaded thickness and compressed thickness. Images of the two pregnant cervixes without any applied load were not collected, so the unloaded thickness of the non-pregnant cervix was assumed to be equal to the unloaded thickness of the pregnant cervixes so that a contact depth could be estimated for these images.

Ultrasound Elastography Modulus Calculation

The elastic modulus (*E*), a normalized measure of stiffness, was calculated using a combination of three-dimensional Hooke's law formulations of stress (a normalized measure of force in each direction) and the Hertzian formulations for stress along the z-axis (stresses experienced in each direction of the phantom located directly under the apex of the indenter tip) of a half-space with an applied Hertzian pressure distribution (pressure due to a spherical tip indenting a flat, infinite surface). Due to geometric symmetry, the stresses (σ) and strains (ε) in the x and y direction can be set equal to each other in both the standard and phantom. This reduces the 3D Hooke's law to equation 4.1.

$$\sigma_z = \frac{E}{(1+\upsilon)(1-2\upsilon)}[(1-\upsilon)\varepsilon_z + 2\upsilon\varepsilon_x] \tag{4.1a}$$

$$\sigma_x = \sigma_y = \frac{E}{(1+\upsilon)(1-2\upsilon)}[\varepsilon_x + \upsilon\varepsilon_z] \tag{4.1b}$$

The subscripts indicate in which direction the stress and strain are in, using a standard Cartesian coordinate system, and the Poisson's ratio (ν) is a material property. The stresses within the phantom directly under the apex of the transducer probe can be expressed using Hertzian formulations (Equation 4.2),

$$\sigma_z = -p_o\left(1+\frac{z^2}{Rd}\right)^{-1} \tag{4.2a}$$

$$\sigma_x = \sigma_y = -p_o\left[(1+\upsilon)\left(1-\frac{z}{\sqrt{Rd}}arctan\frac{\sqrt{Rd}}{z}\right)-\frac{1}{2}\left(1+\frac{z^2}{Rd}\right)^{-1}\right] \tag{4.2b}$$

where p_o is the maximum pressure in the phantom, z is the distance into the phantom, R is the radius of the indenter tip, and d is the contact depth (distance that the indenter tip is compressed into the phantom).

Using equations 4.1 and 4.2, the phantom strain in the z direction is solved for:

$$\varepsilon_{z_p} = \frac{p_o}{E_p}\left(1+\upsilon_p\right)\left[2\upsilon_p\left(1-\frac{z}{\sqrt{Rd}}arctan\frac{\sqrt{Rd}}{z}\right)-\left(1+\frac{z^2}{Rd}\right)^{-1}\right] \tag{4.3}$$

where the subscript p denotes the material properties or strain in the phantom.

If there is no standard attached to the probe then the maximum pressure (p_o) is expressed as:

$$p_o = \frac{2}{\pi}E^*\left(\frac{d}{R}\right)^{1/2} \tag{4.4}$$

where E* is defined as:

$$E^* = \frac{E}{1-\upsilon^2} \tag{4.5}$$

Substituting equations 4.4 and 4.5 into equation 4.3, the UE strain profile along the z-axis within the phantom (ε_{zp}) can be expressed as:

$$\varepsilon_{z_p} = \frac{2}{\pi}\frac{(1+\upsilon_p)}{(1-\upsilon_p{}^2)}\left(\frac{d}{R}\right)^{1/2}\left[2\upsilon_p\left(1-\frac{z}{\sqrt{Rd}}arctan\frac{\sqrt{Rd}}{z}\right)-\left(1+\frac{z^2}{Rd}\right)^{-1}\right] \quad (4.6)$$

When a PDMS standard is attached to the transducer probe, the strain response and material properties of the standard (denoted with a subscript *s*) can be used to calculate the modulus of the phantom (E_p). The stresses within the PDMS standard in the x and y direction (σ_x, σ_y) are assumed to be zero since the standard is not constrained and can freely expand in these directions. This reduces equation 4.1b for the PDMS standard to the expression for Poisson's ratio (Equation 4.7).

$$\varepsilon_{x_s} = -\upsilon_s\varepsilon_{z_s} \quad (4.7)$$

Assuming that the force (P) applied to the surface of the phantom $\left(P = \frac{2}{3}p_o\pi Rd\right)$ is equal to the force applied to the PDMS standard, and that the phantom and PDMS standard have equal contact areas ($A = \pi Rd$), the stress in the z-direction within the PDMS standard (P/A) reduces to $\frac{2}{3}p_o$. Therefore, equation 4.1a for the PDMS standard reduces to Equation 4.8.

$$\sigma_{z_s} = \frac{E}{(1+\upsilon_s)(1-2\upsilon_s)}\left[(1-\upsilon_s)\varepsilon_{z_s} + 2\upsilon_s\varepsilon_{x_s}\right] = \frac{2}{3}p_o \quad (4.8)$$

Substituting equations 4.7 and 4.8 into equation 4.3, the modulus of the phantom as a function of distance into the phantom can be expressed as:

$$E_p = \frac{3}{2}E_s\frac{\varepsilon_{z_s}}{\varepsilon_{z_p}}(1+\upsilon_p)\left[2\upsilon_p\left(1-\frac{z}{\sqrt{Rd}}arctan\frac{\sqrt{Rd}}{z}\right)-\left(1+\frac{z^2}{Rd}\right)^{-1}\right] \quad (4.9)$$

where the ratio of strain between the standard and phantom $\left({}^{\varepsilon_{z_s}}/_{\varepsilon_{z_p}}\right)$ is equal to the strain ratio obtained with UE.

The calculated UE phantom modulus (E_p) was then compared to the measured phantom compressive modulus from unconfined compression by calculating a percent error between the two measurements. This calculated percent error was used to evaluate the accuracy of using the proposed analytical solution.

Finite Element Simulations

A 3D finite element model of UE imaging experiments of tissue phantoms was developed in PreView 1.12[101] using an assumed spherical rigid ultrasound probe with a radius of 1.17 cm and a hexahedral tissue phantom (16 cm x 10.5 cm x 5.5 cm) consisting of 36,000 deformable 8 node linear hexahedral elements in FEBio 1.6.0. [103] When appropriate, PDMS standards were modeled as a sphere encapsulating the ultrasound probe with an inner radius of 1.17cm and a thickness of 0.238 cm, using 3072 8 node linear hexahedral elements. The plastic containers used to hold tissue phantoms were not explicitly modeled. However, to represent the plastic containers used during UE imaging, tissue phantom faces in contact with the plastic container were constrained to have no displacement in the direction perpendicular to the given tissue phantom surface with the exception of the free top surface. For all simulations, the ultrasound probe was displaced into the tissue phantom to contact depths observed during experimental ultrasound imaging. Contact between the ultrasound probe, the tissue phantom, and the PDMS standards was enforced via either a Lagrangian, or an augmented Lagrangian contact formulation. Tissue phantoms and PDMS standards were modeled using a Neo-Hookean material model and experimentally determined moduli from unconfined compression tests. A Poisson's ratio of 0.45 was assumed for all tissue phantoms as well as the PDMS standards. Post processing of finite element data to determine strain and position directly beneath the probe was completed in PostView 1.4.[102]

4.4 RESULTS

Mechanical Characterization

Compressive modulus values obtained with cyclic unconfined compression testing of the PDMS standards and phantoms are shown in Table 4.1. With increased cross-linker the PDMS standard modulus increased and with increased concentration of Knox gelatin the phantom modulus increased. The compressive modulus values of the PDMS standards were used in equation 4.9 to calculate the UE modulus of the gelatin phantoms. The compressive modulus values of the gelatin phantoms were compared to the UE modulus that was calculated using equation 4.9 to assess the accuracy of using UE to measure modulus.

Table 4.1. Unconfined compression moduli of PDMS standards and gelatin phantoms

Material	Modulus (kPa)
20:1 PDMS	700.98
30:1 PDMS	304.58
40:1 PDMS	97.25
50:1 PDMS	45.35
Stiff phantom	55.95
Mid-range phantom	19.38
Compliant phantom	7.28

Ultrasound Elastography without PDMS standards

To verify the presence of a Hertzian strain distribution within the gelatin tissue phantom during UE imaging without an attached PDMS standard, the theoretical Hertzian strain ratio was compared to the finite element and experimental strain ratios. Using equation 4.6 and the contact depths calculated from the DICOM images, the theoretical strain was calculated throughout the depth of each phantom. Similar to the experimental protocol, the strain ratio was then calculated as the ratio between the strain at the top of the phantom and the strain at each ROI within the phantom. This theoretical strain ratio was compared to the experimentally measured UE strain ratios as well as the strain ratios observed in the finite element model for each gelatin phantom

(Figure 4.2). The theoretical strain ratios consistently overestimated both the finite element and experimental strain ratios with increasing divergence at increased distances into the phantoms.

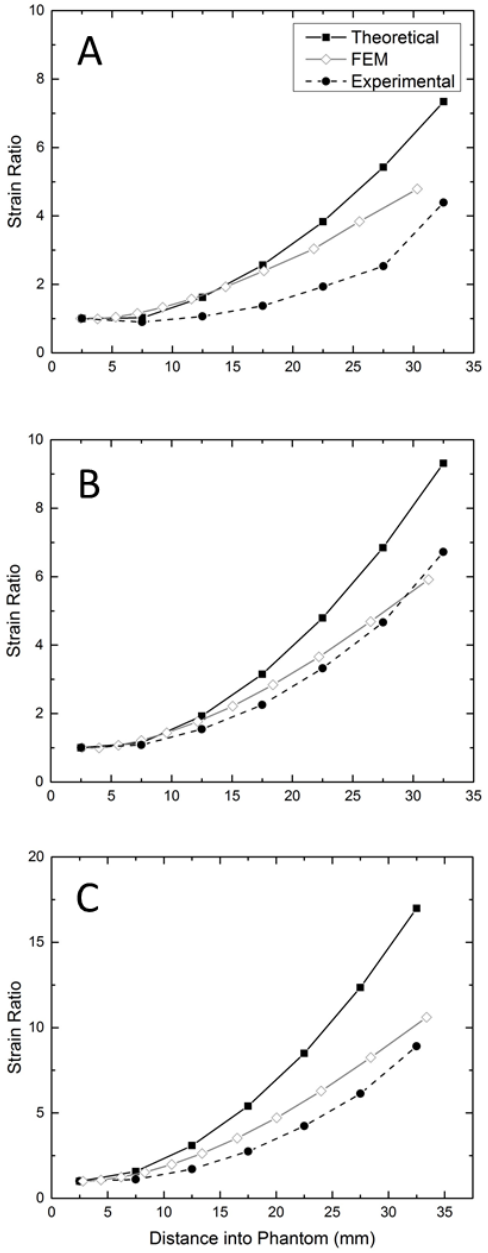

Figure 4.2: Strain ratio comparison between the theoretical, finite element model, and experimental values for the (A) compliant, (B) mid-range, and (C) stiff phantoms being imaged without PDMS standards. The theoretical strain ratios were consistently greater than the finite element model and experimentally measured strain ratios.

Ultrasound Elastography with PDMS standards

To assess the validity of using equation 4.9 to calculate the modulus of a material that is imaged with UE and an attached PDMS standard, the theoretical strain ratio between the standard and phantom needed to calculate a UE modulus that is equal to the compressive phantom modulus obtained with unconfined compression was compared to the finite element and experimental strain ratios. Rearranging equation 4.9 to solve for strain ratio and assuming the modulus of the phantom to be equivalent to the unconfined compression modulus measured in mechanical testing, the theoretical strain ratio between the standard and each ROI within the phantom was determined. The theoretical strain ratios were compared to the strain ratios obtained in the finite element model and with the ultrasound system throughout the depth of each phantom (Figure 4.3). The theoretical and finite element simulation strain ratios had good agreement with a small increase in divergence with increased distances into the phantom. The experimental strain ratios were consistently greater than the theoretical and finite element simulation values if the theoretical standard to phantom strain ratio was less than one. If the theoretical strain ratio between the standard and phantom was greater than one, the experimentally measured strain ratios were consistently less than the theoretical and finite element simulation values. Additionally, the experimental strain ratios were more accurate (compared to the theoretical strain ratios) when the theoretical strain ratio was less than one.

As expected, a similar trend was also seen when equation 4.9 was used to calculate the UE phantom modulus throughout the depth of the phantom for each PDMS standard/gelatin phantom combination (Figure 4.3). Consistent among all combinations of standards and phantoms, the calculated UE phantom modulus decreased with increasing distance into the phantom. When the strain ratios from the finite element simulations were used in equation 4.9, there was a small variation in UE phantom modulus between the different PDMS standard/gelatin phantom combinations. When the experimentally obtained strain ratios from the ultrasound system were used to calculate the UE phantom modulus, the accuracy increased when the strain ratio between the standard and phantom was less than one, which is similar to the trends seen when the theoretical and experimental strain ratios were compared. The most accurate calculation of the UE phantom modulus was for PDMS standard/gelatin phantom combinations that resulted in strain ratios approximately equal to one (Figure 4.4).

Ultrasound Elastography of the Cervix

To demonstrate the feasibility of imaging human tissue, one non-pregnant and two pregnant woman’s cervixes were imaged using UE with an attached PDMS standard. To verify the correct selection of PDMS standards, as detailed in the previous section, the strain ratio between the PDMS standards and cervical tissue was observed throughout the thickness of the tissue (Figure 4.5). The most accurate calculation of UE modulus was obtained when the strain ratio between the PDMS standard and imaged tissue was less than or equal to one. The strain ratio between the non-pregnant cervix and the 40:1 PDMS standard was closer to one than the strain ratio between the non-pregnant cervix and 50:1 PDMS standard. Therefore, the 40:1 PDMS standard was selected to analyze the modulus of the non-pregnant cervix. The strain ratios for the early gestation and mid-gestation cervixes were less than one confirming the appropriate selection of standards.

Using equation 4.9 to calculate the cervical UE modulus, a decrease in modulus was seen with pregnancy that continues to decrease with increased gestation (non-pregnant > early gestation > mid-gestation) (Figure 4.5). However, a distinct discrepancy was seen across all images between the anterior and posterior lip of the cervix. The decrease in modulus in the posterior lip resulted in minimal differences between the pregnant and non-pregnant tissue within the posterior region.

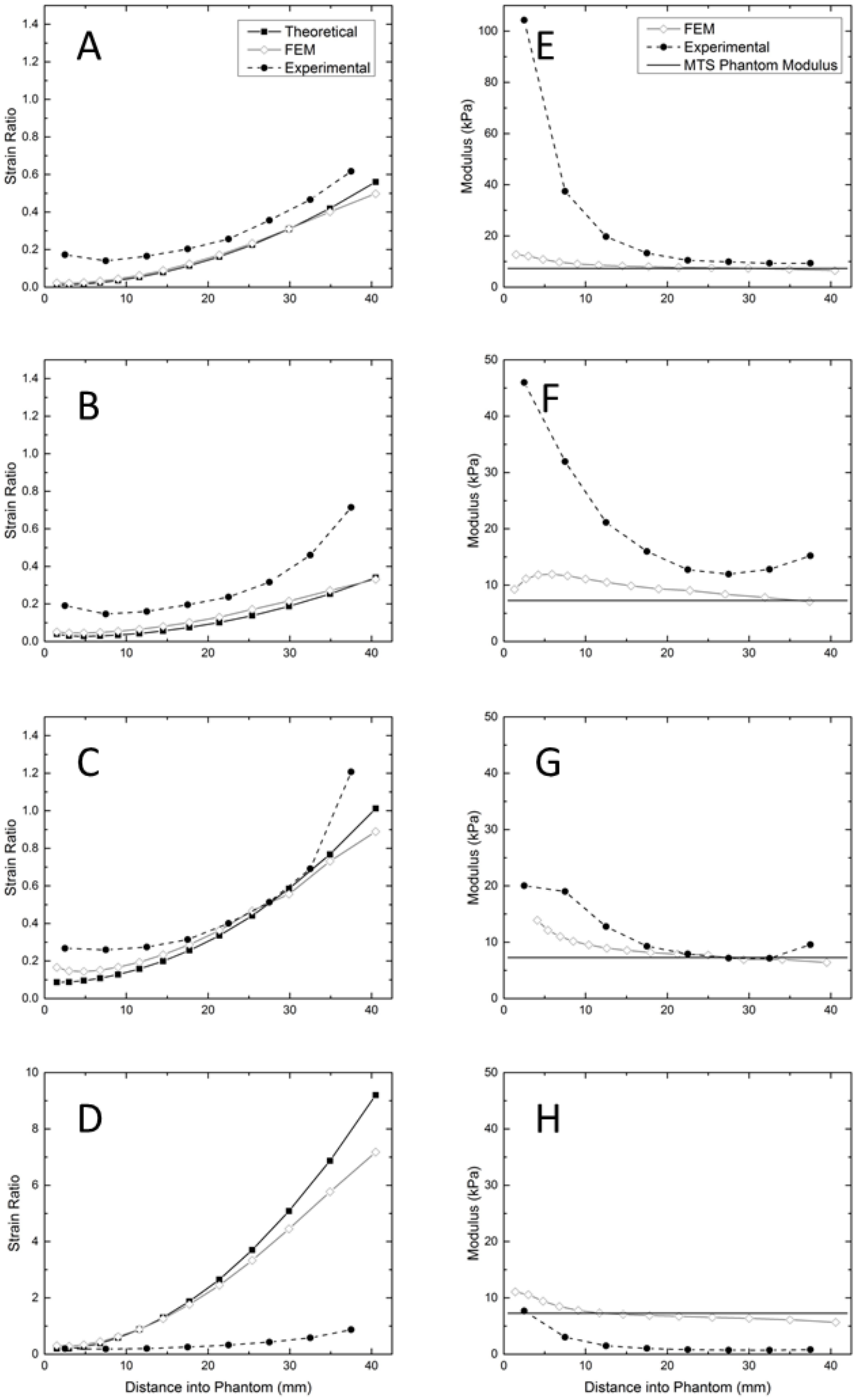
A
B
C
D
E
F
G
H
Theoretical
FEM
Experimental
MTS Phantom Modulus
Strain Ratio
Modulus (kPa)
Distance into Phantom (mm)
0
10
20
30
40
0.0
0.2
0.4
0.6
0.8
1.0
1.2
1.4
2
4
6
8
50
60
80
100

Figure 4.3: Strain ratio (A-D) and UE modulus (E-H) values throughout the depth of the compliant phantom when imaged with the 20:1 (A,E), 30:1 (B,F), 40:1 (C,G), and 50:1 (D,H) PDMS standards. Solid lines on the UE modulus figures represent the compressive modulus of the compliant phantom measured with unconfined compression. The most accurate calculation of UE modulus was obtained when the measured strain ratio approached one. Similar trends were seen in the mid-range and stiff phantoms.

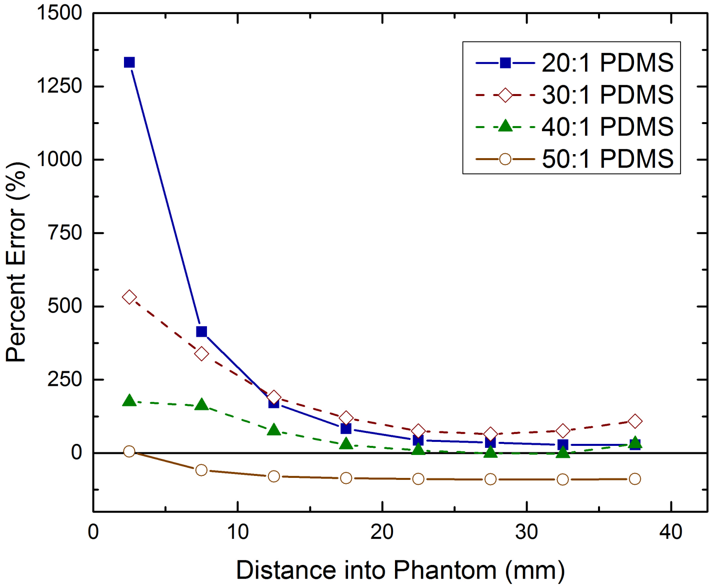

Figure 4.4. Percent error of the UE modulus compared to the unconfined compression modulus throughout the depth of the compliant phantom when imaged with each PDMS standard. The range of error observed between the different PDMS standard/phantom combinations as well as the magnitude of error was considerably reduced compared to when the UE modulus was calculated using a one-dimensional, linear Hooke's law. Similar trends were seen in the mid-range and stiff phantoms.

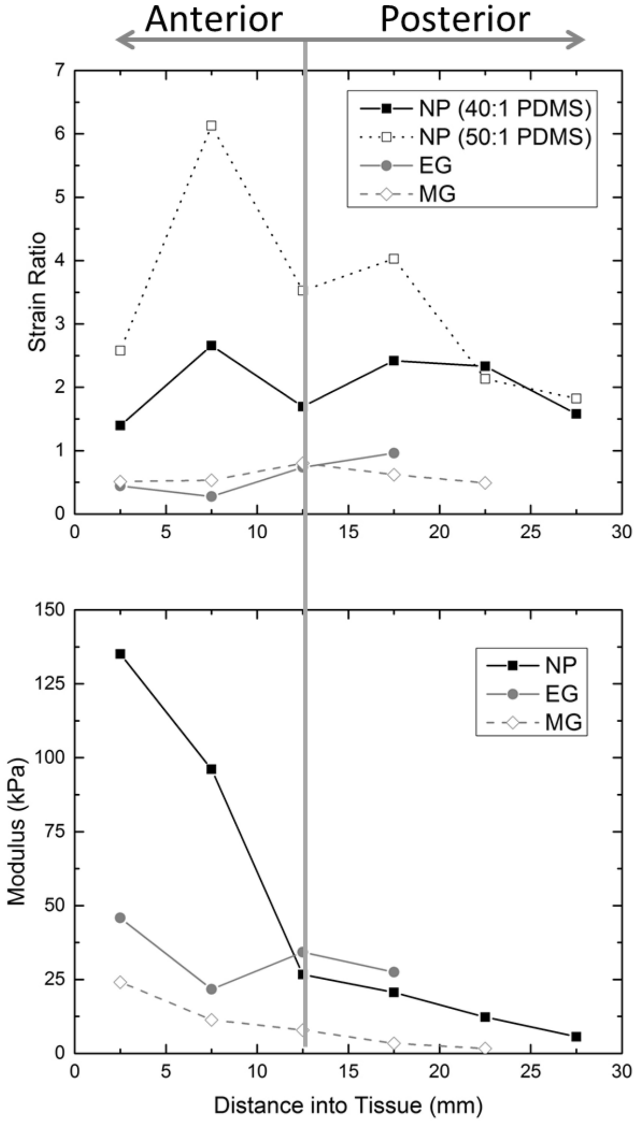

Figure 4.5. Measured strain ratios (top) and calculated UE modulus (bottom) values throughout the thickness of each cervix. UE modulus was shown to be more accurate when the strain ratio between the standard and imaged tissue was approximately equal to one. Therefore, the 40:1 PDMS standard was chosen over the 50:1 PDMS standard to calculate the modulus of the non-pregnant cervix. A decrease in modulus is seen with pregnancy that continues to decrease with increased gestation. Additionally, a clear discrepancy was seen across all images between the anterior and posterior lip of the cervix. This drop in modulus within the posterior lip indicates that the developed analytical solution is not valid across tissue discontinuities and the modulus in the posterior lip cannot be considered accurate. (NP: non-pregnant; EG: early gestation; MG: mid-gestation)

4.5 DISCUSSION

The aim of this study was to develop an analytical solution that would correct for the strain dissipation caused by a spherical tip (transvaginal ultrasound tranducer probe) indenting a half-space (tissue phantom) so that the modulus of a homogenous phantom could be determined at any distance into the phantom using ultrasound elastography (UE). An analytical solution was derived by combining the three-dimensional Hooke's law equations for stress with the three-dimensional Hertzian formulations of stress within the indented half space located directly under the apex of the indenter tip. The analytical solution was used to calculate theoretical strain ratios throughout the phantom when imaged with and without an attached PDMS standard. Experimentally measured UE strain ratios between an attached PDMS standard and the gelatin phantom were then input into the analytical solution to calculate the UE modulus of the phantom. Theoretical and experimental strain ratios and moduli were also compared to finite element simulations of the phantom indentation to further validate and understand the advantages and limitations of this analytical solution. Finally, the proposed analytical solution was used to analyze images of non-pregnant, early gestation, and mid-gestation cervixes to demonstrate the ability of this technique to assess cervical stiffness throughout gestation.

The classic Hertzian solution describes the stress and strain distribution within an infinitely large, flat, homogenous, elastic material (half-space) being indented by a spherical probe that is much stiffer than the half space (Equation 4.2). In our study this was most similar to the gelatin phantoms that were imaged without any PDMS standards attached to the probe. The divergence between the theoretical strain ratios within the phantom and those seen in the finite element model suggests the differences in the experimental set-up and the assumptions between the Hertzian solution and the FEM. The Hertzian solution assumes that the material being indented is infinitely large, however, the gelatin phantom was finite in size. The FEM considered more realistic boundary conditions of the gelatin phantoms by using the actual dimensions of the tissue phantom that was imaged with UE. The difference in boundary conditions could be influencing the difference in strain dissipation between the theoretical solution and FEM predictions. The further divergence of experimental values from the FEM solutions was most likely due to experimental measurement error. The depth at which the indenter tip was pushed into the phantom (contact depth) influenced the magnitude of strain observed in the phantom as well as how quickly the strain was dissipated through the phantom. Error in the measurement of contact depth as well as boundary condition approximations most likely accounts for most of the differences seen between the FEM and experimental values. Despite these limitations and sources of error, the theoretical solution, FEM, and experimental values all followed the same trend, but with different magnitudes. This suggests that it is valid to use a Hertzian model to describe the strain dissipation in a phantom during UE imaging.

Introducing a PDMS standard onto the ultrasound transducer probe enabled the calculation of the gelatin phantom UE modulus by measuring the strain ratio between the PDMS standard and gelatin phantom (Equation 4.9). To better understand the accuracy of calculating the phantom UE modulus with the proposed analytical solution, the strain ratios from the FEM and experimental data were compared to the theoretical strain ratio between the PDMS standard and gelatin phantom. The theoretical solution assumed that the modulus of the gelatin phantom was constant throughout its thickness and equal to the modulus measured with unconfined compression. Therefore, the theoretical strain ratios were calculated to solve for the strain ratio as a function of distance into the phantom and assuming the phantom modulus to be equal to the values measured with unconfined compression. The theoretical strain ratios showed good agreement with the FEM indicating the accuracy of using this solution to describe the strain dissipation within a phantom being imaged with UE and a PDMS reference standard. A small divergence between the theoretical and FEM strain ratios was seen near the bottom of the phantom most likely due to the difference in assumed boundary conditions between the two models. As discussed above, the realistic dimensions of the gelatin phantoms cannot be considered as infinitely large as the theoretical solution assumes, which leads to a difference in boundary conditions and thus a divergence in strain ratio results. Increased divergence between the experimental strain ratios and the theoretical/FEM strain ratios were observed when the theoretical/FEM strain ratios were greater than one. This indicates that the experimental strain ratios are most accurate when the PDMS standards strain less than the gelatin phantoms.

The final measure to assess the accuracy of the developed analytical solution was to calculate the phantom UE modulus using the strain ratio data obtained from the FEM as well as the strain ratio data from the experimental UE data and compare both moduli to the unconfined compression modulus for all PDMS standard/gelatin phantom combinations. Similar to the differences seen between the theoretical and FEM strain ratios, the difference between the FEM calculated UE modulus and the unconfined compression modulus was most likely due to differences in assumed boundary conditions. This was also apparent when comparing the different PDMS standard/gelatin phantom combinations. The magnitude of error was approximately equal across all PDMS standard/gelatin phantom combinations because the basic assumptions of the model did not change with modulus or strain differences. This magnitude of error is thus the minimum error that can be expected when using the proposed analytical solution to calculate the gelatin tissue phantom stiffness from UE strain data.

When using the experimental strain ratios to calculate the phantom UE modulus, a trend emerged that was dependent upon the measured strain ratio between the PDMS standard and gelatin phantom. If the measured UE strain ratio exceeded a magnitude of one, meaning that the PDMS standard strained more than the gelatin phantom, then the UE modulus was the least accurate compared to the other standard/phantom combinations. This could be due to the change in shape that the PDMS standard undergoes at large deformations. The Hertzian assumptions used in the derivation of the proposed analytical solution state that the indenter (i.e. the transducer probe with an attached PDMS standard) is spherical and does not change in radius during compression. When the experimental conditions violate these assumptions, the experimental results deviate from the theoretical solution.

On the other hand, if the measured strain ratio between the PDMS standard and gelatin phantom was less than a magnitude of one, meaning that the PDMS standard strained less than the gelatin phantom, then the calculated UE modulus was more accurate. The most accurate phantom UE modulus was calculated when the gelatin phantom and PDMS standard strained approximately equal amounts resulting in a UE strain ratio equal to one. This could be due to the optimization of conflicting sources of error. The stiffer the PDMS standard is, the less it will deform during UE imaging and loading. This agrees with the assumptions of the Hertzian equations and reduces error associated with the theoretical solution. However, the PDMS standard must be compliant enough to experience compression that is measureable by the ultrasound system during imaging. Increasing the compliance of the PDMS standard reduces measurement error associated with the ultrasound system. Therefore, choosing a PDMS standard that results in a strain ratio equal to one ensures that the standard is not compressed too much or too little during imaging.

Choosing the correct PDMS standard for imaging is thus a straightforward process that is immediately assessed during imaging when the proposed analytical solution is used to calculate UE modulus. A previous study in our lab (Chapter 3) reported a large range in calculated UE modulus that was strongly dependent on the selection of the attached PDMS standard. Additionally, the process of selecting the correct standard was subjective, requiring the ultrasound technician's judgment. The current proposed analytical solution not only presents an objective method for selecting the correct standard, but the range of calculated UE modulus is also dramatically reduced between the different PDMS standards. Therefore, the error associated with PDMS standard selection is drastically reduced from prior studies.

The magnitude of error associated with using the current proposed analytical solution is reduced by several orders of magnitude as compared to previous studies using a one-dimensional linear Hooke's law formulation to calculate UE modulus. Although the current solution does not calculate the exact modulus that was measured in unconfined compression, this solution is a significant improvement on current published methods. Additionally, the calculated UE modulus in this study did not vary as widely with increased distance into the phantom as compared to previous studies. Therefore, we can conclude that the current proposed analytical solution does correct for a large portion of the strain dissipation and is an improvement upon previously published methods.

When applying this method to the human cervix, cervical UE modulus was shown to decrease with gestation and with increased gestational age. These trends agree with clinical observations throughout gestation and with previously published literature.[16,31] The magnitude of non-pregnant cervical UE modulus in the anterior lip agreed well with previously published values of non-pregnant *ex vivo* cervical tissue tested in confined compression.[119] Additionally, the magnitude of mid-gestation cervical UE modulus in the anterior lip was comparable to previously published elastography values of the mid-gestation cervix report by Hee et al.[64] Hee et al. used a one-dimensional, linear Hooke's law relationship to calculate cervical UE moduli that were of the same order of magnitude as the current study; however, their cervical UE modulus values were greater than those reported in the current study. We know from our tissue phantom analysis in the current study compared to that of our previous study using a linear Hooke's law analysis that modulus values obtained from a linear Hooke's law relationship will generally overestimate the actual compressive modulus. Therefore, it is expected that the cervical modulus values reported in the current study would be less than those reported using a one-dimensional Hooke's law analysis. Overestimating cervical stiffness *in vivo* could result in a false negative diagnosis of cervical insufficiency, which could ultimately result in preterm labor or early termination of pregnancy. Thus, it is imperative that UE modulus be calculated with an analytical solution that considers the effects of the transducer probe geometry such as the one proposed in this study.

Consistent among all images, there was a discrepancy seen between the anterior and posterior lip of the cervix. The posterior lip of the cervix was consistently more compliant than the anterior lip even though there is no clinical indication that would cause a different stiffness between the anterior and posterior lip. This discrepancy is due to the discontinuity of the cervix. Our analytical solution assumes a continuous medium for the half-space, whereas the cervix is an annulus with the cervical canal between the anterior and posterior lip. Our model does not accurately account for this geometry, thus the values obtained in the posterior lip using the current analytical solution are not valid.

To our knowledge, this study presents the first attempt at correcting for the strain dissipation observed in UE of the cervix resulting from the compressive load distribution caused by the spherical tip of a transvaginal transducer probe. Although the presented analytical solution includes a number of assumptions and limitations, it significantly reduces the error observed with a one-dimensional, linear Hooke's law analysis commonly used in the literature. Additionally, the current study proposed an objective method for PDMS standard material selection. Using the proposed solution to analyze cervical elastograms, modulus values were obtained of the anterior lip that agreed well with previously published values. Future studies are needed to characterize the strain distribution in a heterogenous and discontinuous material such as the cervix to accurately calculate cervical stiffness at the posterior lip. In conclusion, the results from this study indicate that UE with an attached reference standard holds promise for evaluating cervical stiffness throughout gestation and could improve early detection and diagnosis of cervical insufficiency.

CHAPTER 5

MICROSTRUCTURAL AND COMPOSITIONAL CONTRIBUTIONS TO PLACENTAL MEMBRANE MECHANICS AND TIMING OF RUPTURE

5.1 DESCRIPTION OF STUDIES IN THIS CHAPTER

The aim of this study is to explore ECM and tissue property differences between spontaneously and artificially ruptured membranes to elucidate what causes a difference in membrane rupture timing at term. Previously published literature concluded that the primary structural determinant of the chorioamnion (CA) membrane is the amnion. CA membrane literature as a whole then focused on characterizing the amnion and concluded that the intact membrane behavior *in vivo* was largely determined by the material properties of the amnion alone. Therefore, this study was aimed at characterizing the amnion, hypothesizing that tissue property differences in the amnion between two clinical groups would be responsible for differences in rupture timing. Specifically, artificially ruptured (AROM) amnion would have an increased modulus or toughness compared to spontaneously ruptured (SROM) amnion. Preliminary data were confounding suggesting that the amnion alone did not dictate the timing of rupture. Instead, the chorion may play a much larger role than originally anticipated. The focus of the study was then shifted to include testing of the separated amnion and chorion as well as intact CA. Using the rule of mixtures the contribution of the chorion during membrane rupture was investigated. Preliminary rule of mixtures analyses showed that samples taken near the rupture site could be described with a rule of mixtures approach but samples near the placenta could not. These results suggested that a third mechanism was also contributing to membrane behavior. Thus we hypothesized that the interface between the amnion and chorion was also contributing to membrane behavior and further testing was prompted to characterize the strength of the interface.

Due to these exciting but unexpected results and additional testing protocols, the work described in this chapter is ongoing and will be divided into two manuscripts when completed. The first manuscript will include data collected from vaginally delivered membranes that ruptured either spontaneously or artificially. The bulk of the manuscript will focus on the confounding amnion data and will present preliminary chorion and intact CA data, suggesting that the chorion contributes to the timing of rupture *in vivo*. The second manuscript will use C-section membranes to present a more controlled and comprehensive study of the composite CA membrane properties using a rule of mixtures analysis that includes a component for interfacial strength. Of the dataset that will be included in the second manuscript, only preliminary delamination mechanical testing results are presented here.

5.2 ABSTRACT

Chorioamnion, the sac that surrounds the fetus *in utero*, is comprised of two layers: the inner fibrous amnion and the outer, thick cellular chorion. Scanning electron microscopy has shown a multitude of fine, discrete fibers connecting these two layers. The interplay of these two layers and the interface between the amnion and chorion determine the intact membrane behavior *in vivo*, while their mechanical properties dictate the mode and timing of rupture. Broadly, we seek to elucidate how the underlying microstructure and composition of term chorioamnion contributes to its function and rupture timing *in vivo*. By considering the chorioamnion as a simplified composite bilayer, we applied simple composites theory to better understand the individual contributions of the amnion and chorion. Uniaxial tensile testing was performed on identically sized strips of chorion, amnion, and chorioamnion, from regions proximal ("Placental") and distal ("Rupture") to the placenta, to determine elastic modulus of spontaneously (SROM) and artificially (AROM) ruptured membranes. Amnion modulus did not change significantly between groups (AROM vs SROM; Placental vs Rupture), but rupture region chorion from AROM membranes was greater than other chorion groups tested. This suggests the importance of the chorion in determining the CA composite modulus and timing of rupture. The rule of mixtures, taking into account dimensions and properties of the individual layers, consistently overestimated the CA composite modulus except in rupture region AROM membranes. This suggests that some other mechanisms may be contributing to the intact membrane strength of these membranes. Biochemical and histological analyses provided further insight into these findings with increased GAG concentration in rupture region AROM chorion. Increased GAGs in combination with increased modulus may indicate that decorin is elevated

and forming increased collagen cross-links. Additionally, lap shear testing (based on ASTM D3163-01) of adherent layers of chorion and amnion validated previous observations of fine fibers connecting the two layers. We observed a decrease in shear modulus of the interface between the layers in regions proximal to sites of rupture as compared to the more robust properties in regions proximal to the placenta. The combined results of ECM and tissue property differences in term, healthy membranes that exhibit differing modes of rupture may elucidate the mechanical mechanisms responsible for preterm premature rupture of CA membranes.

5.3 INTRODUCTION

The chorioamnion (CA), or placental membrane, is the sac that surrounds the fetus *in utero*. It is comprised of two layers: the inner fibrous amnion, mainly composed of collagen, and the thick cellular chorion. [24] The CA membrane serves a dual structural function throughout gestation. Prior to term it must remain intact to prevent leaking of amniotic fluid and to provide a physical barrier between the fetus and environmental conditions that may cause infection. At term, the membrane is designed to rupture to allow delivery of the fetus. The timing of rupture, however, is critical to the outcome of the pregnancy. Preterm premature rupture of the membrane (PPROM), rupture prior to 37 weeks gestation, is one of the leading causes of preterm birth (PTB) accounting for 25-30% of PTB in the US. [7] PTB can lead to serious infant morbidity and mortality. The most common complication is respiratory distress syndrome, insufficient surfactant production in the lungs, which is the leading cause of death in preterm infants. [112] Despite these adverse outcomes, the etiology of PTB, in particular PPROM, is poorly understood.

There are several modes of failure of the CA. The most commonly observed mode of failure is spontaneous rupture of the membrane (SROM), characterized by CA rupture at term after labor has begun. In some cases intervention by a physician must be taken to artificially rupture the membrane (AROM) after labor has persisted to allow delivery of the fetus. Why some membranes fail spontaneously at term and some do not is underexplored in the literature, but could elucidate the mechanisms that lead to preterm rupture.

It has been predicted that the strength of the membrane is one of the primary contributors to the timing of membrane rupture *in vivo* and that the extracellular matrix (ECM) components and structural organization dictate the strength.[33,131] Previous studies have shown that the amnion is much stronger and stiffer than the chorion so it has been thought to be the primary structural determinant in the CA. [134,136] Therefore, several studies have characterized possible individual contributors to membrane rupture such as amnion material properties, structure, or composition. [29,85,131] Additional studies have demonstrated decreased strength along the membrane tear line compared to samples taken near the placenta. [11,12,48] Membranes taken from non-labored Caesarean sections also exhibit this weak zone over the cervix, characterized by decreased strength, work to rupture, stiffness, and ductility (displacement at rupture), suggesting that this process is largely biochemically regulated, altering tissue properties near term, instead of solely structural reorganization during labor. [49,117]

Also of interest is the sequence of rupture within the CA. Total membrane failure has been shown to consist of intact membrane distention, separation of the amnion and choriodecidua, rupture of the choriodecidua, non-elastic further distention of the amnion, and ultimately amnion rupture. [10,117] The consistent observation of membrane delamination raised interest in studying the role of the interface in contributing to the strength of the intact CA membrane *in vivo*. Further work showed that the sum of the work to rupture of the individual amnion and chorion was only 54% of the work to rupture the intact chorioamnion. This difference in work to rupture is hypothesized to be, at least in part, due to the work required to separate the amnion from the chorion. Additionally, another study quantified the adhesive force of the interface using T-peel tests. [84] It was shown that the adhesive force decreased as the distance from the placental disc increased. These results collectively suggest that the separation of the amnion and chorion plays an important role in membrane failure[10]; however, the physiologically relevant shear strength of the interface has not been investigated.

In this study we aim to quantify ECM and tissue property differences between spontaneously and artificially ruptured membranes to elucidate how membrane microstructure contributes to the mechanical strength of the membrane and tissue failure *in vivo*. Membrane mechanical properties and ECM composition and structural organization will be investigated from three perspectives: (1) amnion only; (2) CA bilayer/composite structure; and (3) interface between and amnion and chorion. We hypothesize that the ECM and tissue property differences in term, healthy membranes that exhibit differing modes of rupture can elucidate the mechanisms responsible for preterm premature rupture of CA membranes.

5.4 MATERIALS AND METHODS

Specimen Collection and Preparation

Thirty full-term (n = 21 vaginally delivered; n = 9 cesarean section) human placental membranes were collected from consented patients at the University of Colorado Hospital (COMIRB #06-1159) and the Boulder Community Hospital (CU Boulder IRB1007.16). Patients with complications that are typically associated with PPROM, such as diabetes and smoking during pregnancy, were excluded. Immediately following delivery, membranes were washed in phosphate-buffered saline (PBS) (pH 7.4). Sections of intact chorioamnion (20 mm x 40 mm) were dissected adjacent to the rupture site ("Rupture") and near the placenta ("Placental") for histological analysis, rolled using forceps, chorion innermost, and stored in 10% neutral buffered formalin for 24-36 hours. The ends of each roll were tied using fine string, approximately 5 mm from each side, to keep the roll intact. Eight amnion and four chorion biopsy punches (8 mm diameter) were obtained adjacent to the placental disc and identified rupture site and frozen at -80°C for biochemical analysis. The remaining membrane was laid flat and frozen at -80°C until preparation for testing.[3,37] Vaginally delivered membranes (n = 9 AROM and 12 SROM) were included in the amnion only and composite bilayer analyses while the cesarean section membranes were designated for interfacial delamination analysis.

Amnion and Chorioamnion Mechanical Behavior Sample Preparation

Thawed (20°C, 10 min), intact CA strips (5.5 x 25 mm) from vaginally delivered membranes were dissected near the placental disc ("Placental") and adjacent to the rupture site ("Rupture") (n = 4 strips/region) for mechanical testing. Sections of chorion were gently removed from the amnion near the placental disc and rupture site. Strips of amnion and chorion (5.5 x 25 mm) were then dissected in each region of separated chorioamnion (n = 6 amnion and 4 chorion strips/region) for mechanical testing. Mechanical testing specimens were equilibrated overnight in PBS at 4°C.

CA Interfacial Behavior Sample Preparation

Strips of thawed (20°C, 10 min), intact CA membrane (10 x 80 mm) from C-section membranes were dissected adjacent to the placental disc ("Placental"), the identified rupture site ("Rupture"), and a mid-region ("Middle") between the placental and rupture sites (n = 2 strips/region). A water-based dye, gentian violet (HUMCO, Texarkana, TX), was applied to outline a central 10 mm region that would remain intact. Using gentle traction, the amnion and chorion were separated on both sides of each specimen up to the designated intact region. The separated chorion was cut on one side of the specimen and the separated amnion was cut on the opposing side of the specimen. Specimens were equilibrated overnight in PBS at 4°C. Immediately before testing, a thin polyester backing was carefully adhered with cyanoacrylate adhesive (Loctite, Henkel Consumer Adhesives Inc., Avon, OH) to all exposed sides of the chorion and amnion to facilitate gripping and to isolate deformation to the chorioamnion interface (Fig. 5.1). Interface dimensions (length x width) were measured prior to testing with digital calipers.

Mechanical Testing

Investigation of Amnion and Chorioamnion Mechanical Behavior and Properties

An MTS Insight 2 (MTS Systems Corp, Eden Prairie, MN; 5 N load cell) equipped with an environmental chamber was used to perform uniaxial tensile testing. Specimens were held between two smooth metal grips (11 mm gauge length, PBS, pH = 7.4, 37°C) and sand paper to prevent slipping during testing. Specimen width was measured prior to testing with digital calipers and thickness was measured using histology specimens. Three different testing methods were used to study the mechanical response of amnion: cyclic, incremental cyclic, and incremental stress relaxation. The chorion and intact CA samples were only analyzed with the cyclic and incremental cyclic methods. A preload of 0.01 N was imposed on each sample to ensure consistent initial stress states.

Cyclic tests (n = 2 amnion, 2 chorion, and 2 intact CA specimens/region) displaced amnion samples to 3.5 mm, chorion samples to 4.75 mm, and intact CA samples to 5.5 mm and unloaded to 0 mm extension at a constant crosshead displacement rate of 15 mm/min. This load-unload cycle was repeated for a total of ten cycles. Incremental cyclic tests (n = 2 amnion, 2 chorion, and 2 intact CA specimens/region) initially displaced samples to 1 mm and unloaded to 0 mm extension at a constant crosshead displacement rate of 15 mm/min. This load-unload cycle was repeated for a total of 3 cycles. The load-unload cycle maximum displacement was increased in increments of 1 mm with 3 cycles per increment until failure. Incremental stress relaxation tests (n = 2 amnion specimens/region) initially displaced samples to 10% strain followed by a 200 second hold segment to observe the relaxation response of the tissue. Samples were then displaced in increments of 5% strain and followed by a 200 second hold segment. This process was repeated to failure. Displacement increments occurred in less than 1 second (1.5 mm/s) to assume instantaneous displacement.

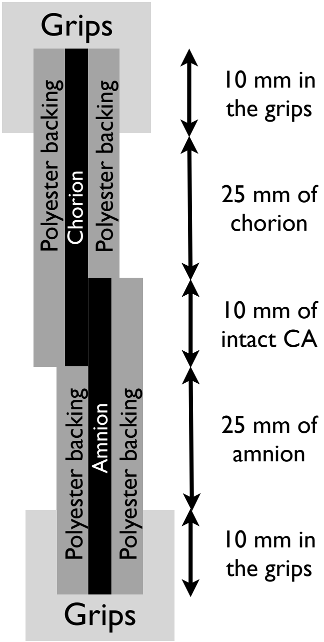

Figure 5.1. Specimen configuration during lap shear delamination testing. Polyester backing was adhered to all exposed sides of the sample to isolate mechanical response to the chorioamnion interface.

Investigation of the CA Interfacial Behavior and Properties

An MTS Insight 2 (MTS Systems Corp, Eden Prairie, MN; 5 N load cell) equipped with an environmental chamber (PBS, pH

= 7.4, 37°C) was used to perform lap shear delamination testing. All specimens were held between two custom smooth metal grips and maintained 25 mm between the intact region and the interface of the grips (Fig. 5.1). Samples were displaced at a constant crosshead displacement rate of 0.5 mm/s. Specimen dimensions and testing methods were adapted from ASTM Standard D3163-01.

Biochemical Analysis

Specimens were lyophilized and weighed prior to all biochemical assays (1 amnion specimen = 2 tissue biopsy punches; 1 chorion specimen = 1 tissue biopsy punch). Total collagen content was measured using the Woessner method[172] against hydroxyproline standards. The measured hydroxyproline content was converted into collagen content using a mass ratio of collagen to hydroxyproline of 7.64:1. Sulfated GAG content was measured using a standard dimethylmethylene blue (DMMB) assay with chondroitin-6-sulfate as the standard.[44]

Histology

Samples were fixed in 10% neutral buffered formalin for 24-36 hours, ethanol dehydrated, and paraffin embedded. 10 μm sections were stained with Masson's Trichrome for structure and thickness observations. Images were examined for qualitative differences between placental and rupture regions from AROM and SROM membranes.

Data Analysis

Investigation of Amnion and Chorioamnion Mechanical Behavior and Properties

Mechanical testing data are reported as mean ± standard error of the mean (SEM). The 10th loading cycle of each cyclic test method dataset was used to calculate the elastic modulus, *E,* which was defined as the slope of the final 18% of the σ-ε curve. Incremental cyclic datasets were analyzed for failure stress, failure strain, and toughness (using a trapezoidal rule in Matlab R2013b, The MathWorks Inc., Natick, MA) using the final loading curve that led to failure of the specimen. Finally, incremental stress relaxation datasets were used to calculate an instantaneous modulus, E_o, and equilibrium modulus, E_∞. E_o was defined as the linear region slope of the peak stress, σ_o, vs respective strain curve, where σ_o was defined as the maximum stress of each increment. E_∞ was defined as the linear region slope of the equilibrium stress, σ_∞, vs respective strain curve, where σ_∞ was defined as the last stress value recorded for each increment.

Composite Modeling of the CA Bilayer to Predict Properties

The rule of mixtures was used to investigate the individual contributions of the amnion and chorion for intact CA membrane behavior.[33] With the assumption that the length and width were constant for each specimen, the rule of mixtures was simplified to utilize thickness ratios, rather than volume ratios of the components:

$$E_{CA} = \frac{E_C t_C + E_A t_A}{t_C + t_A} \tag{5.1}$$

where the elastic moduli (*E*) were taken from cyclic mechanical tests and thicknesses (*t*) were measured using histology images. This rule of mixtures incorporates assumptions that the materials are elastic, isotropic, and homogenous.

Investigation of the CA Interfacial Behavior and Properties

The slope of the linear pre-failure region of the σ-ε loading response was defined as the interfacial modulus, E_i (Figure 5.2). The delamination stress, σ_D, was determined as the maximum stress that the interface withstood prior to failure.

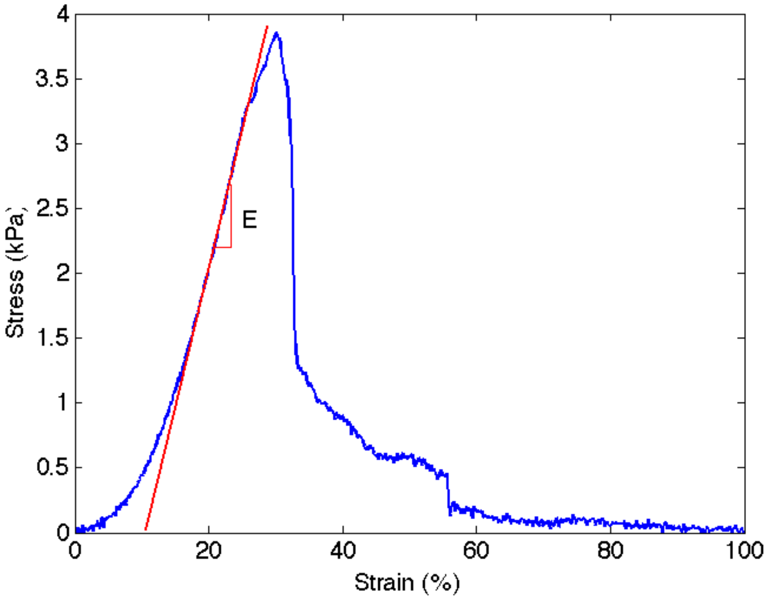

Figure 5.2. Interfacial modulus was determined as the slope of the linear region of the σ-ε curve prior to failure.

Statistical Analysis

Two-factor ANOVAs were performed to detect significant differences between AROM and SROM membranes between placental and rupture regions (amnion and chorioamnion behavior analysis). One-way ANOVAs were performed to detect significant differences between placental, middle, and rupture region interfacial modulus and delamination stress (interfacial behavior analysis). Tukey's tests were performed as an ANOVA post-hoc to determine which groups were significantly different (JMP, Version 11.1. SAS Institute Inc., Cary, NC). Due to the complexity of factors that could affect the mechanics of CA during a vaginal delivery and the variance of how they may have been handled post-delivery a p-value of 0.1 was considered to be significant.

5.5 RESULTS

Mechanical Testing

Investigation of Amnion and Chorioamnion Mechanical Behavior and Properties

Cyclic testing was performed on amnion, chorion, and intact chorioamnion to assess the modulus of each tissue after preconditioning. The stress-strain response of amnion, chorion, and intact CA was non-linear and viscoelastic (Figure 5.3). A secondary linear region was observed at higher strains indicating collagen engagement. The collagen engagement region (final 18% of the stress-strain curve) was used to determine the elastic modulus of the 10th loading cycle. No statistical differences were observed in the amnion. Due to the small samples sizes and high variance there was also no statistical significance in the chorion; however, further inspection of chorion data showed that chorion dissected from the rupture region of AROM membranes was 92% stiffer than chorion taken from the rupture region of SROM membranes, which suggests that these two groups may become significant with increased sample sizes. Also of interest was that the general trend of decreasing modulus from placental to rupture regions was reversed in chorion harvested from AROM membranes. Instead of the modulus decreasing in the rupture region of AROM membranes, the modulus increased. This behavior was further reflected in the intact CA data, which also had an increase in modulus for rupture region CA from AROM membranes. Even with small samples sizes, statistical analysis revealed a significant increase in modulus from intact CA harvested from AROM membranes versus SROM membranes ($p = 0.04$) (Figure 5.4).

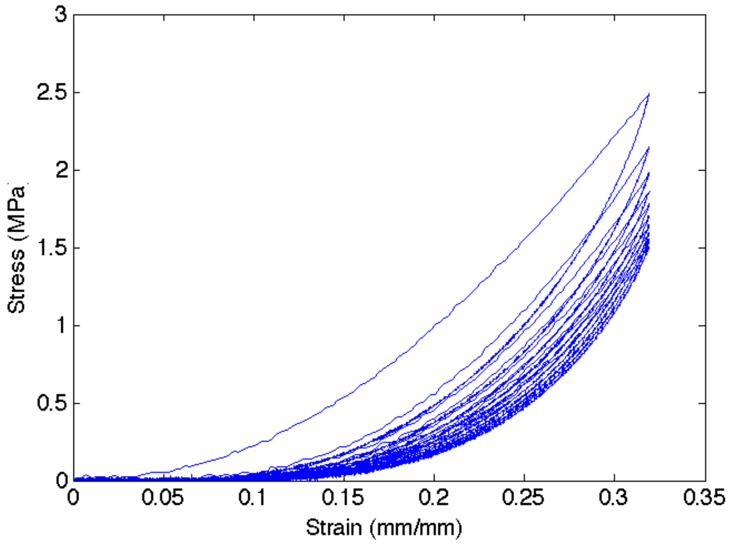

Figure 5.3. Representative stress-strain curve of amnion during a uniaxial cyclic tensile test. Chorion and intact CA specimens also exhibited a similar response.

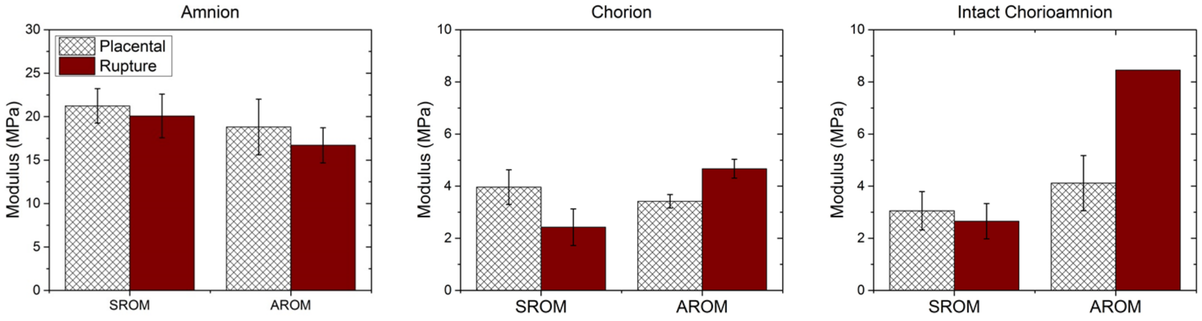

Figure 5.4. Elastic modulus of amnion (n = 12 SROM and 9 AROM), chorion (n = 2 SROM and 3 AROM), and intact CA (n = 2 SROM and 2 AROM) dissected near the placenta and adjacent to the identified rupture site. Rupture region chorion dissected from AROM membranes were 92% stiffer than rupture region chorion from SROM membranes. Intact CA harvested from AROM membranes were stiffer than samples taken from SROM membranes ($p = 0.04$). No significant differences were seen in the amnion. Data are reported as mean ± SEM.

Incremental cyclic tests were performed to mimic the loading conditions during labor and cervical dilation and were thus analyzed for failure conditions, including failure stress, failure strain, and toughness. Incremental cyclic tests had a pronounced difference in the stress-strain curves between SROM and AROM amnion (Figure 5.5). Amnion harvested from SROM membranes experienced a significant increase in stress prior to failure (p = 0.06) and as a result required more energy to rupture (*i.e.,* toughness) than AROM membranes (p = 0.04). No significance was seen in the failure strain of amnion (Figure 5.6). Characterizing the failure conditions of chorion revealed no statistically significant differences, likely due to small sample sizes and large variation in biological tissue data. However, visual inspection of the failure stress and toughness revealed striking differences between the placental and rupture sites of SROM membranes that was absent in AROM membranes (Figure 5.7). Chorion from the placental site of SROM membranes required 152% more stress to rupture and 143% more energy (*i.e.,* toughness) than rupture region chorion from SROM membranes.

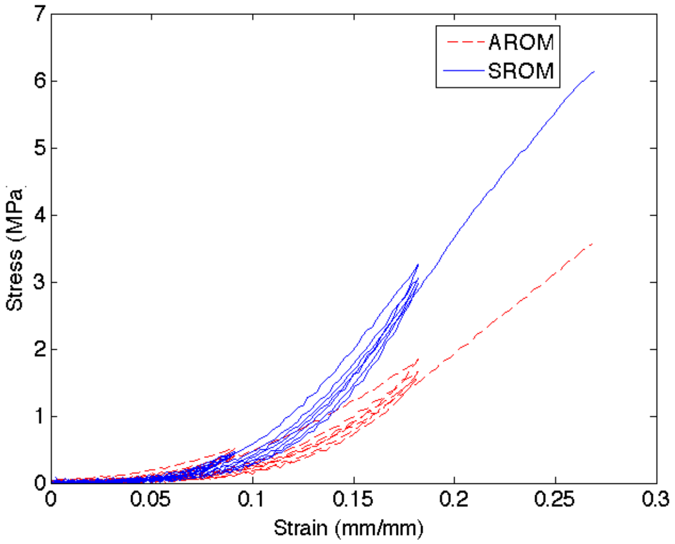

Figure 5.5. Representative response of placental SROM and AROM amnion during an incremental cyclic test.

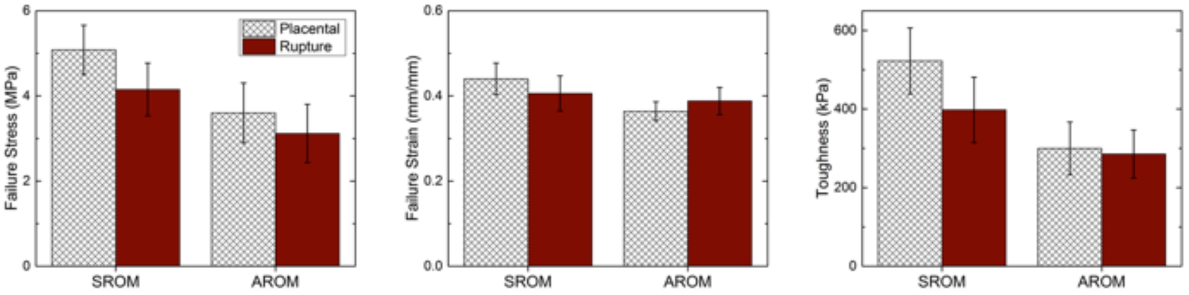

Figure 5.6. Failure stress, failure strain, and toughness of amnion (n = 7 SROM and 6 AROM) dissected near the placenta and adjacent to the identified rupture site. Amnion from SROM membranes had an increased failure stress (p = 0.06) and toughness (p = 0.04) compared to amnion from AROM membranes. Data are reported as mean ± SEM.

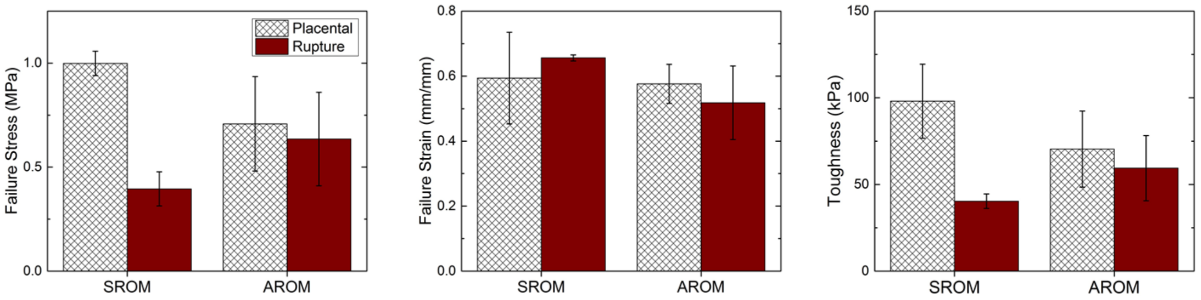

Figure 5.7. Failure stress, failure strain, and toughness of chorion (n = 2 SROM and 3 AROM) dissected near the placenta and adjacent to the identified rupture site. Although a lack in statistical power did not reveal significant differences, it is important to note that chorion taken from the placental site of SROM membranes required a 152% increase in stress to rupture and a 143% increase in toughness compared to chorion from the rupture region of SROM membranes. Data are reported as mean ± SEM.

Incremental stress relaxation tests were conducted to measure instantaneous and equilibrium moduli of amnion. Placental region SROM amnion was 34% stiffer than placental region AROM amnion (Figure 5.8): however, no statistically significant differences were seen between amnion from AROM and SROM membranes. There was a significant decrease in both the instantaneous (p = 0.08) and equilibrium moduli (p = 0.07) when comparing amnion from the placental site versus the rupture site within SROM membranes that was absent in AROM membranes (Figure 5.9).

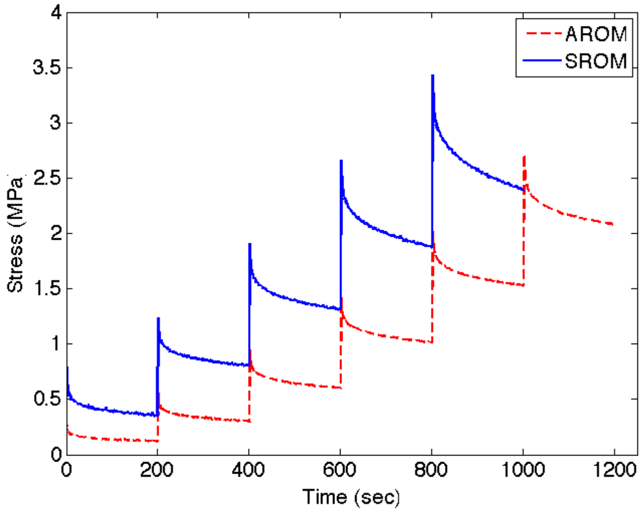

Figure 5.8. Representative incremental stress relaxation response of amnion harvested near the placenta from SROM and AROM membranes.

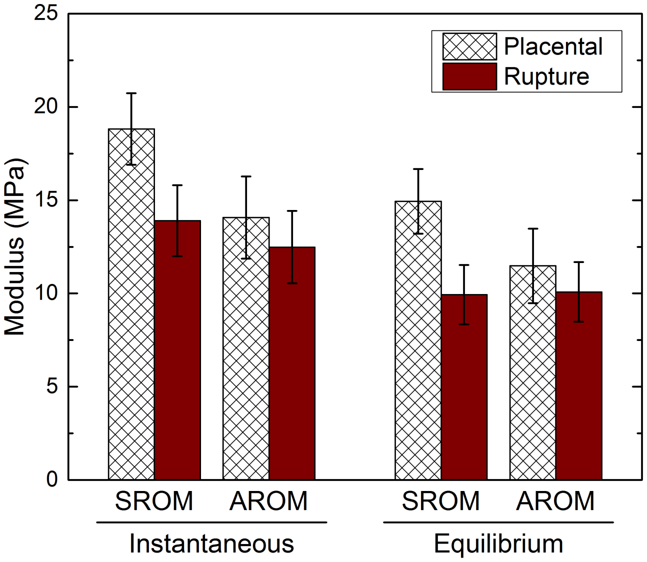

Figure 5.9. Instantaneous and equilibrium moduli of amnion (n = 12 SROM and 9 AROM) dissected near the placenta and adjacent to the identified rupture site. Amnion from SROM membranes had a significant decrease in both instantaneous (p = 0.08) and equilibrium (p = 0.07) moduli in samples taken near the rupture site as compared to samples from near the placenta. Data are reported as mean ± SEM.

Composite Modeling of the CA Bilayer to Predict Properties

Application of the rule of mixtures to the CA bilayer composite, utilizing the mean moduli of the amnion and chorion of AROM and SROM membranes, yielded results that were consistently greater than the experimentally measured values (Figure 5.10). The only exception to this trend was for rupture region samples from AROM membranes, which had experimental values greater than the rule of mixtures prediction.

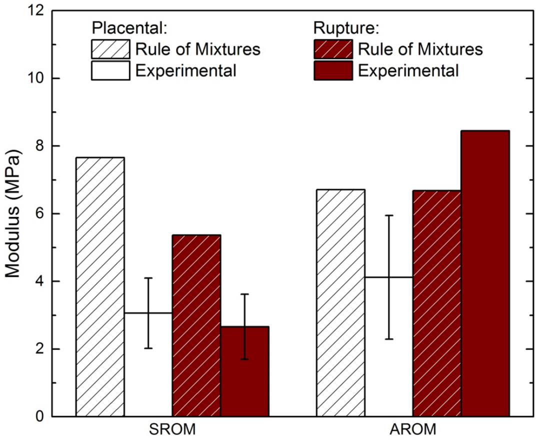

Figure 5.10. The rule of mixtures tended to overestimate the modulus of intact CA, except in the rupture region of AROM membranes. Data shown as mean ± standard deviation

Investigation of the CA Interfacial Behavior and Properties

Lap shear delamination tests were performed on specimens harvested adjacent to the placental disc ("Placental"), the identified rupture site ("Rupture"), and a mid-region between the placental and rupture sites ("Middle"). All three regions showed a non-linear, viscoelastic loading curve to a peak stress followed by a rapid decrease in stress typical of tissue failure (Figure 5.11). The delamination stress and interfacial stiffness decreased with increased distance from the placenta (Table 5.1). The chorioamnion interface adjacent to the identified site of rupture had a significantly smaller delamination stress than the middle (p = 0.015) and placental (p = 0.015) regions. There was no significant difference of the interfacial stiffness with region; however, a trend indicates decreased stiffness with increased distance from the placenta.

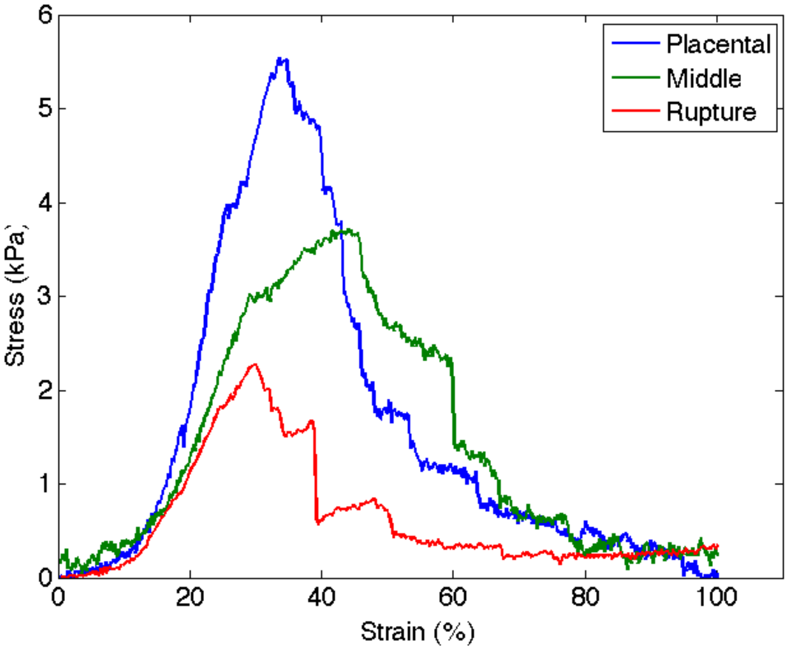

Figure 5.11. Representative delamination responses of the chorioamnion interface from placental, middle, and rupture regions shows a significant decrease in delamination stress with increased distance from the placenta.

Table 5.1. Delamination Stress and Interfacial Modulus of the Chorioamnion Interface at the Placental, Middle, and Rupture Regions of the Membrane (n = 3)

	Placental	Middle	Rupture	p-value
Delamination Stress (kPa)	4.33 ± 0.59	3.31 ± 0.29	1.67 ± 0.28	0.011
Interfacial Modulus (kPa)	28.56 ± 7.80	16.28 ± 1.60	12.35 ± 3.14	0.130

Data are reported as mean ± SEM.

Biochemical Analysis

Amnion samples proximal to the placenta and rupture site were subject to biochemical analysis in which total collagen content was quantified (Table 5.2). No statistical differences were observed between any of the groups.

Table 5.2. Total Collagen Content of Placental and Rupture Region Amnion from SROM and AROM Membranes (μg collagen/mg dry weight)

	SROM (n = 9)	AROM (n = 5)	p-value (AROM/SROM; Placental/Rupture)
Placental	345.8 ± 45.5	295.1 ± 30.0	0.508
Rupture	319.4 ± 23.6	319.3 ± 34.5	0.846

Data are reported as mean ± SEM.

Sulfated GAGs were quantified in both the amnion and chorion. Significant differences were observed in GAG concentration of chorion from the placental site versus rupture site (p = 0.06). This difference was more pronounced in the AROM membranes with a 26% increase in GAG concentration of chorion taken near the rupture site compared to the placental site (Figure 5.12). No significance differences were observed in the amnion.

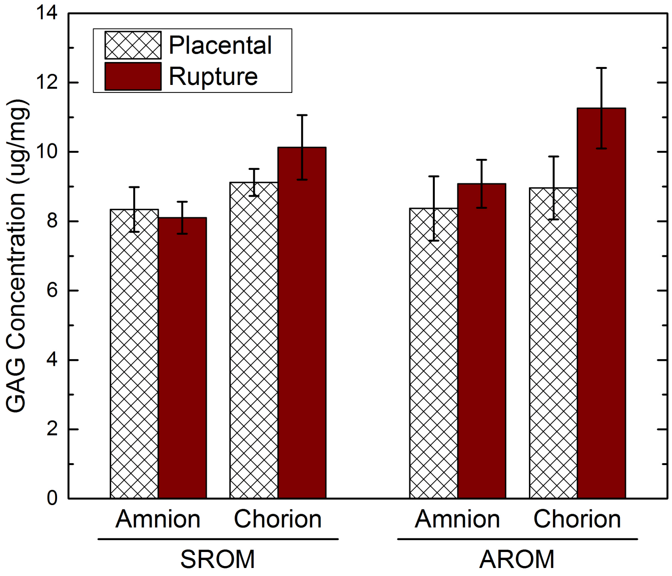

Figure 5.12. GAG concentration (μg/mg dry weight) of amnion (n = 12 SROM and 7 AROM) and chorion (n = 6 SROM and 5 AROM) dissected near the placenta and adjacent to the identified rupture site. Significant differences were seen when comparing chorion taken near the placental site versus rupture site (p = 0.06). No significant differences were observed in the amnion. Data are reported as mean ± SEM.

Histology

Masson's Trichrome stain of n = 7 SROM and n = 1 AROM CA membranes from placental and rupture regions illustrated substantial morphological differences between both amnion and chorion. SROM amnion appears to consist more of fiber strands that may have a higher degree of alignment leading to the consistent increase in damage of amnion during histological processing. The collagen rich portion of the chorion (reticular layer) in SROM membranes appears to be less dense and thin and the cellular portion (trophoblast layer) of the chorion appears to also be less compact than AROM membranes. On the other hand, AROM membranes exhibit a thick and compact collagen layer of amnion with a distinct amnion epithelial layer. AROM chorion also has a thick and distinct reticular layer of collagen preceding a dense layer of trophoblast cellular components (Figure 5.13). Ongoing analysis will determine if this trend is seen in additional AROM membranes in this study.

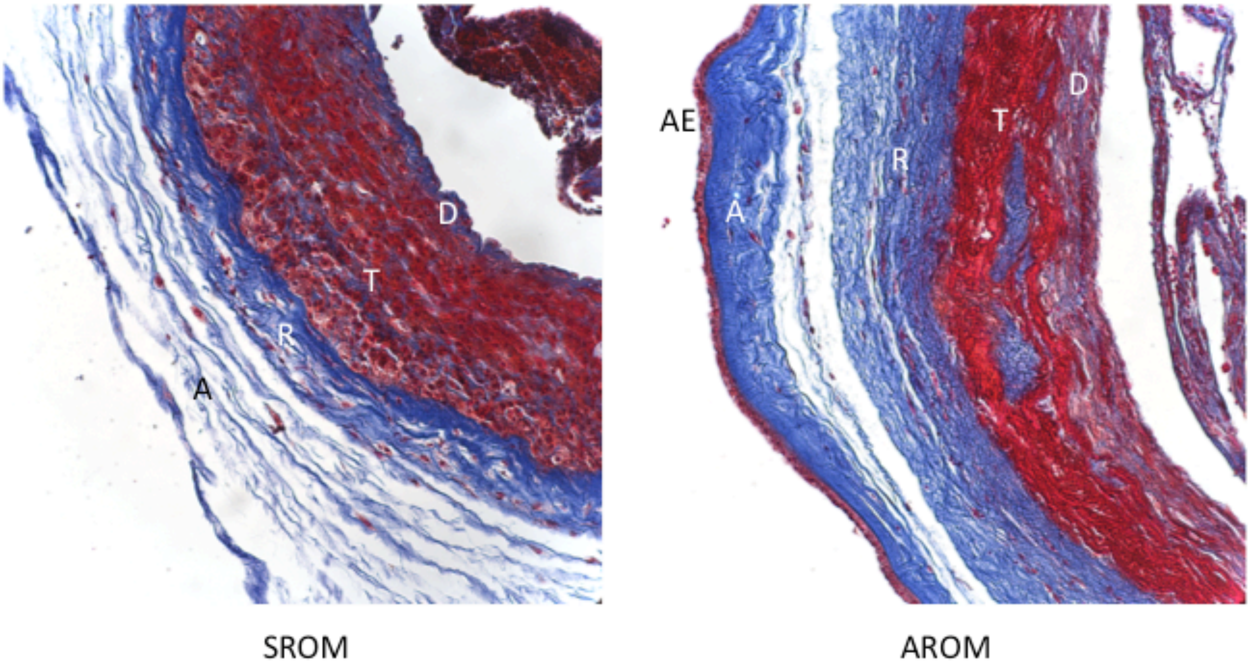

Figure 5.13. Representative Masson's Trichrome stained sections of placental chorioamnion from SROM and AROM membranes. The amnion and the reticular layer of the chorion seem to be more thick and compact in AROM membranes. (20x) AE: amniotic epithelium, A: amnion, R: reticular layer, T: trophoblast layer, D: decidua.

5.6 DISCUSSION

The aim of this study was to explore ECM and tissue property differences between spontaneously and artificially ruptured membranes to elucidate what causes healthy, term tissue to rupture at different times in pregnancy. To address such a complex problem multiple ECM components and tissue properties were studied in the amnion, chorion, and intact chorioamnion. Material properties indicative of tissue behavior during gestation (*i.e.* elastic modulus, instantaneous modulus and equilibrium modulus) were studied with cyclic and incremental stress relaxation methods. To mimic failure conditions during labor and cervical dilation, incremental cyclic tests were conducted and the failure stress, failure strain, and toughness were calculated. Additionally, the interfacial failure between the amnion and chorion was quantified with a lap shear test (delamination stress and interfacial modulus). Finally, the ECM was studied (*i.e.* collagen content, GAG content, and structural organization) to predict mechanisms that may dictate the observed mechanical response of the tissue.

When only considering amnion material properties it is unclear why some membranes rupture spontaneously while others do not. Contrary to our hypothesis, most measured parameters showed either no significant differences between amnion collected from AROM membranes versus SROM membranes, or there was an increase in modulus and conditions related to failure for SROM membranes compared to AROM membranes. When comparing amnion harvested adjacent to the placenta to amnion from near the rupture site, only the instantaneous and equilibrium moduli were significantly different. Additionally, this difference was only observed in SROM membranes. These combined results suggested that amnion from SROM membranes is a stronger and more robust material compared to amnion from AROM membranes. This finding contradicted our hypothesis that since SROM membranes rupture *in vivo* while AROM membranes technically do not, AROM membranes must be stiffer than SROM membranes. However, this trend does agree with previous literature that found preterm ruptured membranes to be stiffer than term membranes. [19,87] Collectively, these confounding results suggest that amnion stiffness may be playing a role during *in vivo* membrane rupture; however, it does not fully explain the mechanics or timing of rupture at term.

Considering the CA membrane as a composite structure that is dependent on both the amnion and chorion provided more information about the timing of membrane rupture at term.

Cyclic testing of intact CA revealed that SROM membranes have a decreased composite modulus compared to AROM membranes. This finding agrees with the clinical observation that AROM membranes are “clinically strong”, meaning that they would have either not ruptured spontaneously or would have ruptured late into labor if they had not been punctured by a physician. Mechanical testing of isolated chorion showed similar trends to the intact CA although the differences were not statistically significant due to small sample sizes and large variance. Chorion from the rupture region of AROM membranes was stiffer than both the chorion from the rupture region of SROM membranes and the placental region of AROM membranes. Although no differences were seen with the failure stress or toughness between chorion from AROM and SROM membranes, striking decreases were recorded for chorion from the rupture region of SROM membranes. These combined results suggest that the chorion may be responsible for the increase in strength observed in intact AROM membranes as well as the decrease in stress and toughness needed to rupture SROM membranes.

The rule of mixtures, based on simple theory for calculating material properties of laminated composite materials, was used to calculate a predicted modulus of intact CA using the modulus and thickness measurements of separated amnion and chorion. Modulus values calculated with the rule of mixtures consistently overestimated the measured intact CA modulus, except in the case of CA from the rupture region of AROM membranes. This finding suggests that a structural component, other than the separate layers of amnion and chorion, may be responsible for the intact tissue strength in the rupture region of AROM membranes. We hypothesize that the interface between the amnion and chorion could be this component and thus contribute to the observed increase in experimental AROM modulus. Future studies will consider a composites analysis that will incorporate the strength of the interface.

Preliminary analyses of the shear properties at the interface between the chorion and amnion revealed a decrease in interfacial modulus and delamination stress with increased distance from the placenta. These results indicate that damage occurs at the interface in samples collected proximal to sites of rupture. As these samples were collected from term, non-labored, cesarean deliveries, this interfacial damage may be one potential mechanism that prepares the tissue for rupture at term. In other words, the composite model demonstrates that this interfacial region may play a critical role to the structural integrity of the CA. Failure of this interface prior to rupture of membranes may prevent a mechanical interaction between the chorion and amnion and thus disable the chorion from providing energy absorption and toughness to the composite CA bilayer. Brittle fracture of either layer would then likely ensue. Further testing of the interface delamination behavior is ongoing to fully elucidate the role that this critical interface plays in membrane function and timing of rupture *in vivo*; however, preliminary analysis of additional data indicates that the differences seen between the regions on the membrane may be reduced due to large standard deviations.

Biochemical analysis of collagen and sulfated GAG content indicated minimal differences in the amnion and an increase in GAG content in chorion at sites proximal to rupture regions. The increase in GAG content, in combination with increased modulus of rupture region chorion in AROM, suggests that decorin, one of the prevalent proteoglycans in the CA, may be elevated.[111,173] Increased decorin concentration would promote interactions with fibronectin and increased collagen cross-links in the tissue – leading to structural reinforcement within the ECM molecules.[179] Ongoing collagen cross-linking quantification of the amnion and chorion of these tissues will provide more information on whether this is the mechanism that could be strengthening AROM chorion.

Histological images of the CA membrane showed distinct differences between CA from SROM and AROM. Amnion in SROM consistently appeared shredded, perhaps an indication of greater collagen alignment, and resulted in fiber separation during processing. A greater degree of fiber alignment could account for the increased instantaneous modulus observed in the SROM amnion. The chorion also showed drastic differences between AROM and SROM membranes. In AROM, a more pronounced reticular layer of collagen preceded a dense layer of trophoblast cellular components. This thick collagen layer may also contribute to the increased modulus observed in chorion from AROM subjects. Ongoing quantification of collagen and collagen cross-linking within the chorion layer will indicate if the observed differences are due to an increased collagen concentration, organization, and/or cross-linking and also indicate the role that these ECM-level alterations play in the observed mechanical behavior.

This study was the first to our knowledge to quantify the ECM and tissue material properties of both the amnion and chorion in spontaneously and artificially ruptured membranes to elucidate what causes healthy, term tissue to rupture at different times in pregnancy. Our results indicate that the chorion, and not "the primary structural determinant" of amnion, was largely responsible for altering intact CA behavior *in vivo*, where the chorion contributed to an increase in modulus of rupture region CA from AROM subjects and a decrease in maximum stress and toughness of rupture region samples from SROM subjects. This finding validates the importance of the chorion in mechanics of the intact CA membrane, which contradicts previous studies that claimed the amnion to be largely responsible for CA membranes mechanics.[134,136] The mechanisms that caused an increase in modulus are the focus of ongoing analyses; however, these changes may be due to an increase in collagen content, organization, and/or cross-linking – and possibly due to an increase in decorin. Future work should also evaluate the relative content of specific proteoglycans including decorin and biglycan in the CA tissues. Here, our findings suggest that ECM and tissue property changes may alter the timing of CA rupture through mechanisms that may also cause preterm CA rupture. Therefore, future studies will investigate the ECM composition, structure and organization in combination with mechanical properties of amnion, chorion, and intact CA of PPROM membranes to further our understanding of the mechanisms that lead to preterm rupture.

CHAPTER 6

DISCUSSION AND CONCLUSIONS

In this dissertation we hypothesized that the cervix, the CA, and their substructures form a hierarchical and integrated load bearing system that undergoes mechanical failure to initiate birth. In particular, the alteration of ECM constituents, structure, and organization influences tissue material property losses, which in turn enables gross structural and functional tissue changes and, ultimately, tissue failure. The timing of this cascade is imperative to the outcome of the pregnancy, where tissue failure leads to preterm (< 37 weeks gestation) or term birth. Therefore, the aim of this dissertation was to elucidate the events leading to tissue failure in pregnancy by evaluating ECM and tissue material property changes that result in gross structural or functional tissue changes in both the cervix and CA membranes.

6.1 MAJOR FINDINGS

The work contained within this dissertation demonstrated that tissue material properties influence gross structural changes or functional tissue losses in tissues critical to a successful pregnancy outcome. In other words, the underlying ECM structure, chemistry, and function dictates the timing of tissue failure during or at the end of a term pregnancy. Therefore, the accurate *in vivo* characterization of the ECM or material properties of reproductive tissues providing structural support during pregnancy could assess the risk of and provide insight into the mechanisms that cause spontaneous preterm birth (SPTB).

Throughout gestation, the cervix and CA are critical for sustaining pregnancy by providing structural support and a barrier to infection. When altered ECM prematurely weakens either one of these tissues, the risk of preterm cervical failure and / or membrane rupture, and consequential pregnancy termination, is greatly increased. Detecting these tissue property changes early in pregnancy could initiate preventative measures such as bed rest, a cervical cerclage (the placement of a suture into and around the cervix to prevent further dilation), or hormonal therapies such as hydroxyprogesterone caproate injections (the synthetic version of progesterone that has been shown to prolong pregnancy) to prolong gestation.

In chapters 3 and 4, we developed a novel technique to measure cervical stiffness using ultrasound elastography (UE). We found that a reference standard was required in each image for comparing tissue strain measurements across multiple imaging sessions, and that the strain undergoes significant dissipation into the tissue with increased distance from the transducer probe. To correct for this dissipation, an analytical solution was formulated that incorporated a Hertzian contact mechanics analysis. With further validation on the human cervix and other heterogeneous material systems, this technique shows promise for monitoring cervical stiffness *in vivo* to detect premature softening.

In chapter 5 we aimed to elucidate mechanisms that cause preterm rupture of CA by characterizing material properties and ECM composition and organization of both the amnion and chorion in term membranes with different modes of rupture. We found that clinically strong membranes (*i.e.* artificially ruptured CA) demonstrated an increased modulus in the rupture region of chorion and intact CA, but not in the amnion. Therefore, while the amnion is by far the stiffer layer, the chorion is largely responsible for the increase in modulus of intact CA of artificially ruptured membranes thus demonstrating its importance in membrane mechanics. These results suggest that failure of the chorion to support and integrate with the amnion may play a large role in causing preterm rupture and should be included in future studies.

Overall, the studies included in this dissertation provide novel approaches to measuring material properties and detecting ECM alterations in tissues that are critical for providing structural support during gestation. Thus, the work described in this dissertation enables future studies to evaluate how the collective influences of cervical and CA gross structure and function link with ECM biochemistry, structure, and organization to ultimately lead to SPTB. Moreover, further investigation of this integrated system of tissues in pregnancy may provide cues for future research on prevention of SPTB and other disorders of pregnancy.

6.2 CLINICAL RELEVANCE

Preterm birth affects 13 million babies globally every year. Despite significant advances in medical technology over the past 100 years, SPTB rates have remained essentially unchanged. A major culprit lies in our poor understanding of the mechanisms underlying SPTB. We currently lack fidelity in accurately assessing risk for a patient to deliver preterm and especially for women in their first pregnancy who have limited obstetric history. The studies in this dissertation introduce novel methods for assessing tissue material properties in an effort to understand and assess the risk of SPTB that may lead to new approaches to improve clinical care and outcomes.

Cervical stiffness is imperative for the successful, term pregnancy. Premature softening of the cervix, cervical insufficiency, can result in an increased risk of preterm labor or early termination of the pregnancy. Current methods for detecting softening of the internal *os* occur after structural changes are evident in a traditional B-mode ultrasound image of the cervix. Chapters 3 and 4 of this study present a novel method for determining cervical stiffness using UE. Detecting stiffness changes prior to structural changes (*i.e.,* cervical funneling) could aid in the early detection of cervical insufficiency and thus indicate the need for medical techniques that have been shown to prolong pregnancies at risk for preterm delivery, such as the administration of synthetic progesterone or placement of a cerclage to suture the insufficient cervix closed.

Hydroxyprogesterone caproate injections (synthetic progesterone) have been shown to lower the risk of preterm birth, but are typically only administered to women who have a history of preterm delivery since the injections are not intended to stop preterm labor and it is undesirable to expose a fetus to any unnecessary pharmaceuticals *in utero*. Additionally, it is currently unknown how the synthetic progesterone works to prevent labor. The use of the UE techniques described in this dissertation could reveal if the injections stiffen the cervix to prolong pregnancy. If the injections stiffen the cervix, then physicians could use UE to assess the stiffness of their patient's cervix, make more informed decisions about whether to begin administering the synthetic progesterone, and then continue to monitor the stiffness of the cervix for the remainder of the pregnancy to assess the effectiveness of the drug. This technique, therefore, has the potential to significantly improve the detection and management of cervical insufficiency.

In the case of a short cervix, physicians may decide to place a cerclage. However, the timing of cerclage placement is imperative for its success. Cerclage placement after 20 weeks gestation increases the risk of preterm premature membrane rupture (PPROM), chorioamnionitis, and intrauterine infection.[61] Additionally, studies have shown that cerclage placement closer to the internal *os* transfers more of the load off of the cervix and onto the suture.[68] Therefore, it is critical that cervical softening and resulting cervical shortening be detected as early as possible during gestation so that a cerclage can be placed at the optimum time and location along the cervix, increasing the likelihood of a term pregnancy. UE would aid in the early detection of a soft cervix, indicating to the physician that the cervical length will need to be monitored on a regular basis. This frequent monitoring ensures that a cerclage is placed at the right time and location along the cervix for patients who develop a short cervix.

Timing of CA membrane rupture is also crucial for pregnancy outcome. Membranes that rupture prior to term can cause an increased risk of infection, preterm labor, and delivery. Chapter 5 of this study presented an evaluation of the mechanics and related analysis of ECM composition and structure of term membranes that are, *a priori*, considered to be clinically strong versus weak (*i.e.,* AROM vs SROM). Understanding the mechanisms that lead to a difference in term membrane rupture timing may provide insight into preterm rupture. Understanding the causes of preterm rupture provides a foundation for future development of techniques that can predict the timing of rupture *in vivo* and possibly lower the prevalence of PPROM.

6.3 SCOPE WITHIN THE EXISTING LITERATURE

UE was developed as a means for detecting large differences in strain within the field of view for the purpose of detecting stiff tumors within soft tissues.[5,74,114,160] Several researchers have explored the ability of this technique to provide a quantitative measure of tissue stiffness without fully understanding the fundamental mechanics that are involved. They have incorrectly used UE to compare images without knowledge of the force[5,72,160,161,175], without an applied compression[158], or without correcting for strain dissipation when using a transvaginal ultrasound transducer probe[64,66,115]. Chapters 3 and 4 of this dissertation provided concrete evidence that cervical stiffness cannot be simply estimated from strain comparisons within or between UE images and from imaging sessions without a protocol to standardize the elastography measurements. Strain is a measure of displacement and does not rely directly on a material property (*e.g.,* modulus). However, a constitutive relationship such as linear elastic Hooke's law does relate strain to the applied stress through a material constant, or the material property of modulus. Here, the stress in the tissue must be ascertained by use of a force transducer[77]. As measuring the exceptionally low magnitude loads that cause substantial deformation of soft tissues is difficult, and the intrusion of devices to measure such loads would likely be painful or intimidating to the patient, a reference material of known properties that is included in every imaging session can alternately be used to calculate the applied stress (or force), again using Hooke's law.[38,64,176] While others have simply applied this linear relationship[64], we observed that, when using a transvaginal transducer probe, a strain distribution was produced in the tissue that does not follow the linear relationship assumed by Hooke's law. Previously published studies have recognized the need for correcting this strain dissipation but have not attempted to do so.[64,66,115] In chapter 4, we proposed an initial analytical solution to account for the strain dissipation within the analyzed volume of tissue and demonstrated its efficacy. To our knowledge this was the first analytical solution developed for calculating cervical stiffness using UE that corrects for the observed strain dissipation. While our results showed vast improvement over the linear Hooke's law approximation, future advancements using complex computational and numerical approaches (*i.e.,* modulus) are needed to provide a true measure of tissue properties *in situ.*

It has been predicted that the strength of the CA membrane is one of the primary contributors to the timing of membrane rupture *in vivo* and that the ECM components and structural organization dictate the strength[33,131]; however, the etiology of PPROM is poorly understood. Previous CA membrane studies have concluded that the amnion is the primary structural determinant that dictates membrane behavior and rupture *in vivo.*[134,136] These previously published studies predicated this notion based on the observation that amnion is much stiffer than chorion and thus assumed that stiffer materials dictate composite behavior. [134,136] Therefore, several studies have characterized possible individual contributors to membrane rupture such as amnion material properties, structure, or composition without considering the chorion or the chorioamnion interface contributions to the composite material properties.[29,85,131] Additionally, others have attempted to characterize the pathological condition of PPROM without fully understanding what causes term membranes to rupture at different times during pregnancy.[19,134,135,144] It is difficult to understand the mechanisms that cause preterm rupture when it is poorly understood what causes normal, term membranes to rupture. Our results indicated that the chorion plays a much larger role in the CA mechanical response than previously thought and may even dictate rupture timing. These findings could shift the focus of

CA membrane research to include analysis of the chorion instead of primarily evaluating the amnion alone. By considering all layers of the composite CA, the mechanisms leading to PPROM may be understood. Additionally, this was the first study to our knowledge to investigate the mechanisms that cause differing rupture times at term by investigating both the ECM and tissue property changes of clinically weak and clinically strong membranes (SROM vs AROM). The approach outlined herein for understanding what causes membrane rupture at term could illuminate the ECM and tissue property changes that may lead to preterm rupture.

6.4 FUTURE STUDIES

The work described in this dissertation enables future studies that evaluate the collective influences of tissue mechanics and ECM biochemistry, structure, and organization on the pathways that ultimately lead to SPTB. In particular, using the UE techniques described in this work (Chapters 3 and 4) to analyze cervical stiffness throughout gestation could provide a unique analysis of the softening process in the human cervix over time or of the changes in the cervix after administration of pharmaceuticals that are known to prolong pregnancy (*e.g.* synthetic progesterone). Past studies have only been able to gather stiffness values on human tissue at one point in time after hysterectomy. The ability to quantify stiffness non-invasively reveals the unique opportunity to study the same tissue at several time points in gestation.

It is hypothesized in this dissertation that the mechanism contributing to SPTB is a complex interaction between several tissues that provide structural support during pregnancy. To gain a better understanding of the interaction between the cervix and CA in determining the timing of delivery, the CA membranes could be collected post-delivery on the same patients as cervical elastography image collection. CA membranes could be analyzed with the protocol developed in chapter 5 to understand the ECM composition as well as the material properties of these membranes. By combining the cervical UE stiffness, CA tissue properties, and clinical outcome of the pregnancy (including membrane rupture time, time of delivery, gestational age at delivery and mode of rupture), a greater understanding of the events that led up to delivery could be ascertained. Additionally, studying these combined mechanisms on women who are at risk for preterm delivery as well as a control group could be the first study to characterize tissue interactions that contribute to term versus preterm delivery.

Finally, to expand upon the results discussed in chapter 5, which presented a change in GAG concentration that correlated with modulus differences in these tissues, *in vitro* studies could be conducted on both the amnion and chorion to alter GAG concentrations. Tissues with increased GAG concentrations (chorion from the rupture region of AROM subjects) can be exposed to chontroitinase ABC overnight to remove GAGs while control samples are in a buffer without chondroitinase. The mechanical response of the control group to the group with removed GAGs can then be compared. This would enable analyses that would directly relate to the SROM and AROM membranes to understand if the observed decrease in GAGs of the SROM membranes caused the decrease in modulus measured in this study. Additional exploratory studies could be conducted on healthy, term membranes to investigate the mechanical role of other ECM components using protocols to digest out the constituent of interest. This type of analysis provides a more controlled experiment that could address the problem of limited sample numbers for clinical groups experienced in this dissertation.

6.5 CONCLUDING REMARKS

This dissertation addressed the broad goal of improving our understanding of the mechanical properties and functional tissue alterations that occur in tissues critical to a term pregnancy. Specifically, this dissertation addressed the tissues that make up the integrated mechanical system of the cervix and the CA, where failure of either tissue initiates irreversible alterations in both tissues that are necessary for birth. The collective studies within this dissertation demonstrated that:

- UE holds promise for quantifying *in vivo* cervical stiffness; however it is critical to include both a reference standard and to correct for strain dissipation caused by a spherical tip transducer probe.
- The chorion may be largely responsible for altered mechanical properties in the CA membrane at term and could likely contribute to the timing of rupture *in vivo.*

In conclusion, the accurate *in vivo* characterization of the ECM and material properties of reproductive tissues providing structural support during pregnancy provides insight into the timing of delivery and could aid in assessing the risk of preterm birth.

BIBLIOGRAPHY

1. Volume 8, mechanical testing and evaluation. In: *ASM handbooks*. Materials Park, Ohio, USA: ASM International; 2012-2013.

2. CDC - preterm birth-prematurity - maternal infant health - reproductive health. http://www.cdc.gov/reproductivehealth/maternalinfanthealth/pretermbirth.htm. Accessed 4/18/2014, 2014.

3. The influence of different preservation and sterilisation steps on the histological properties of amnion allografts — light and scanning electron microscopic studies - springer. http://link.springer.com/article/10.1023/B:CATB.0000022276.47180.96. Accessed 4/18/2014, 2014.

4. Aigner F, Pallwein L, Schocke M, et al. Comparison of real-time sonoelastography with T2-weighted endorectal magnetic resonance imaging for prostate cancer detection. *J Ultrasound Med*. 2011;30(5):643-649.

5. Alhabshi SM, Rahmat K, Abdul Halim N, et al. Semi-quantitative and qualitative assessment of breast ultrasound elastography in differentiating between malignant and benign lesions. *Ultrasound Med Biol*. 2013;39(4):568-578.

6. Al-Zaid NS, Bou-Resli MN, Goldspink G. Bursting pressure and collagen content of fetal membranes and their relation to premature rupture of the membranes. *Br J Obstet Gynaecol*. 1980;87:227-229.

7. Ananth CV, Vintzileos AM. Epidemiology of preterm birth and its clinical subtypes. *J Matern Fetal Neonatal Med*. 2006;19:773-782.

8. Aplin JD, Campbell S, Allen TD. The extracellular matrix of human amniotic epithelium: Ultrastructure, composition and deposition. *J Cell Sci*. 1985;79:119-136.

9. Arechavaleta-Velasco F, Ogando D, Parry S, Vadillo-Ortega F. Production of matrix metalloproteinase-9 in lipopolysaccharide-stimulated human amnion occurs through an autocrine and paracrine proinflammatory cytokine-dependent system. *Biol Reprod*. 2002;67:1952-1958.

10. Arikat S, Novince RW, Mercer BM, et al. Separation of amnion from choriodecidua is an integral event to the rupture of normal term fetal membranes and constitutes a significant component of the work required. *Am J Obstet Gynecol*. 2006;194:211-217.

11. Artal R, Burgeson RE, Hobel CJ, Hollister D. An in vitro model for the study of enzymatically mediated biomechanical changes in the chorioamniotic membranes. *Am J Obstet Gynecol*. 1979;133:656-659.

12. Artal R, Sokol RJ, Neuman M, Burstein AH, Stojkov J. The mechanical properties of prematurely and non--prematurely ruptured membranes. methods and preliminary results. *Am J Obstet Gynecol*. 1976;125:655-659.

13. Aspden RM. Collagen organisation in the cervix and its relation to mechanical function. *Coll Relat Res*. 1988;8(2):103-112.

14. Athayde N, Romero R, Gomez R, et al. Matrix metalloproteinases-9 in preterm and term human parturition. *J Matern Fetal Med*. 1999;8:213-219.

15. Baacke KA, Edwards RK. Preinduction cervical assessment. *Clin Obstet Gynecol*. 2006;49:564-572.

16. Bakke T. Cervical consistency in women of fertile age measured with a new mechanical instrument. *Acta Obstet Gynecol Scand*. 1974;53(4):293-302.

17. Barr RG, Destounis S, Lackey LB,2nd, Svensson WE, Balleyguier C, Smith C. Evaluation of breast lesions using sonographic elasticity imaging: A multicenter trial. *J Ultrasound Med*. 2012;31(2):281-287.

18. Behzad F, Dickinson MR, Charlton A, Aplin JD. Brief communication: Sliding displacement of amnion and chorion following controlled laser wounding suggests a mechanism for short-term sealing of ruptured membranes. *Placenta*. 1994;15:775-778.

19. Benson-Martin J, Zammaretti P, Bilic G, et al. The young's modulus of fetal preterm and term amniotic membranes. *Eur J Obstet Gynecol Reprod Biol*. 2006;128:103-107.

20. Bishop EH. Pelvic scoring for elective induction. *Obstet Gynecol*. 1964;24:266-268.

21. Borazjani A, Weed BC, Patnaik SS, et al. A comparative biomechanical analysis of term fetal membranes in human and domestic species. *Am J Obstet Gynecol*. 2011;204(4):365.e25-365.e36.

22. Boudreau N, Sympson CJ, Werb Z, Bissell MJ. Suppression of ICE and apoptosis in mammary epithelial cells by extracellular matrix. *Science*. 1995;267:891-893.

23. Bou-Resli MN, Al-Zaid NS, Ibrahim ME. Full-term and prematurely ruptured fetal membranes. an ultrastructural study. *Cell Tissue Res*. 1981;220:263-278.

24. BOURNE GL. The microscopic anatomy of the human amnion and chorion. *Am J Obstet Gynecol*. 1960;79:1070-1073.

25. Boussinesq J. *Application des potentials à l'etude de l'équilibre et du mouvement des solides élastiques*. Paris: Gauthier-Villars; 1885.

26. Brown XQ, Ookawa K, Wong JY. Evaluation of polydimethylsiloxane scaffolds with physiologically-relevant elastic moduli: Interplay of substrate mechanics and surface chemistry effects on vascular smooth muscle cell response. *Biomaterials*. 2005;26(16):3123-3129.

27. Bryant-Greenwood GD. The extracellular matrix of the human fetal membranes: Structure and function. *Placenta*. 1998;19(1):1-11.

28. Bude RO, Adler RS. An easily made, low-cost, tissue-like ultrasound phantom material. *Journal of Clinical Ultrasound*. 1995;23(4):271-273.

29. Buerzle W, Mazza E. On the deformation behavior of human amnion. *J Biomech*. 2013;46(11):1777-1783.

30. Buhimschi IA, Kramer WB, Buhimschi CS, Thompson LP, Weiner CP. Reduction-oxidation (redox) state regulation of matrix metalloproteinase activity in human fetal membranes. *Am J Obstet Gynecol*. 2000;182:458-464.

31. Cabrol D. Cervical distensibility changes in pregnancy, term and preterm labor. *Semin Perinatol*. 1991;15(2):133-139.

32. Cabrol D, Jannet D, Le Houezec R, Dudzik W, Bonoris E, Cedard L. Mechanical properties of the pregnant human uterine cervix use of an instrument to measure the index of cervical distensibility. *Gynecol Obstet Invest*. 1990;29:32-36.

33. Calvin SE, Oyen M. Microstructure and mechanics of the chorioamnion membrane with an emphasis on fracture properties. *Ann N Y Acad Sci*. 2007;1101:166-185.

34. Carrillo F, Gupta S, Balooch M, et al. Nanoindentation of polydimethylsiloxane elastomers: Effect of crosslinking, work of adhesion, and fluid environment on elastic modulus. *J Mater Res*. 2005;20(10):2820.

35. Cerruti V. *Roma, acc. lincei, mem. fis. mat.*; 1882.

36. Cespedes I. Elastography: Elasticity imaging using ultrasound with application to muscle and breast in vivo. *Ultrason Imaging*. 1993;15(2):73-88.

37. Chang CJ, Yang JY. Frozen preservation of human amnion and its use as a burn wound dressing. *Changgeng Yi Xue Za Zhi*. 1994;17(4):316-324.

38. Chino K, Akagi R, Dohi M, Fukashiro S, Takahashi H. Reliability and validity of quantifying absolute muscle hardness using ultrasound elastography. *PLoS ONE*. 2012;7(9):e45764.

39. Cho N, Jang M, Lyou C. Distinguishing benign from malignant masses at breast US: Combined US elastography and color doppler US—Influence on radiologist accuracy. *Radiology*. 2012;262(1).

40. Conrad J, Tokarz R, Williford J. Anatomic site and stretch modulus in the human cervix. *Dilatation of the Uterine Cervix: Connective Tissue Biology and Clinical Management*. 1980:255-264.

41. Cox SM, Casey ML, MacDonald PC. Accumulation of interleukin-1beta and interleukin-6 in amniotic fluid: A sequela of labour at term and preterm. *Hum Reprod Update*. 1997;3:517-527.

42. Danforth DN. The fibrous nature of the human cervix, and its relation to the isthmic segment in gravid and nongravid uteri. *Am J Obstet Gynecol*. 1947;53:541-560.

43. Danforth DN, McElin TW, States MN. Studies on fetal membranes. I. bursting tension. *Am J Obstet Gynecol*. 1953;65:480-490.

44. De Ceuninck F, Sabatini M, Pastoureau P. Cartilage and osteoarthritis. *Springer Science & Business Media*. 2004.

45. DeWall RJ, Varghese T, Kliewer MA, Harter JM, Hartenbach EM. Compression-dependent viscoelastic behavior of human cervix tissue. *Ultrason Imaging*. 2010;32:214-228.

46. Drakonaki EE, Allen GM. Magnetic resonance imaging, ultrasound and real-time ultrasound elastography of the thigh muscles in congenital muscle dystrophy. *Skeletal Radiol*. 2010;39(4):391-396.

47. Duyl WAv, Zon,A T M van der, Drogendijk AC. Stress relaxation of the human cervix: A new tool for diagnosis of cervical incompetence. *Clinical Physics and Physiological Measurement*. 1984;5(3):207-218.

48. El Khwad M, Pandey V, Stetzer B, et al. Fetal membranes from term vaginal deliveries have a zone of weakness exhibiting characteristics of apoptosis and remodeling. *J Soc Gynecol Investig*. 2006;13:191-195.

49. El Khwad M, Stetzer B, Moore RM, et al. Term human fetal membranes have a weak zone overlying the lower uterine pole and cervix before onset of labor. *Biol Reprod*. 2005;72:720-726.

50. El Maradny E, Kanayama N, Halim A, Maehara K, Terao T. Stretching of fetal membranes increases the concentration of interleukin-8 and collagenase activity. *Am J Obstet Gynecol*. 1996;174:843-849.

51. Evaldson GR, Larsson B, Jiborn H. Is the collagen content reduced when the fetal membranes rupture? A clinical study of term and prematurely ruptured membranes. *Gynecol Obstet Invest*. 1987;24:92-94.

52. Fawthrop RK, Ockleford CD. Cryofracture of human term amniochorion. *Cell Tissue Res*. 1994;277:315-323.

53. Feltovich H, Hall TJ, Berghella V. Beyond cervical length: Emerging technologies for assessing the pregnant cervix. *Am J Obstet Gynecol*. 2012;207(5):345-354.

54. Foltz CM, Russo RG, Siegal GP, Terranova VP, Liotta LA. Interactions of tumor cells with whole basement membrane in the presence or absence of endothelium. *Prog Clin Biol Res*. 1982;89:353-371.

55. Fortunato SJ, Menon R, Bryant C, Lombardi SJ. Programmed cell death (apoptosis) as a possible pathway to metalloproteinase activation and fetal membrane degradation in premature rupture of membranes. *Am J Obstet Gynecol*. 2000;182:1468-1476.

56. Fortunato SJ, Menon R, Lombardi SJ. Role of tumor necrosis factor-alpha in the premature rupture of membranes and preterm labor pathways. *Am J Obstet Gynecol*. 2002;187:1159-1162.

57. Fortunato SJ, Menon R, Lombardi SJ. MMP/TIMP imbalance in amniotic fluid during PROM: An indirect support for endogenous pathway to membrane rupture. *J Perinat Med*. 1999;27:362-368.

58. Fratzl P. Collagen: Structure and Mechanics. *Springer Science + Business Media*. 2008.

59. Ganne-Carrie N, Ziol M, de Ledinghen V, et al. Accuracy of liver stiffness measurement for the diagnosis of cirrhosis in patients with chronic liver diseases. *Hepatology*. 2006;44:1511-1517.

60. Garra BS, Cespedes EI, Ophir J, et al. Elastography of breast lesions: Initial clinical results. *Radiology*. 1997;202(1):79-86.

61. Gary CF, Gant N, Leveno K, Gilstrap L, Hauth J, Wenstrom K. Williams obstetrics. *New York: Mc Grow–Hill*. 2005:823-829.

62. GRANSTROM L, EKMAN G, ULMSTEN U, MALMSTROM A. Changes in the connective tissue of corpus and cervix uteri during ripening and labour in term pregnancy. *BJOG: An International Journal of Obstetrics and Gynaecology*. 1989;96(10):1198-1202.

63. Gray H. Gray's anatomy: Anatomy of the human body. *Lea & Febiger*. 1918.

64. Hee L, Sandager P, Petersen O, Uldbjerg N. Quantitative sonoelastography of the uterine cervix by interposition of a synthetic reference material. *Acta Obstet Gynecol Scand*. 2013;92(11):1244-1249.

65. Helmig R, Oxlund H, Petersen LK, Uldbjerg N. Different biomechanical properties of human fetal membranes obtained before and after delivery. *Eur J Obstet Gynecol Reprod Biol*. 1993;48:183-189.

66. Hernandez-Andrade E, Hassan SS, Ahn H, et al. Evaluation of cervical stiffness during pregnancy using semiquantitative ultrasound elastography. *Ultrasound in Obstetrics & Gynecology*. 2013;41(2):152-161.

67. Hertz H. Über die berührung fester elastischer körper (on the contact of elastic solids). *J. reine und angewandte Mathematik*. 1882;92.

68. House M, Socrate S. The cervix as a biomechanical structure. *Ultrasound in Obstetrics and Gynecology*. 2006;28(6):745-749.

69. House M, Kaplan DL, Socrate S. Relationships between mechanical properties and extracellular matrix constituents of the cervical stroma during pregnancy. *Semin Perinatol*. 2009;33:300-307.

70. Iams JD. Cervical incompetence. *Maternal Fetal Medicine*. 1999.

71. Iams JD, Goldenberg RL, Meis PJ, et al. The length of the cervix and the risk of spontaneous premature delivery. national institute of child health and human development maternal fetal medicine unit network. *N Engl J Med*. 1996;334:567-572.

72. Iglesias-Garcia J, Larino-Noia J, Abdulkader I, Forteza J, Dominguez-Munoz JE. Quantitative endoscopic ultrasound elastography: An accurate method for the differentiation of solid pancreatic masses. *Gastroenterology*. 2010;139(4):1172-1180.

73. Ito A, Kitamura K, Mori Y, Hirakawa S. The change in solubility of type I collagen in human uterine cervix in pregnancy at term. *Biochem Med*. 1979;21(3):262-270.

74. Itoh A, Ueno E, Tohno E, et al. Breast disease: Clinical application of US elastography for diagnosis. *Radiology*. 2006;239:341-350.

75. Johnson K. *Contact mechanics*. Cambridge University Press; 1985.

76. Kamoi K, Okihara K, Ochiai A, et al. The utility of transrectal real-time elastography in the diagnosis of prostate cancer. *Ultrasound Med Biol*. 2008;34(7):1025-1032.

77. Karimi H, Fenster A, Samani A. A novel fast full inversion based breast ultrasound elastography technique. *Phys Med Biol*. 2013;58(7):2219-2233.

78. Keene DR, Sakai LY, Lunstrum GP, Morris NP, Burgeson RE. Type VII collagen forms an extended network of anchoring fibrils. *J Cell Biol*. 1987;104(3):611-621.

79. Khanafer K, Duprey A, Schlicht M, Berguer R. Effects of strain rate, mixing ratio, and stress–strain definition on the mechanical behavior of the polydimethylsiloxane (PDMS) material as related to its biological applications. *Biomed Microdevices*. 2009;11(2):503.

80. Kinoshita K, Satoh K, Sakamoto S. Human amniotic membrane and prostaglandin biosynthesis. *Biol Res Pregnancy Perinatol*. 1984;5:61-67.

81. Kiss MZ, Hobson MA, Varghese T, et al. Frequency-dependent complex modulus of the uterus: Preliminary results. *Phys Med Biol*. 2006;51:3683-3695.

82. Kleissl HP, van der Rest M, Naftolin F, Glorieux FH, de Leon A. Collagen changes in the human uterine cervix at parturition. *Am J Obstet Gynecol*. 1978;130:748-753.

83. Kumar D, Fung W, Moore RM, et al. Proinflammatory cytokines found in amniotic fluid induce collagen remodeling, apoptosis, and biophysical weakening of cultured human fetal membranes. *Biol Reprod*. 2006;74:29-34.

84. Kumar D, Novince R, Strohl A, et al. A new methodology to measure strength of adherence of the fetal membrane components, amnion and the choriodecidua. *Placenta*. 2009;30:560-563.

85. Kumar D, Schatz F, Moore RM, et al. The effects of thrombin and cytokines upon the biomechanics and remodeling of isolated amnion membrane, in vitro. *Placenta*. 2011;32(3):206-213.

86. Lavery JP, Miller CE. Deformation and creep in the human chorioamniotic sac. *Am J Obstet Gynecol*. 1979;134:366-375.

87. Lavery JP, Miller CE. The viscoelastic nature of chorioamniotic membranes. *Obstet Gynecol*. 1977;50:467-472.

88. Lavery JP, Miller CE, Knight RD. The effect of labor on the rheologic response of chorioamniotic membranes. *Obstet Gynecol*. 1982;60:87-92.

89. Leppert PC. Anatomy and physiology of cervical ripening. *Clin Obstet Gynecol*. 1995;38:267-279.

90. Leppert PC, Keller S, Cerreta J, Hosannah Y, Mandl I. The content of elastin in the uterine cervix. *Arch Biochem Biophys*. 1983;222:53-58.

91. Leppert PC, Yu SY, Keller S, Cerreta J, Mandl I. Decreased elastic fibers and desmosine content in incompetent cervix. *Am J Obstet Gynecol*. 1987;157:1134-1139.

92. Linnala A, Balza E, Zardi L, Virtanen I. Human amnion epithelial cells assemble tenascins and three fibronectin isoforms in the extracellular matrix. *FEBS Lett*. 1993;317:74-78.

93. Lopez Bernal A, Hansell DJ, Khong TY, Keeling JW, Turnbull AC. Prostaglandin E production by the fetal membranes in unexplained preterm labour and preterm labour associated with chorioamnionitis. *Br J Obstet Gynaecol*. 1989;96:1133-1139.

94. Maclachlan TB. A method for the investigation of the strength of the fetal membranes. *Am J Obstet Gynecol*. 1965;91:309-313.

95. Madri JA, Williams SK. Capillary endothelial cell cultures: Phenotypic modulation by matrix components. *J Cell Biol*. 1983;97:153-165.

96. Malak TM, Bell SC. Fetal membranes structure and prelabour rupture. *Fetal and Maternal Medicine Review*. 1996;8:143-164.

97. Malak TM, Bell SC. Structural characteristics of term human fetal membranes: A novel zone of extreme morphological alteration within the rupture site. *Br J Obstet Gynaecol*. 1994;101:375-386.

98. Malak TM, Ockleford CD, Bell SC, Dalgleish R, Bright N, Macvicar J. Confocal immunofluorescence localization of collagen types I, III, IV, V and VI and their ultrastructural organization in term human fetal membranes. *Placenta*. 1993;14:385-406.

99. Manabe Y, Himeno N, Fukumoto M. Tensile strength and collagen content of amniotic membrane do not change after the second trimester or during delivery. *Obstet Gynecol*. 1991;78:24-27.

100. Martin JA, Hamilton BE, Ventura SJ, Osterman MJK, Mathews TJ. Births: Final data for 2011. *National Vital Statistics Reports*. 2013;62(1).

101. Mass S, Rawlings D, Weiss J. PreView: Finite element pre-processing musculoskeletal research laboratories. http://mrl.sci.utah.edu/software/preview. Updated 2013.

102. Mass S, Rawlins D, Weiss J. PostView: Finite element post-processing musculoskeletal research laboratories. http://mrl.sci.utah.edu/software/postview. Updated 2012.

103. Mass SA, Ateshian GA, Weiss JA, Ellis BJ. FEBio: Finite elements for biomechanics. *Journal of Biomechanical Engineering*. 2012;134(1341).

104. Mathews TJ, MacDorman MF. Infant mortality statistics from the 2006 period linked birth/infant death data set. *National Vital Statistics Reports*. 2010;58.

105. Maymon E, Ghezzi F, Edwin SS, et al. The tumor necrosis factor alpha and its soluble receptor profile in term and preterm parturition. *Am J Obstet Gynecol*. 1999;181:1142-1148.

106. Mazza E, Nava A, Bauer M, Winter R, Bajka M, Holzapfel GA. Mechanical properties of the human uterine cervix: An in vivo study. *Med Image Anal*. 2006;10:125-136.

107. McGregor J, French J, Lawellin D, Franco-Buff A, Smith C, Todd J. Bacterial protease-induced reduction of chorioamniotic membrane strength and elasticity. *Obstet Gynecol*. 1987;69:167-174.

108. McLaren J, Taylor DJ, Bell SC. Increased concentration of pro-matrix metalloproteinase 9 in term fetal membranes overlying the cervix before labor: Implications for membrane remodeling and rupture. *Am J Obstet Gynecol*. 2000;182:409-416.

109. McParland PC, Taylor DJ, Bell SC. Mapping of zones of altered morphology and chorionic connective tissue cellular phenotype in human fetal membranes (amniochorion and decidua) overlying the lower uterine pole and cervix before labor at term. *Am J Obstet Gynecol*. 2003;189:1481-1488.

110. Meinert M, Eriksen GV, Petersen AC, et al. Proteoglycans and hyaluronan in human fetal membranes. *Am J Obstet Gynecol*. 2001;184:679-685.

111. Meinert M, Malmström A, Tufvesson E, et al. Labour induces increased concentrations of biglycan and hyaluronan in human fetal membranes. *Placenta*. 2007;28(5-6):482-486.

112. Mercer BM. Preterm premature rupture of the membranes. *Obstet Gynecol*. 2003;101:178-193.

113. Mitchell MD. *Sources of eicosanoids within the uterus during pregnancy*. Ithaca: Perinatology Press; 1988.

114. Miyanaga N, Akaza H, Yamakawa M, et al. Tissue elasticity imaging for diagnosis of prostate cancer: A preliminary report. *Int J Urol*. 2006;13:1514-1518.

115. Molina FS, Gómez LF, Florido J, Padilla MC, Nicolaides KH. Quantification of cervical elastography: A reproducibility study. *Ultrasound in Obstetrics & Gynecology*. 2012;39(6):685-689.

116. Moore R, Mansour J, Redline R, Mercer B, Moore J. The physiology of fetal membrane rupture: Insight gained from the determination of physical properties. *Placenta*. 2006;27:1037-1051.

117. Moore RM, Mansour JM, Redline RW, Mercer BM, Moore JJ. The physiology of fetal membrane rupture: Insight gained from the determination of physical properties. *Placenta*. 2006;27:1037-1051.

118. Myers K, Socrate S, Tzeranis D, House M. Changes in the biochemical constituents and morphologic appearance of the human cervical stroma during pregnancy. *Eur J Obstet Gynecol Reprod Biol*. 2009;144 Suppl 1:S82-9.

119. Myers KM, Paskaleva AP, House M, Socrate S. Mechanical and biochemical properties of human cervical tissue. *Acta Biomater*. 2008;4:104-116.

120. Myers KM, Socrate S, Paskaleva A, House M. A study of the anisotropy and tension/compression behavior of human cervical tissue. *J Biomech Eng*. 2010;132(2).

121. Norman M, Ekman G, Malmstrom A. Changed proteoglycan metabolism in human cervix immediately after spontaneous vaginal delivery. *Obstetrics & Gynecology*. 1993;81(2).

122. Norman M, Ekman G, Ulmsten U, Barchan K, Malmstrom A. Proteoglycan metabolism in the connective tissue of pregnant and non-pregnant human cervix. an in vitro study. *Biochem J*. 1991;275 (Pt 2):515-520.

123. Obara M, Hirano H, Ogawa M, et al. Changes in molecular weight of hyaluronan and hyaluronidase activity in uterine cervical mucus in cervical ripening. *Acta Obstet Gynecol Scand*. 2001;80:492-496.

124. Okazaki T, Casey ML, Okita JR, MacDonald PC, Johnston JM. Initiation of human parturition. XII. biosynthesis and metabolism of prostaglandins in human fetal membranes and uterine decidua. *Am J Obstet Gynecol*. 1981;139:373-381.

125. Okitsu O, Mimura T, Nakayama T, Aono T. Early prediction of preterm delivery by transvaginal ultrasonography. *Ultrasound Obstet Gynecol*. 1992;2:402-409.

126. Olson DM, Skinner K, Challis JR. Prostaglandin output in relation to parturition by cells dispersed from human intrauterine tissues. *J Clin Endocrinol Metab*. 1983;57:694-699.

127. Ophir J, Cespedes I, Garra B, Ponnekanti H, Huang Y, Maklad N. Elastography: Ultrasonic imaging of tissue strain and elastic modulus in vivo. *European Journal of Ultrasound*. 1996;3(1):49-70.

128. Ophir J, Cespedes I, Ponnekanti H, Yazdi Y, Li X. Elastography: A quantitative method for imaging the elasticity of biological tissues. *Ultrason Imaging*. 1991;13:111-134.

129. Ophir J, Alam SK, Garra BS, et al. Elastography: Imaging the elastic properties of soft tissues with ultrasound. *Journal of Medical Ultrasonics*. 2002;29(4):155-171.

130. Optiz H, Bernoth E. Strukturuntersuchungen der menschlichen eihaut nach vor- und rechtzeitigem blasensprung. *Archiv fur Gynakologie*. 1962;196:435-446.

131. Orgel J, Connon CJ, Nakamura T, et al. The biomechanics of amnion rupture: An X-ray diffraction study. *PLoS ONE*. 2007;2(11):e1147.

132. Osmers R, Rath W, Pflanz MA, Kuhn W, Stuhlsatz HW, Szeverenyi M. Glycosaminoglycans in cervical connective tissue during pregnancy and parturition. *Obstet Gynecol*. 1993;81:88-92.

133. Oxlund H, Helmig R, Halaburt JT, Uldbjerg N. Biomechanical analysis of human chorioamniotic membranes. *Eur J Obstet Gynecol Reprod Biol*. 1990;34:247-255.

134. Oyen M, Calvin SE, Landers DV. Premature rupture of the fetal membranes: Is the amnion the major determinant? *Am J Obstet Gynecol*. 2006;195:510-515.

135. Oyen M, Cook R, Calvin S. Mechanical failure of human fetal membrane tissues. *J Mater Sci Mater Med*. 2004;15:651-658.

136. Oyen M, Cook R, Stylianopoulos T, Barocas V, Calvin S, Landers D. Uniaxial and biaxial mechanical behavior of human amnion. *J Mater Res*. 2005;20:2902-2909.

137. Oyen ML, Calvin SE, Cook RF. Uniaxial stress-relaxation and stress-strain responses of human amnion. *J Mater Sci Mater Med*. 2004;15:619-624.

138. Pandey V, Moore R, Kumar D, et al. Repetitively stretched human fetal membranes initially strengthen and then fail. *J Soc Gynecol Investig*. 2005;12.

139. Parry-Jones E, Priya S. A study of the elasticity and tension of fetal membranes and of the relation of the area of the gestational sac to the area of the uterine cavity. *Br J Obstet Gynaecol*. 1976;83:205-212.

140. Petersen LK, Oxlund H, Uldbjerg N, Forman A. In vitro analysis of muscular contractile ability and passive biomechanical properties of uterine cervical samples from nonpregnant women. *Obstet Gynecol*. 1991;77:772-776.

141. Petersen LK, Uldbjerg N. Cervical collagen in non-pregnant women with previous cervical incompetence. *Eur J Gynecol Reprod Biol*. 1996;67:41-45.

142. Petry G. Die bedeutung der embryonalhullen bei der frage nach der herkunft alkalischer phosphatase im menschlichen fruchtwasser. 1962;158:171-180.

143. Polishuk WZ, Kohane S, Peranio A. The physical properties of fetal membranes. *Obstet Gynecol*. 1962;20:204-210.

144. Pressman EK, Cavanaugh JL, Woods JR. Physical properties of the chorioamnion throughout gestation. *Am J Obstet Gynecol*. 2002;187:672-675.

145. Rath W, Osmers R, Szeverenyi M, stuhlsatz H, Kuhn W. *Changes of glycosaminoglycans in cervical connective tissue*. Perinatology Press; 1991.

146. Rechberger T, Uldbjerg N, Oxlund H. Connective tissue changes in the cervix during normal pregnancy and pregnancy complicated by cervical incompetence. *Obstet Gynecol*. 1988;71:563-567.

147. Romero R, Yeo L, Miranda J, Hassan SS, Conde-Agudelo A, Chaiworapongsa T. A blueprint for the prevention of preterm birth: Vaginal progesterone in women with a short cervix. *J Perinat Med*. 2013;41(1):27-44.

148. Rotten D, Gavignet C, Colin MC, Robert AM, Godeau G. Evolution of the elastic fiber network of the human uterine cervix before, during and after pregnancy. A quantitative evaluation by automated image analysis. *Clin Physiol Biochem*. 1988;6:285-292.

149. Schmidt W. Der feinbau der reifen menschlichen eihaute. *Zeitschrift fur Anatomie und Entwicklungsgeschichte*. 1956;119:203-222.

150. Schober EA, Kusy RP, Savitz DA. Resistance of fetal membranes to concentrated force applications and reconciliation of puncture and burst testing. *Ann Biomed Eng*. 1994;22:540-548.

151. Scott JE. Proteoglycan-fibrillar collagen interactions. *Biochem J*. 1988;252:313-323.

152. Seo JH, Sakai K, Yui N. Adsorption state of fibronectin on poly(dimethylsiloxane) surfaces with varied stiffness can dominate adhesion density of fibroblasts. *Acta Biomater*. 2013;9(3):5493-5501.

153. Shimizu T, Endo M, Yosizawa Z. Glycoconjugates (glycosaminoglycans and glycoproteins) and glycogen in the human cervix uteri. *Tohoku J Exp Med*. 1980;131:289-299.

154. Skinner KA, Challis JR. Changes in the synthesis and metabolism of prostaglandins by human fetal membranes and decidua at labor. *Am J Obstet Gynecol*. 1985;151:519-523.

155. Skinner SJ, Campos GA, Liggins GC. Collagen content of human amniotic membranes: Effect of gestation length and premature rupture. *Obstet Gynecol*. 1981;57:487-489.

156. Smieja Z, Zakar T, Walton JC, Olson DM. Prostaglandin endoperoxide synthase kinetics in human amnion before and after labor at term and following preterm labor. *Placenta*. 1993;14:163-175.

157. So T, Ito A, Sato T, Mori Y, Hirakawa S. Tumor necrosis factor-alpha stimulates the biosynthesis of matrix metalloproteinases and plasminogen activator in cultured human chorionic cells. *Biol Reprod*. 1992;46:772-778.

158. Swiatkowska-Freund M, Preis K. Elastography of the uterine cervix: Implications for success of induction of labor. *Ultrasound Obstet Gynecol*. 2011;38:52-56.

159. Thomas A. Imaging of the cervix using sonoelastography. *Ultrasound Obstet Gynecol*. 2006;28:356-357.

160. Thomas A, Degenhardt F, Farrokh A, Wojcinski S, Slowinski T, Fischer T. Significant differentiation of focal breast lesions: Calculation of strain ratio in breast sonoelastography. *Acad Radiol*. 2010;17(5):558-563.

161. Thomas A, Kummel S, Gemeinhardt O, Fischer T. Real-time sonoelastography of the cervix: Tissue elasticity of the normal and abnormal cervix. *Acad Radiol*. 2007;14:193-200.

162. Timmons B, Akins M, Mahendroo M. Cervical remodeling during pregnancy and parturition. *Trends Endocrinol Metab*. 2010;21:353-361.

163. Uldbjerg N, Ekman G, Malmstrom A, Olsson K, Ulmsten U. Ripening of the human uterine cervix related to changes in collagen, glycosaminoglycans, and collagenolytic activity. *Am J Obstet Gynecol*. 1983;147:662-666.

164. Uldbjerg N, Malmstrom A, Ekman G, Sheehan J, Ulmsten U, Wingerup L. Isolation and characterization of dermatan sulphate proteoglycan from human uterine cervix. *Biochem J*. 1983;209:497-503.

165. Ulug U, Goldman S, Ben-Shlomo I, Shalev E. Matrix metalloproteinase (MMP)-2 and MMP-9 and their inhibitor, TIMP-1, in human term decidua and fetal membranes: The effect of prostaglandin F(2alpha) and indomethacin. *Mol Hum Reprod*. 2001;7:1187-1193.

166. von Maillot K, Stuhlsatz HW, Mohanaradhakrishnan V, Greiling H. Changes in the glycosaminoglycans distribution pattern in the human uterine cervix during pregnancy and labor. *Am J Obstet Gynecol*. 1979;135:503-506.

167. Von Maillot K, Stuhlsatz H, Gentsch H. *Connective tissue changes in the human cervix in pregnancy and labour*. New York: Churchill Livingston Inc; 1981.

168. Weiss S, Jaermann T, Schmid P, et al. Three-dimensional fiber architecture of the nonpregnant human uterus determined ex vivo using magnetic resonance diffusion tensor imaging. *Anat Rec A Discov Mol Cell Evol Biol*. 2006;288(1):84-90.

169. Westergren-Thorsson G, Norman M, Björnsson S, et al. Differential expressions of mRNA for proteoglycans, collagens and transforming growth factor-ß in the human cervix during pregnancy and involution. *Biochimica et Biophysica Acta (BBA) - Molecular Basis of Disease*. 1998;1406(2):203-213.

170. Wilder EA, Guo S, Lin-Gibson S, Fasolka MJ, Stafford CM. Measuring the modulus of soft polymer networks via a buckling-based metrology. *Macromolecules*. 2006;39(12):4138-4143.

171. Winkler M, Rath W. Changes in the cervical extracellular matrix during pregnancy and parturition. *J Perinat Med*. 1999;27:45-60.

172. Woessner JF. The determination of hydroxyproline in tissue and protein samples containing small proportions of this imino acid. *Arch Biochem Biophys*. 1961;93:440-447.

173. Wu Z, Horgan CE, Carr O, Owens RT, Iozzo RV, Lechner BE. Biglycan and decorin differentially regulate signaling in the fetal membranes. *Matrix Biology*. 2013.

174. Xu P, Alfaidy N, Challis JR. Expression of matrix metalloproteinase (MMP)-2 and MMP-9 in human placenta and fetal membranes in relation to preterm and term labor. *J Clin Endocrinol Metab*. 2002;87:1353-1361.

175. Yamaguchi S,et al. Ultrasound image of the month: Tissue elastography imaging of the uterine cervix during pregnancy. *J Med Ultrasonics*. 2007;34:209-210.

176. Yanagisawa O, Niitsu M, Kurihara T, Fukubayashi T. Evaluation of human muscle hardness after dynamic exercise with ultrasound real-time tissue elastography: A feasibility study. *Clin Radiol*. 2011;66(9):815-819.

177. Yurchenco PD, Ruben GC. Basement membrane structure in situ: Evidence for lateral associations in the type IV collagen network. *J Cell Biol*. 1987;105:2559-2568.

178. Zaga V, Estrada-Gutierrez G, Beltran-Montoya J, Maida-Claros R, Lopez-Vancell R, Vadillo-Ortega F. Secretions of interleukin-1beta and tumor necrosis factor alpha by whole fetal membranes depend on initial interactions of amnion or choriodecidua with lipopolysaccharides or group B streptococci. *Biol Reprod*. 2004;71:1296-1302.

179. Zhang Y, Conrad AH, Conrad GW. Effects of ultraviolet-A and riboflavin on the interaction of collagen and proteoglycans during corneal cross-linking. *J Biol Chem*. 2011;286(15):13011-13022.

180. Zlatnik FJ, Burmeister LF. Interval evaluation of the cervix for predicting pregnancy outcome and diagnosing cervical incompetence. *J Reprod Med*. 1993;38:365-369.